

**Establishment of Drug Screening  
Platform Using Nanopattern Mimicking  
Diseased Renal Mesangial Matrix**

**February 2020**

**Chia jung CHANG**

**Establishment of Drug Screening  
Platform Using Nanopattern Mimicking  
Diseased Renal Mesangial Matrix**

**February 2020**

**Waseda University  
Graduate School of Advanced Science and Engineering  
Department of Nanoscience and Nanoengineering,  
Research on Nanobiomaterials**

**Chia jung CHANG**

## Acknowledgement

Firstly, I would like to express my greatest appreciation to advisor, Prof. Akiyoshi Taniguchi for giving me the opportunity to join his group at National Institute for Materials Science (NIMS) and for the continuous support of my Ph.D. study and related research, for his patience, motivation, and immense knowledge. His guidance helped me in all the time of research and writing of this dissertation. I could not have imagined having a better advisor and mentor for my Ph.D. study.

Also, I would like to extend my deepest gratitude to Prof. Pi-Chao Wang, who started by proposing this PhD project and believing in my capacity to accomplish it. She has been there providing her heartfelt support and guidance at all times and has given me invaluable guidance, inspiration and encouragement in both my research and life in Japan.

I would like to express a special appreciation to my dissertation committee: Prof. Shuichi Shoji, Prof. Takashi Tanii and Prof. Jun Nakanishi for their insightful comments and valuable inputs to be included in this dissertation, and for generously spending their precious time giving me guidance, comments and encouragement.

Special thanks are extended to Prof. Tony Hsiang-Kuang Liang for his valuable medical advice, and his wife Esther for her caring and encouragement. I would also like to thank Dr. Hans and his wife Mio for their heartfelt support, suggestion and encouragement.

I am also very glad and thankful to have met and work with my lab mates Dr. Shimaa, Dr. Sun, Dr. Phuc, Dr. Alaa, Basma, and Denisa. My sincere thanks to our group secretary Iwano and Kumada for their assistance and caring.

I am very grateful to TICA, who has become my family in Tsukuba. Many thanks to Pastor Chris, David, Ailsa, Thomas, Yamamoto, Kaori, Terada, Samuel, Tito, Miura, Naho and all who have prayed and helped me throughout my research, dissertation writing, and my daily life in Japan. Even though I am not able to list everyone here, I am forever thankful.

I wish to express my deepest gratitude to my family and Pastor Peter, especially my parents for their constant support and encouragement. I deeply appreciate and thank Michael for the caring and assistance. Without whose love, this work would never be possible.

Foremost, I give all the praise, honor and thanks to Almighty God. May God bless us.

Tokyo, Japan, February 2020

Chia Jung CHANG

# Table of Contents

<b>Acknowledgement</b> .....	I
<b>Table of Contents</b> .....	I
<b>Table of Figures</b> .....	VI
<b>Table of Tables</b> .....	VIII
<b>List of Abbreviation</b> .....	IX

## Chapter I

<b>Introduction</b> .....	1
<b>1.1. Experimental Disease Models</b> .....	1
1.1.1. Advantages of <i>In Vivo</i> Animal Studies .....	2
1.1.2. Disadvantages of <i>In Vivo</i> Animal Studies .....	3
1.1.3. Advantages of <i>In Vitro</i> Studies .....	3
1.1.4. Disadvantages of <i>In Vitro</i> Studies .....	4
<b>1.2. Advanced Culture System Could Bridge the Discrepancy Between the <i>In Vivo</i> and <i>In Vitro</i></b> .....	5
1.2.1. Three-dimensional Culture Models .....	5
1.2.2. TiO <sub>2</sub> -based Nanostructured Biomaterials .....	6
<b>1.3. Hypothesis</b> .....	8
<b>References</b> .....	9

## Chapter II

<b>Establishment of An <i>In Vivo</i> Experimental Model of IBD-associated Renal Disease Studies</b> .....	14
<b>2.1. Introduction</b> .....	14
<b>2.2. Materials and Methods</b> .....	17

2.2.1. Laboratory Animals .....	17
2.2.2. Induction of DSS-colitis in Mice.....	18
2.2.3. Disease Activity Index (DAI).....	19
2.2.4. Histological Investigation.....	20
2.2.5. Immunofluorescence Staining and Confocal Imaging .....	21
2.2.6. Renal Glomerular Isolation .....	21
2.2.7. Protein Isolation and Western Blot Analysis.....	22
2.2.8. Statistical Analysis .....	23
<b>2.3. Results</b> .....	<b>24</b>
2.3.1. Progression of DSS-colitis.....	24
2.3.2. Renal Morphology and Histological Changes in DSS-colitis Mice .....	26
2.3.3. Collagen Changes in Glomeruli .....	28
2.3.4. Changes in GFB-related Proteins .....	30
2.3.5. Inflammatory Cytokines and Mediators in Kidneys after DSS Administration .....	32
<b>2.4. Discussions</b> .....	<b>33</b>
<b>2.5. Conclusion</b> .....	<b>37</b>
<b>References</b> .....	<b>37</b>

## Chapter III

### Development of an *In Vitro* Renal Disease Model to Study the Influence on

<b>Mesangial Cell Behavior</b> .....	<b>45</b>
<b>3.1. Introduction</b> .....	<b>45</b>
<b>3.2. Materials and Methods</b> .....	<b>49</b>
3.2.1. Fabrication of Nanopatterned TiO <sub>2</sub> Substrates.....	49
3.2.2. Cell Culture .....	51
3.2.3. Cell Proliferation Assay .....	52
3.2.4. Immunofluorescence Staining and Confocal Imaging .....	52

3.2.5. SEM for Cell Morphology .....	53
3.2.6. Statistical Analysis .....	54
<b>3.3. Results</b> .....	54
3.3.1. Design and Fabrication of Disease- and Normal-mimic Nanopatterned TiO <sub>2</sub> Substrates .....	54
3.3.2. MES13 Cell Proliferation on Disease-mimic Nanopatterns.....	57
3.3.3. Expressions of Specific ECM Components in MES13 Cells.....	60
3.3.4. MES13 Cell Morphological and Cytoskeletal Changes.....	62
3.3.5. $\alpha$ -SMA Expression in MES13 Cells.....	63
3.3.6. TGF- $\beta$ 1 Expression in MES13 Cells.....	65
3.3.7. Integrin $\alpha$ 5 $\beta$ 1 Expression in MES13 Cells.....	67
<b>3.5. Conclusions</b> .....	72
<b>References</b> .....	73

## Chapter IV

<b>Evaluation of Physical and Chemical Cues on Disease-mimic Culture System as a Drug Screening Platform</b> .....	80
<b>4.1. Introduction</b> .....	80
<b>4.2. Materials and Methods</b> .....	83
4.2.1. Fabrication of Nanopatterned TiO <sub>2</sub> Substrates.....	83
4.2.2. Cell Culture .....	85
4.2.3. Cell Viability Assay .....	85
4.2.4. Cell Proliferation Assays.....	86
4.2.5. Immunofluorescence Staining and Confocal Imaging .....	87
4.2.6. Evaluation of ROS Content in MES13 Cells .....	88
4.2.7. Statistical Analysis .....	89
<b>4.3. Results</b> .....	89
4.3.1. Cell Viability in TGF- $\beta$ 1 Treated MES13 Cells.....	89

4.3.2. The Effect of Disease-mimic Culture System on MES13 Cells Proliferation	92
4.3.3. The Effect of Disease-mimic Culture System on MES13 Cells ECM Component Change	95
<b>4.4. Discussion</b>	102
<b>4.5. Conclusion</b>	105
<b>References</b>	105
 <b>Chapter V</b>	
<b>Conclusions and Future Perspectives</b>	110
5.1. Conclusions	110
5.2. Future Perspectives	113
<b>References</b>	114
 <b>List of Research Achievements</b>	 116

# Table of Figures

## **Chapter I**

Figure 1. 1. Discrepancy between the in vivo and in vitro..	7
Figure 1. 2. The hypothesis of this dissertation.	8

## **Chapter II**

Figure 2. 1. Illustration of nephron and glomerulus in kidney	17
Figure 2. 2. Investigating mouse glomerular structural changes associated with dextran sulfate sodium (DSS)-induced colitis.	19
Figure 2. 3. Macro- and microscopic changes to bowel in mice with DSS-induced colitis	25
Figure 2. 4. Macro- and microscopic changes to the kidney and glomeruli in mice after DSS	27
Figure 2. 5. Changes in glomerular collagens in mice after DSS administration	29
Figure 2. 6. Changes in GFB-related proteins in mice after DSS administration.	31
Figure 2. 7. The protein expressions of inflammatory cytokines and mediators in renal cortex after DSS administration.	32

## **Chapter III**

Figure 3. 1. Illustration of normal glomerulus morphology and structural changes in diseased glomerulus	47
Figure 3. 2. Illustration of the steps required for nanopatterned TiO <sub>2</sub> substrates fabrication process.	51
Figure 3. 3. Characterization of each fabricated titanium dioxide (TiO <sub>2</sub> ) nanopatterns used in this study including groove/ridge width and depth	56
Figure 3. 4. Proliferation of MES13 cells cultured on disease- and normal-mimic nanopatterns	58
Figure 3. 5. Proliferation of MES13 cells cultured on disease- and normal-mimic nanopatterns	59
Figure 3. 6. Expressions of diseased ECM components in MES13 cells cultured on disease- and normal-mimic nanopatterns.	61
Figure 3. 7. Expressions of normal ECM components in MES13 cells cultured on disease- and normal-mimic nanopatterns.	61

Figure 3. 8. MES13 cell morphological and cytoskeletal changes in disease- and normal-mimic nanopatterns. ....	64
Figure 3. 9. Alpha-smooth muscle actin ( $\alpha$ -SMA) expression in MES13 cells influenced by disease- and normal-mimic nanopatterns .....	65
Figure 3. 10. Transforming growth factor beta 1 (TGF- $\beta$ 1) expression in MES13 cells influenced by disease- and normal-mimic nanopatterns.....	66
Figure 3. 11. Integrin $\alpha$ 5 $\beta$ 1 expression in MES13 cells influenced by disease- and normal-mimic nanopatterns. ....	67
Figure 3. 12. The possible mechanism of cells sense nanopatterned substrates through the integrins assembly and integrin clusters formation.....	71

## **Chapter IV**

Figure 4. 1. Scheme of drug screening platform using a disease-mimic model for new drug discovery .....	81
Figure 4. 2. Effect of various concentrations of TGF- $\beta$ 1 on MES13 cell viability in 96-well plates.....	90
Figure 4. 3. Effect of various concentrations of A83-01 on MES13 cell viability in 96-well plates. ....	91
Figure 4. 4. Effect of various concentrations of DEX on MES13 cell viability in 96-well plates. ....	92
Figure 4. 5. Effect of disease-mimic culture system on MES13 cell proliferation.....	94
Figure 4. 6. Effects of TGF- $\beta$ 1 and disease-mimic nanopattern on expression of type I collagen (COL1) in MES13 cells. ....	97
Figure 4. 7. The expression of type IV collagen (COL4) in MES13 cells. ....	98
Figure 4. 8. ROS proliferation in MES13 cells treated with TGF- $\beta$ 1 (1ng/ml), A83-01 (1 $\mu$ M), DEX (10nM) or untreated (0) at indicated time points in 96-well plates.....	100
Figure 4. 9. Effects of TGF- $\beta$ 1 and disease-mimic nanopattern on ROS generation in MES13 cells. ....	101

## **Chapter V**

Figure 5. 1. Illustration of summary that the consistent results from in vivo and in vitro models developed a disease-mimic culture system that could be used for drug screening platform. ....	112
Figure 5. 2. Illustration of the future prospects to establish the organ-specific <i>in vitro</i> fibrosis model using nanopatterning. ....	114

## Table of Tables

Table 2. 1. Criteria for scoring disease activity index (DAI).....	20
Table 2. 2. List of antibodies used in immunofluorescence staining and western blotting.....	23
Table 3. 1. List of antibodies used in immunofluorescence staining.....	53
Table 4. 1. List of antibodies used in immunofluorescence staining.....	87

## List of Abbreviation

<b>ECM</b>	Extracellular matrix
<b>TiO<sub>2</sub></b>	Titanium dioxide
<b>3D</b>	Three-dimensional
<b>EBL</b>	Electron beam lithography
<b>DSS</b>	DSS Dextran sulfate sodium
<b>MC</b>	Mesangial cell
<b>IBD</b>	Inflammatory bowel disease
<b>TNF-<math>\alpha</math></b>	Tumor necrosis factor- $\alpha$
<b>IL-6</b>	Interleukin-6
<b>TGF-<math>\beta</math>1</b>	Transforming growth factor- $\beta$ 1
<b>iNOS</b>	Inducible nitric oxide synthase
<b>COX-2</b>	Cyclooxygenase-2
<b>GFB</b>	Glomerular filtration barrier
<b>GBM</b>	Glomerular basement membrane
<b>DAI</b>	Disease activity index
<b>PBS</b>	Phosphate buffered saline
<b>HE</b>	Hematoxylin and eosin
<b>DAPI</b>	4',6-diamidino-2-phenylindole
<b>PAS</b>	Periodic acid-Schiff
<b>MT</b>	Masson's trichrome
<b>COL4</b>	Type IV collagen
<b>COL1</b>	Type I collagen
<b>COL5</b>	Type V collagen
<b>MM</b>	Mesangial matrix
<b><math>\alpha</math>-SMA</b>	Alpha-smooth muscle actin
<b>SCCM</b>	Standard cubic centimeter/minute
<b>ALD</b>	Atomic layer deposition
<b>MES13</b>	SV40MES13 immortalized mouse mesangial cell line

<b>DMEM</b>	Dulbecco's modified Eagle's medium
<b>FBS</b>	Fetal bovine serum
<b>BSA</b>	Bovine serum albumin
<b>TBS</b>	Tris-buffered saline
<b>WST-1</b>	4-[3-(4-Iodophenyl)-2-(4-nitrophenyl)-2H-5-tetrazolio]-1,3-benzene Disulfonate
<b>ROS</b>	Reactive oxygen species
<b>DEX</b>	Dexamethasone

---

# Chapter I

## Introduction

---

### 1.1. Experimental Disease Models

Experimental disease models are commonly used for studies of fundamental and pre-clinical research. This experimental disease research can be conducted with both *in vitro* and *in vivo* models with animals, tissue, and cell cultures [1]. Disease models are the means of pre-clinical studies that use animals or cells to exhibit all or some of the pathological manifestations that are observed in relevant human disease which are either induced or naturally occur [2]. Disease models are essential for the understanding of disease states, pathogenesis, evaluating of pharmaceutical efficacy, developing of novel therapeutics and drug discovery [3,4]. Thus, the appropriate experimental *in vivo* and *in vitro* models are important for the human disease related studies. However, these experimental models are not always perfect in reflecting the actual human disease due to various reasons. For example, tightly controlled *in vivo* and *in vitro* models are difficult to be expected to human physiological environment. In addition, variation such as individual biology, genetics, biochemistry, and metabolism are different between experimental animals and human [5,6]. These limitations need to be considered and solutions that could bridge the discrepancy are needed.

### **1.1.1. Advantages of *In Vivo* Animal Studies**

The term “*in vivo*” is a Latin word which means “within the living”, which means the experiments are performed within a whole, living organism. Humans and mammals have phylogenetic and physiological similarities, and it leads that experimental animals are widely used in pre-clinical models in investigation of disease before applying to humans [7,8]. Herein, *in vivo* animal models address a variety of scientific issues of human disease, from basic science to the elucidation of toxicological, oncological, pharmacological, pathological mechanism, and prevention or novel therapeutic strategies [8]. Among experimental animals, mice are the most commonly used animal model, as more than 95% of the genes are homologous to humans [8,9]. Experimental mice as an animal model offer a number of advantages. For instance, mice volume is small and therefore, easy to maintain and ship with lower expense than other large animals. Mice have short gestation periods around twenty days with large numbers of offspring. One of the most significant advantages of mice models is that they have proved useful in studies of renal function, stroke, vascular function, atherosclerosis and hypertension [10,7,11,].

The use of mice as *in vivo* models for human disease is not only based on the genetic and physiological similarities between the species but also being able to mimic human disease or condition by genetic engineering.

### **1.1.2. Disadvantages of *In Vivo* Animal Studies**

Although animal models have offered valuable contribution on the research of human disease, they still show some disadvantages and limitations are noticeable. Firstly, despite high similarities, there are still significant differences between the species which might be related to the animal selection [12]. Inbreeding and genetic drift cause limited genetic diversity and low experimental replicability [13]. Adoption of outbred mice such as ICR strain that have a genetic condition that is similar to humans might dissolve the limitation [14,15]. Regarding the ethical and animal welfare consideration, 3R rules for replacement, reduction and refinement of animal experiments is required to practice [8,13]. Animal use and number must be prudent, considered and calculated carefully. The procedure of animal experiments must be considered throughout to minimize any stress, pain and harm inflicted to the animals [8, 16]. However, these limitations could be altered by an *in vitro* model.

### **1.1.3. Advantages of *In Vitro* Studies**

“*In vitro*” means “within the glass” in Latin. Therefore, the studies are done in glass or Petri dishes. *In vitro* models are used to study the cell behavior in a simple environment free of normal homeostasis and stress of an experiment that occurs in an animal model [17].

*In vitro* models have many advantages compared to *in vivo* models, such as precise control of chemical and physical environment (such as pH, temperature, oxygen, and carbon dioxide), reduced animal numbers, less animal welfare issues, lower expense on animal maintenance and care and shorter time period with higher throughput [18].

Mammalian cell *in vitro* model provides a defined platform for investigation of cell biology, development of tissue engineering, understanding of the pathological underlying mechanisms of diseases and cellular drug response [19,20].

#### **1.1.4. Disadvantages of *In Vitro* Studies**

However, the results obtained from *in vitro* models have often failed to adequately represent the *in vivo* situation. One of the biggest issues is that the typical culture system on flat substrate or petri dishes receives completely different environments that lack the complex environment of the extracellular matrix (ECM) in native tissues, including nano- to micrometer scale structures [17,21]. In fact, all tissue and living cells *in vivo* are surrounded by other cells and ECM in an environment with micro- to nano-scale structure [22]. However, cells are cultured as monolayers on the typical culture flat surfaces. These differences result in cell flattening and remodeling of its internal cytoskeleton. Such changes affect cell morphological change, cellular responses, functions and gene expression changes, resulting in failing to reflect *in vivo* cell behavior [19]. These cultured cells do not mimic the natural structures of tissues and result in discrepancy between the *in vitro* and *in vivo* studies [20] which is thought to be a critical point to the high failure rate in drug discovery. Figure 1.1 illustrated the discrepancy between *the in vivo* and *in vitro*.

## **1.2. Advanced Culture System Could Bridge the Discrepancy Between the *In Vivo* and *In Vitro***

Cell cultures from all the cell types are commonly used in *in vitro* models providing wide contributions on the biomedical investigation, diseases mechanisms and new drug discovery. Nevertheless, cell cultures still have many disadvantages and limitations.

Advanced cell culture system are allowed cells to grow and interact with surrounding extracellular framework in three dimensions [23]. It has been shown that cell responses in three-dimensional (3D) cultures are closer to the behavior *in vivo* compared to those cultured on flat substrates [24].

### **1.2.1. Three-dimensional Culture Models**

There are two classified 3D culture models, scaffold-free and scaffold-based culture systems for a specific application [23,25]. Scaffold-free 3D culture systems allow the cells to self-assemble forming self-aggregation called spheroids. Spheroids could produce their own ECM that closely mimics the structural and physiological environment, prompting the spheroids to be useful in basic tumor biology [26,27]. In scaffold-based 3D culture systems, cells are grown on artificial structure that acted as a simple mechanical support to induce cells to produce native-mimic ECM of human tissues [26,28].

### 1.2.2. TiO<sub>2</sub>-based Nanostructured Biomaterials

It is very important to investigate the cell-environment interactions that regulate cellular behavior and function [29]. The *in vivo* complex micro/nanoenvironment consists of cell populations, ECM components that form an intricate system that includes chemical and physical properties, which are critical for modulating cell fate, such as tissue-specific differentiation and promoting developmental morphogenesis [30,31]. Cells sense their immediately surrounding area via interacting with ECM architecture that adopts many topographical features [32,33]. To address these issues, nanotechnology provides a powerful means of fabricating the biomaterials that better mimic *in vivo* environment by controlling scaffold nanotopographical features such as grooves, ridges and pores [34,35]. Among the nanofabrication techniques, electron beam lithography (EBL) provides high stability and resolution for 10-nm scale lithography which offers novel tools to perform the nanostructured biomaterials [36,37].

Nanostructured biomaterials are synthetic or natural and are designed to be used in medical applications. For example, in the medical implants field, nanostructured biomaterials are used to mimic the natural tissues structural and physiological functions, which can replace or regenerate the lost or failed structure/function in different parts of the human body such as the heart, blood vessels, elbows, knees, and dental structures [31,38]. Nanostructured biomaterials are also used in medical devices such as surgical sutures [39]. More recently, nanostructured biomaterials are applied in molecular probes as biosensors and drug delivery system [40,41]. These advantages improve the quality and longevity of human life. In general, these biomaterials are in direct contact with biological systems, and

thus they should be nontoxic and biocompatible without eliciting adverse responses in the body [42].

Titanium dioxide (TiO<sub>2</sub>) is an inorganic titanium compound and has been commonly used as coating material in biomedical applications over the past 10 years [43]. TiO<sub>2</sub> is well-known to be non-toxic, photoreactive, low cost and a biologically stable or inert material [44]. The most key functional feature is that TiO<sub>2</sub> exhibits an excellent biocompatibility to improve cell attachment, differentiation, and proliferation [45,46]. Over the past decades, TiO<sub>2</sub>-based nanostructured biomaterials have exhibited large specific surface area, proper electronic band structure, ion-changeable ability, and chemical stability, which make these TiO<sub>2</sub>-based nanostructured biomaterials to have been extensively applied in biomedical applications [43,46,47].

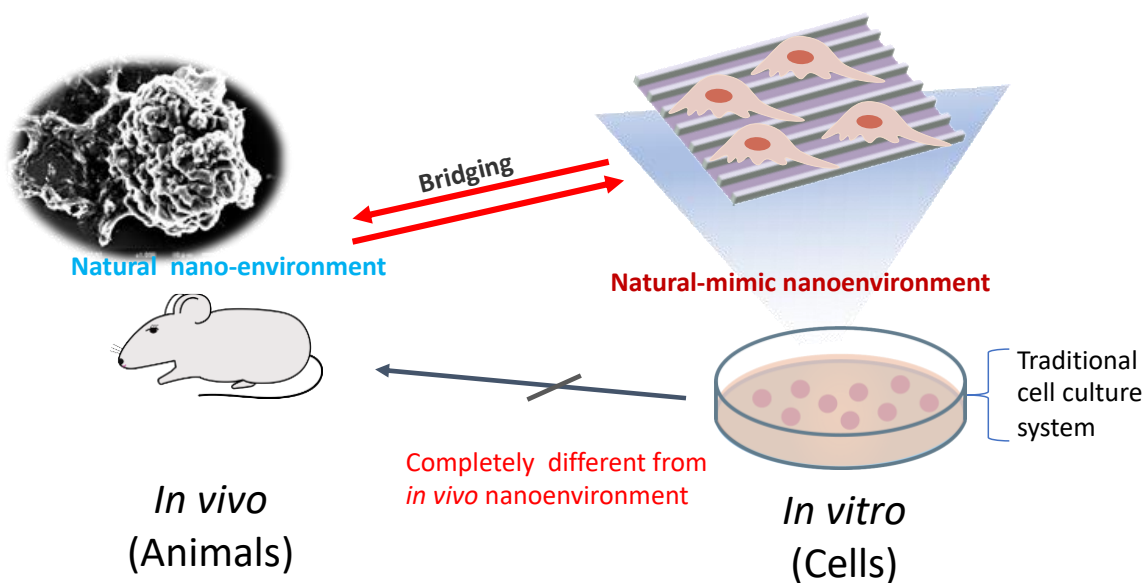


**Figure 1. 1.** Discrepancy between the *in vivo* and *in vitro*. All tissue and living cells *in vivo* are surrounded by other cells and ECM in an environment with micro- to nano-scale structure. The environment of the typical culture system is completely different from the *in vivo* nanoenvironment, which results in discrepancy between the *in vitro* and *in vivo* studies. Mimicking the natural nanoenvironment by nanopattern could bridge the discrepancy between *in vivo* and *in vitro* models.

Based on these advanced techniques, I asked a question that if the natural nanoenvironment could be mimicked by nanopattern use for *in vitro* model, it could bridge the discrepancy between *in vivo* and *in vitro* models.

### 1.3. Hypothesis

In this Doctoral dissertation, I hypothesized that mimicking the natural nanoenvironment by nanopattern could bridge the discrepancy between *in vivo* and *in vitro* models. Figure 1.2 illustrated the hypothesis of this dissertation. To examine my hypothesis, both *in vivo* model by dextran sulfate sodium (DSS)-colitis mice model and *in vitro* disease model by disease-mimic nanopattern were established to induce the cellular responses mimicking the renal disease condition. This Doctoral thesis has achieved 1) investigated the glomerular structural change in the experimental mice with DSS-induced colitis, 2) evaluated the effects of disease-mimic nanopattern on mesangial cells (MCs) proliferation and matrix change, and 3) evaluated physical and chemical cues on disease-mimic culture system as a drug screening platform.

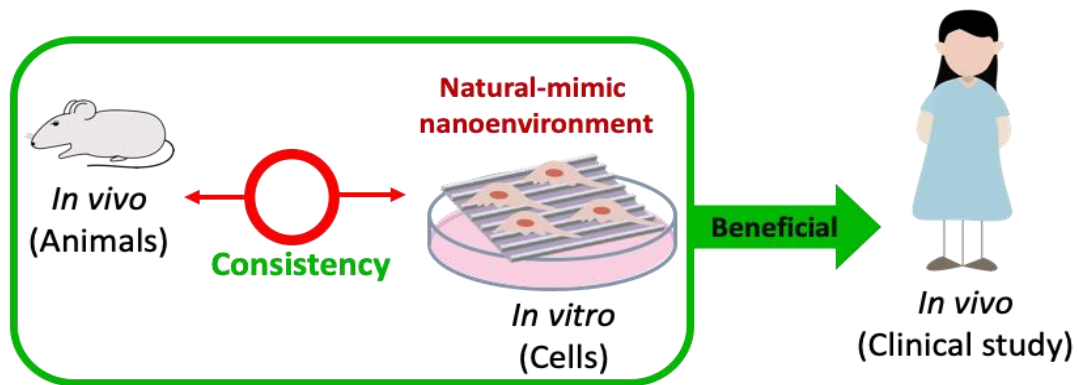


**Figure 1. 2.** The hypothesis of this dissertation that mimicking the natural nanoenvironment by nanopattern could bridge the discrepancy between *in vivo* and *in vitro* models.

## References

1. Kamimura, H.; Ito, S.; Chijiwa, H.; Okuzono, T.; Ishiguro, T.; Yamamoto, Y.; Nishinoaki, S.; Ninomiya, S.I.; Mitsui, M.; Kalgutkar, A.S. et al. Simulation of human plasma concentration-time profiles of the partial glucokinase activator PF-04937319 and its disproportionate N-demethylated metabolite using humanized chimeric mice and semi-physiological pharmacokinetic modeling. *Xenobiotica* **2017**, *47*, 382-393.
2. Morgan, S.J.; Elangbam, C.S.; Berens, S.; Janovitz, E.; Vitsky, A.; Zabka, T.; Conour, L. Use of animal models of human disease for nonclinical safety assessment of novel pharmaceuticals. *Toxicol Pathol* **2013**, *41*, 508-518.
3. Vandamme, T.F. Use of rodents as models of human diseases. *J Pharm Bioallied Sci* **2014**, *6*, 2-9.
4. Schmidt, B.J.; Papin, J.A.; Musante, C.J. Mechanistic systems modeling to guide drug discovery and development. *Drug Discov Today* **2013**, *18*, 116-127.
5. Shanks, N.; Greek, R.; Greek, J. Are animal models predictive for humans? *Philos Ethics Humanit Med* **2009**, *4*, 2.
6. Swearngen, J.R. Choosing the right animal model for infectious disease research. *Animal Model Exp Med* **2018**, *1*, 100-108.
7. Perlman, R.L. Mouse models of human disease: An evolutionary perspective. *Evol Med Public Health* **2016**, *2016*, 170-176.
8. Barre-Sinoussi, F.; Montagutelli, X. Animal models are essential to biological research: issues and perspectives. *Future Sci OA* **2015**, *1*, FSO63.
9. Garcia, Y.; Diaz-Castro, J. Advantages and disadvantages of the animal models v. in vitro studies in iron metabolism: a review. *Animal* **2013**, *7*, 1651-1658.
10. Bao, Y.W.; Yuan, Y.; Chen, J.H.; Lin, W.Q. Kidney disease models: tools to identify mechanisms and potential therapeutic targets. *Zool Res* **2018**, *39*, 72-86.

11. Lerman, L.O.; Kurtz, T.W.; Touyz, R.M.; Ellison, D.H.; Chade, A.R.; Crowley, S.D.; Mattson, D.L.; Mullins, J.J.; Osborn, J.; Eirin, A. et al. Animal Models of Hypertension: A Scientific Statement From the American Heart Association. *Hypertension* **2019**, *73*, e87-e120.
12. Justice, M.J.; Dhillon, P. Using the mouse to model human disease: increasing validity and reproducibility. *Dis Model Mech* **2016**, *9*, 101-103.
13. Hartung, T. Thoughts on limitations of animal models. *Parkinsonism Relat Disord* **2008**, *14 Suppl 2*, S81-83.
14. Wareing, T.H.; Merrill, W.H. Aorto-esophageal fistula: unusual complication. *South Med J* **1989**, *82*, 1306-1308.
15. Tuttle, A.H.; Philip, V.M.; Chesler, E.J.; Mogil, J.S. Comparing phenotypic variation between inbred and outbred mice. *Nat Methods* **2018**, *15*, 994-996.
16. Graham, M.L.; Prescott, M.J. The multifactorial role of the 3Rs in shifting the harm-benefit analysis in animal models of disease. *Eur J Pharmacol* **2015**, *759*, 19-29.
17. Kapalczynska, M.; Kolenda, T.; Przybyla, W.; Zajaczkowska, M.; Teresiak, A.; Filas, V.; Ibbs, M.; Blizniak, R.; Luczewski, L.; Lamperska, K. 2D and 3D cell cultures - a comparison of different types of cancer cell cultures. *Arch Med Sci* **2018**, *14*, 910-919.
18. Festing, S.; Wilkinson, R. The ethics of animal research. Talking Point on the use of animals in scientific research. *EMBO Rep* **2007**, *8*, 526-530.
19. Knight, E.; Przyborski, S. Advances in 3D cell culture technologies enabling tissue-like structures to be created in vitro. *J Anat* **2015**, *227*, 746-756.
20. Duval, K.; Grover, H.; Han, L.H.; Mou, Y.; Pegoraro, A.F.; Fredberg, J.; Chen, Z. Modeling Physiological Events in 2D vs. 3D Cell Culture. *Physiology (Bethesda)* **2017**, *32*, 266-277.
21. Antoni, D.; Burckel, H.; Josset, E.; Noel, G. Three-dimensional cell culture: a breakthrough in vivo. *Int J Mol Sci* **2015**, *16*, 5517-5527.

22. Birgersdotter, A.; Sandberg, R.; Ernberg, I. Gene expression perturbation in vitro--a growing case for three-dimensional (3D) culture systems. *Semin Cancer Biol* **2005**, *15*, 405-412.
23. Langhans, S.A. Three-Dimensional in Vitro Cell Culture Models in Drug Discovery and Drug Repositioning. *Front Pharmacol* **2018**, *9*, 6.
24. Edmondson, R.; Broglie, J.J.; Adcock, A.F.; Yang, L. Three-dimensional cell culture systems and their applications in drug discovery and cell-based biosensors. *Assay Drug Dev Technol* **2014**, *12*, 207-218.
25. Alghuwainem, A.; Alshareeda, A.T.; Alsowayan, B. Scaffold-Free 3-D Cell Sheet Technique Bridges the Gap between 2-D Cell Culture and Animal Models. *Int J Mol Sci* **2019**, *20*.
26. Nunes, A.S.; Barros, A.S.; Costa, E.C.; Moreira, A.F.; Correia, I.J. 3D tumor spheroids as in vitro models to mimic in vivo human solid tumors resistance to therapeutic drugs. *Biotechnol Bioeng* **2019**, *116*, 206-226.
27. Michailidis, E.; Vercauteren, K.; Mancio-Silva, L.; Andrus, L.; Jahan, C.; Ricardo-Lax, I.; Zou, C.; Kabbani, M.; Park, P.; Quirk, C. et al. Expansion, in vivo-ex vivo cycling, and genetic manipulation of primary human hepatocytes. *Proc Natl Acad Sci U S A* **2020**.
28. Carletti, E.; Motta, A.; Migliaresi, C. Scaffolds for tissue engineering and 3D cell culture. *Methods Mol Biol* **2011**, *695*, 17-39.
29. Ruprecht, V.; Monzo, P.; Ravasio, A.; Yue, Z.; Makhija, E.; Strale, P.O.; Gauthier, N.; Shivashankar, G.V.; Studer, V.; Albiges-Rizo, C. et al. How cells respond to environmental cues - insights from bio-functionalized substrates. *J Cell Sci* **2017**, *130*, 51-61.
30. Muncie, J.M.; Weaver, V.M. The Physical and Biochemical Properties of the Extracellular Matrix Regulate Cell Fate. *Curr Top Dev Biol* **2018**, *130*, 1-37.

31. Chen, F.M.; Liu, X. Advancing biomaterials of human origin for tissue engineering. *Prog Polym Sci* **2016**, *53*, 86-168.
32. Kechagia, J.Z.; Ivaska, J.; Roca-Cusachs, P. Integrins as biomechanical sensors of the microenvironment. *Nat Rev Mol Cell Biol* **2019**, *20*, 457-473.
33. Lu, P.; Takai, K.; Weaver, V.M.; Werb, Z. Extracellular matrix degradation and remodeling in development and disease. *Cold Spring Harb Perspect Biol* **2011**, *3*.
34. Krishna, L.; Dhamodaran, K.; Jayadev, C.; Chatterjee, K.; Shetty, R.; Khora, S.S.; Das, D. Nanostructured scaffold as a determinant of stem cell fate. *Stem Cell Res Ther* **2016**, *7*, 188.
35. Donnelly, H.; Salmeron-Sanchez, M.; Dalby, M.J. Designing stem cell niches for differentiation and self-renewal. *J R Soc Interface* **2018**, *15*.
36. Ermis, M.; Antmen, E.; Hasirci, V. Micro and Nanofabrication methods to control cell-substrate interactions and cell behavior: A review from the tissue engineering perspective. *Bioact Mater* **2018**, *3*, 355-369.
37. Biswas, A.; Bayer, I.S.; Biris, A.S.; Wang, T.; Dervishi, E.; Faupel, F. Advances in top-down and bottom-up surface nanofabrication: techniques, applications & future prospects. *Adv Colloid Interface Sci* **2012**, *170*, 2-27.
38. Zhang, K.; Wang, S.; Zhou, C.; Cheng, L.; Gao, X.; Xie, X.; Sun, J.; Wang, H.; Weir, M.D.; Reynolds, M.A. et al. Advanced smart biomaterials and constructs for hard tissue engineering and regeneration. *Bone Res* **2018**, *6*, 31.
39. Serrano, C.; Garcia-Fernandez, L.; Fernandez-Blazquez, J.P.; Barbeck, M.; Ghanaati, S.; Unger, R.; Kirkpatrick, J.; Arzt, E.; Funk, L.; Turon, P. et al. Nanostructured medical sutures with antibacterial properties. *Biomaterials* **2015**, *52*, 291-300.
40. Ngoepe, M.; Choonara, Y.E.; Tyagi, C.; Tomar, L.K.; du Toit, L.C.; Kumar, P.; Ndesendo, V.M.; Pillay, V. Integration of biosensors and drug delivery technologies for early detection and chronic management of illness. *Sensors (Basel)* **2013**, *13*, 7680-7713.

41. Patra, J.K.; Das, G.; Fraceto, L.F.; Campos, E.V.R.; Rodriguez-Torres, M.D.P.; Acosta-Torres, L.S.; Diaz-Torres, L.A.; Grillo, R.; Swamy, M.K.; Sharma, S. et al. Nano based drug delivery systems: recent developments and future prospects. *J Nanobiotechnology* **2018**, *16*, 71.
42. Williams, D.F. Specifications for Innovative, Enabling Biomaterials Based on the Principles of Biocompatibility Mechanisms. *Front Bioeng Biotechnol* **2019**, *7*, 255.
43. Banerjee, A.N. The design, fabrication, and photocatalytic utility of nanostructured semiconductors: focus on TiO<sub>2</sub>-based nanostructures. *Nanotechnol Sci Appl* **2011**, *4*, 35-65.
44. Pilar de Lara-Castells, M.; Hauser, A.W.; Ramallo-Lopez, J.M.; Buceta, D.; Giovanetti, L.J.; Lopez-Quintela, M.A.; Requejo, F.G. Increasing the optical response of TiO<sub>2</sub> and extending it into the visible region through surface activation with highly stable Cu<sub>5</sub> clusters. *J Mater Chem A Mater* **2019**, *7*, 7489-7500.
45. Chen, X.; Mao, S.S. Titanium dioxide nanomaterials: synthesis, properties, modifications, and applications. *Chem Rev* **2007**, *107*, 2891-2959.
46. Kulkarni, M.; Mazare, A.; Gongadze, E.; Perutkova, S.; Kralj-Iglic, V.; Milosev, I.; Schmuki, P.; Iglic, A.; Mozetic, M. Titanium nanostructures for biomedical applications. *Nanotechnology* **2015**, *26*, 062002.
47. Hamidi, F.; Aslani, F. TiO<sub>2</sub>-based Photocatalytic Cementitious Composites: Materials, Properties, Influential Parameters, and Assessment Techniques. *Nanomaterials (Basel)* **2019**, *9*.

---

## Chapter II

# Establishment of An *In Vivo* Experimental Model of IBD-associated Renal Disease Studies

---

### 2.1. Introduction

Inflammatory bowel disease (IBD) is a chronic, excessive and relapsing inflammatory disorder of the gastrointestinal tract characterized by inflammation and mucosal tissue damage and is associated with significant morbidity. Ulcerative colitis and Crohn's disease are the two most common forms of IBD. Ulcerative colitis and Crohn's disease differ from each other in physiology, but show similar symptoms such as severe diarrhea, rectal bleeding, abdominal pain, fever, and weight loss [1,2]. The pathogenesis of IBD is still largely unknown. However, defective immunological responses in IBD patients are reported, especially inflammatory cytokine network abnormalities caused by chronic and excessive inflammation of the gastrointestinal tract can lead to active inflammation [3]. Increased level of inflammatory cytokines such as tumor necrosis factor- $\alpha$  (TNF- $\alpha$ ), interleukin-6 (IL-6), transforming growth factor- $\beta$ 1 (TGF- $\beta$ 1), and inflammatory mediators including inducible nitric oxide synthase (iNOS) and cyclooxygenase-2 (COX-2) were found in patients with IBD [3–6]. This disturbance of inflammatory cytokines and mediators results in tissue damage which plays a critical role in the pathogenesis of IBD [7].

---

Clinical and epidemiological evidence suggest that the long-term inflammatory condition of IBD is accompanied by various extraintestinal manifestations and complications. These extraintestinal manifestations and complications can affect almost every organ system, including the musculoskeletal system, skin, eyes, liver, lungs, kidneys, immune system, hematologic system, and cardiovascular system [2,8].

Mammalian kidneys play critical roles in controlling blood pressure, filtering blood and concentrating metabolic waste through formation of urine [9]. Renal manifestations and complications in patients with IBD are not rare, and numerous clinical studies have reported that 4–23% of IBD patients experience renal disease such as tubulointerstitial nephritis, nephrolithiasis, and glomerulonephritis [10–17], which eventually induce renal disease. The appropriate experimental animal model of IBD-associated renal disease thus has clinical importance for related studies, including pathological mechanisms, prevention and treatment strategies for IBD.

Dextran sulfate sodium (DSS) is a water-soluble sulfated polysaccharide. Oral administration of DSS to trigger acute colitis has been widely used in experimental animal models for preclinical studies of IBD, because the pathophysiology resembles human Ulcerative colitis [18–20]. Recent studies have reported that mice with colitis induced by DSS show renal tubular injury that might be associated with increased neutrophil infiltration and expressions of cytokines and chemokines in both intestines and kidneys [21,22]. However, these studies of DSS-related renal injury have not mentioned structural changes to the glomeruli. On the other hand, the renal glomerulus is included in the nephron with the tubule, and tubular necrosis has been reported to potentially lead to

declines in glomerular function [23,24], suggesting that glomerular damage might be accompanied by tubular injury.

The glomerulus contains a highly specialized filtration barrier structure that is essential for maintaining normal plasma ultrafiltration, and loss of glomerular filtration function can lead to poor blood filtration, resulting in renal disease [25,26]. The selectively permeable glomerular filtration barrier (GFB) is a three-layered structure that separates the capillaries and Bowman's space, and comprises the interdigitating foot processes of the podocytes, the intervening glomerular basement membrane (GBM), and the fenestrated endothelium, as illustrated in Figure 2.1 [27,28]. The GBM is constituted of specialized extracellular matrix (ECM) components, namely IV collagen (COL4), laminin and other proteoglycans, which are essential for providing a complete structural scaffold to the glomeruli, and are important for establishing and maintaining the integrity of the GFB [29,30]. Disrupted GBM has been demonstrated to lead to filtration barrier damage and eventual glomerular disease [30,31]. However, whether GFB-related protein changes are involved in IBD associated renal disease has not yet been clarified. Herein, this chapter is aimed to establish an *in vivo* experimental model of IBD-associated renal disease studies. This study investigated the glomerular structural change in the experimental mice with dextran sulfate sodium (DSS)-induced colitis. The glomerular structural changes were focused on specific types of glomerular collagens and GFB-related proteins after DSS administration, to demonstrate the coexistence of glomerular structural changes and IBD in a DSS-induced colitis mouse model. This study should help establish an experimental animal model for further elucidation of the clinical pathological mechanisms of IBD-associated renal disease.

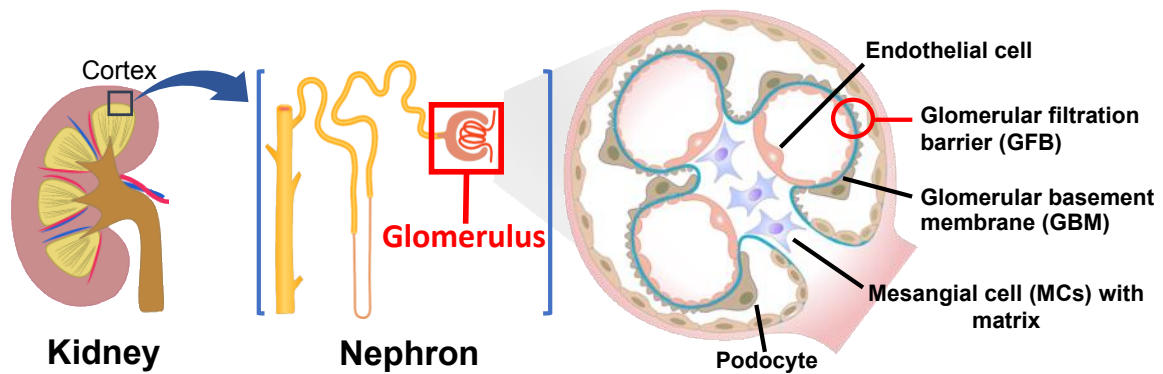


**Figure 2. 1.** Illustration of nephron and glomerulus in kidney. Nephron is the filtration unit of kidney, and it has a barrier structure called glomerulus. Cells of the glomerular tuft include MCs, endothelial cells, and podocytes are shown, along with the GBM. The GFB is a highly specialized structure mainly constituted by mesangial, endothelial, podocytes and GBM.

## 2.2. Materials and Methods

### 2.2.1. Laboratory Animals

Seven-week-old male Slc:ICR strain mice weighing 28–30 g (Japan SLC, Hamamatsu, Japan) were housed in the Central Animal House at the University of Tsukuba under climate-controlled conditions (room temperature,  $22 \pm 2$  °C; 12-h light/dark cycle; relative humidity, 65%). Cages were cleaned and sterilized every week. All mice were given free access to food and water. Animal experiments were conducted in strict accordance with the recommendations of the Guide for the Care and Use of Laboratory Animals of the Science Council of Japan and Ministry of Education, Culture, Sports, Science and Technology of Japan. The protocol was approved by the Committee on the Ethics of

Animal Experiments of the University of Tsukuba (Permit Number: 14-047; May 2016) based on the Institutional Animal Care and Use Committee (IACUC). All surgery was performed under sodium pentobarbital anesthesia, and all efforts were made to minimize suffering.

### **2.2.2. Induction of DSS-colitis in Mice**

As a widely used model of IBD, the DSS-induced colitis mouse model was used in this study to investigate changes to renal glomerular collagens and GFB-related proteins. This mouse model was established by inducing colitis with the administration of DSS in drinking water for eight days (Figure 2.2), following the previously described method [21]. Briefly, mice were administered 3.5% (*w/v*) DSS (MW 36,000–50,000 Da; MP Biomedicals, Solon, OH, USA) dissolved in drinking water for eight days. Six mice per group were used in each experiment, and were not allowed access to any other source of water. Mouse weights were monitored daily to quantify the systemic consequences of colitis. Mice were fed with normal water in place of DSS water on Day 8 and euthanized on Day 9. Colon length and kidney weight were measured for each mouse at harvest, then fixed in 10% neutral buffered formalin (Wako, Osaka, Japan) or stored at  $-80\text{ }^{\circ}\text{C}$  for further use. Mice receiving only distilled water were used as controls.

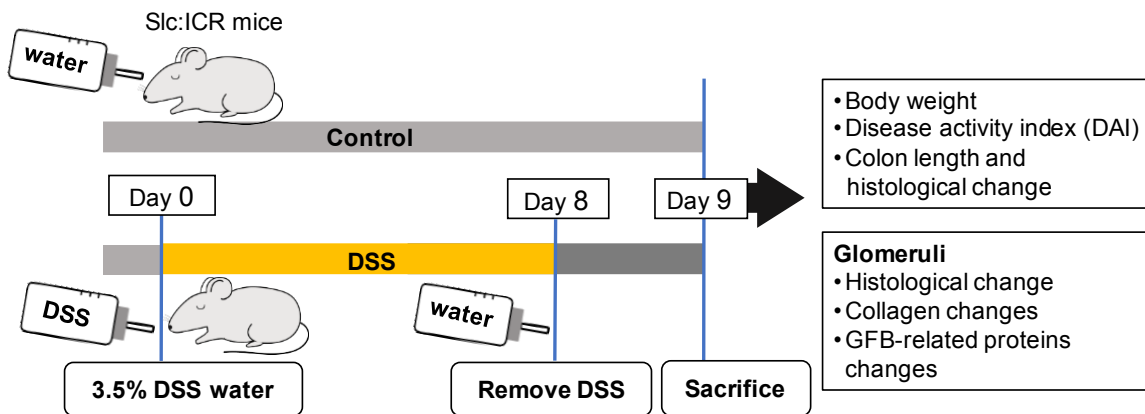


**Figure 2. 2.** Investigating mouse glomerular structural changes associated with dextran sulfate sodium (DSS)-induced colitis. Slc:ICR mice were administered 3.5% DSS in drinking water for eight days, then allowed intake of filtered water on Day 8. Control mice were given filtered water. All mice were sacrificed on Day 9 and further assessments were performed. **Abbreviation:** GFB, glomerular filtration barrier.

### 2.2.3. Disease Activity Index (DAI)

Weight loss, stool consistency, and rectal bleeding were recorded daily to assess the severity of DSS-colitis. DAI was determined based on the methods described previously [32]. Briefly, DAI was scored from 0 to 4 for each parameter, and then averaged for each group, as shown in Table 2.1. Parameters were body weight loss (0 = no weight loss; 1 = 1–5% weight loss; 2 = 6–10% weight loss; 3 = 11–15% weight loss; and 4 =  $\geq$  15% weight loss), stool consistency (0 = normal stools; 2 = loose stools; 4 = diarrhea) and gross bleeding (0 = negative, 2 = positive occult blood in stools, 4 = rectal bleeding). DAI was calculated as the sum of the weight loss, stool consistency and gross bleeding scores.

**Table 2. 1.** Criteria for scoring disease activity index (DAI).

---

<b>Score</b>	<b>Weight loss (%)</b>	<b>Stool consistency*</b>	<b>Occult blood or gross bleeding</b>
0	None	Normal	Negative
1	1-5	Loose stools	Negative
2	6-10	Loose stools	Hemoccult positive
3	11-15	Diarrhea	Hemoccult positive
4	>15	Diarrhea	Gross bleeding

---

The sum of the scores of two parameters was defined as the DAI score.

\*Normal stools = well-formed pellets; loose stools = pasty stool that does not stick to the anus; and diarrhea = liquid stools that sticks to the anus.

#### **2.2.4. Histological Investigation**

To detect injury to the colon and renal tissues, prepared tissues were cut into 2- $\mu$ m thick sections using a microtome (Thermo Fisher Scientific, Waltham, MA, USA) and stained with hematoxylin and eosin (HE) for histological investigations. To assess the GBM, periodic acid-Schiff (PAS) was used to estimate the glomerular deposition of matrix glycoprotein [33]. Briefly, 3- $\mu$ m-thick sections were stained using a PAS staining kit (Merck, Darmstadt, Germany) and counterstained with hematoxylin according to the instructions from the manufacturer. To detect collagen fiber deposition [34], 3- $\mu$ m sections were stained with a Masson's trichrome staining kit (Muto Pure Chemicals, Tokyo, Japan) according to the manufacturer's instruction. Microscopic images were acquired using a light microscope with a charge-coupled device camera (Olympus, Tokyo, Japan).

### **2.2.5. Immunofluorescence Staining and Confocal Imaging**

Immunofluorescence staining was performed by following the method described previously [35]. Briefly, kidneys were embedded in optimal cutting temperature compound (Sakura Finetek, Tokyo, Japan), and frozen in liquid nitrogen. Sections of 5- $\mu$ m thickness were cut by a cryostat (CM3050; Leica, Wetzlar, Germany); then incubated with primary antibodies against type I collagen (COL1, Acris Antibodies, Germany), COL4, type V collagen (COL5), synaptopodin, VE-cadherin (Santa Cruz Biotechnology, Santa Cruz, CA, USA), nephrin, and podocalyxin (R&D Systems, Minneapolis, MN, USA), respectively, at 4 °C overnight, and followed by secondary antibodies conjugated to Alexa Fluor® 488 or 568 (Invitrogen, Carlsbad, CA, USA); double-stained with rhodamine-conjugated phalloidin (Life Technologies, Gaithersburg, MD, USA) for F-actin; and finally submerged in fluoroshield mounting medium containing 4',6-diamidino-2-phenylindole (DAPI) (Abcam, Cambridge, UK). Confocal imaging was performed according to the method described previously [36] with a confocal microscope (LSM700; Carl Zeiss, Jena, Germany). Alexa Fluor® 488, and 568 signals were detected at laser excitation wavelengths of 488 nm and 543 nm, respectively. The antibodies used in this study were listed in Table 2.2.

### **2.2.6. Renal Glomerular Isolation**

Kidney cortex tissue from each mouse was removed, glomeruli were isolated using a serial sieving method described previously [37], and then washed with phosphate buffered saline (PBS, pH 7.4, Sigma-Aldrich, St. Louis, MO, USA) to remove small tubular

fragments. The isolated glomeruli were re-suspended by PBS for further use or dissolved in lysis buffer for protein extraction.

### **2.2.7. Protein Isolation and Western Blot Analysis**

Renal cortices (~50 mg) or isolated glomeruli from kidney cortices of each mouse were homogenized in lysis buffer (50 mM Tris pH 7.4, 250 mM NaCl, 5 mM EDTA, 2 mM Na<sub>3</sub>VO<sub>4</sub>, 1 mM NaF, 20 mM Na<sub>4</sub>P<sub>2</sub>O<sub>7</sub>, 0.02% NaN<sub>3</sub>, 1% Triton X-100, 0.1% SDS and 1 mM PMSF) with 1% protease inhibitor cocktail (Sigma-Aldrich, St. Louis, MO, USA) by sonication (Qsonica, Newtown, CT, USA), followed by incubation on ice for 10 min and centrifugation at 10,000 rpm for 10 min. Supernatant was collected and protein concentration was quantitated using the Micro BCA Protein Assay kit (Thermo Fisher Scientific, Waltham, MA, USA) according to the instructions from the manufacturer. Thirty micrograms of total protein were loaded per lane and separated by 7.5% polyacrylamide gels, followed by transferring onto methanol-activated PVDF membrane (Millipore, Billerica, MA, USA). Protein-transferred membranes were incubated with primary antibodies against COL1, COL4, COL5, synaptopodin, VE-cadherin, nephrin, podocalyxin, TNF- $\alpha$ , IL-6, iNOS, COX-2 (Cell Signaling Technology, USA), TGF- $\beta$ 1 (Santa Cruz Biotechnology) and  $\beta$ -actin, respectively, at 4 °C overnight, followed by incubation with horseradish peroxidase-conjugated secondary antibody for 2 h at room temperature. Blots were visualized with chemiluminescence substrate for 1 min and detected using a luminescent image analyzer (LAS-4000 mini; Fujifilm, Tokyo, Japan). Band density was quantitated densitometrically with Image J software (National Institutes of Health, MD, USA) by calculating the average optical density in each band. Relative and

normalized protein expressions were calculated using the ratio of each protein density to  $\beta$ -actin density. The antibodies used in this study are listed in Table 2.2.

### 2.2.8. Statistical Analysis

Statistical analyses were performed using Prism software (GraphPad, San Diego, CA, USA). All data are expressed as mean  $\pm$  standard error of the mean (SEM) from 6 replicates ( $n = 6$  mice per group) in at least 3 independent experiments. The significance of differences between groups were analyzed using Student's *t*-test. A probability level of  $p < 0.05$  was considered significant.

**Table 2. 2.** List of antibodies used in immunofluorescence staining and western blotting

Primary antibodies used	Source	Host	Molecular weight (kDa)
Type I collagen	Acris Antibodies(R1038)	Rabbit	150
Type IV collagen	Santa Cruz Biotechnology (sc-11360)	Rabbit	160-190
Type V collagen	SantaCruz Biotechnology (sc-20648)	Rabbit	220
Synaptopodin	SantaCruz Biotechnology (sc-515842)	Goat	100
VE-Cadherin	SantaCruz Biotechnology (sc-28644)	Rabbit	130
Nephrin	R&D Systems (AF3159)	Goat	185
Podocalyxin	R&D Systems (AF1556)	Goat	130
$\beta$ -actin	Thermo Fisher Scientific (MA5-15739)	Mouse	42
Secondary antibodies used	Source	Host	
Anti-Rabbit IgG Alexa Fluor 488	Invitrogen (A11034)	Goat	
Anti-Goat IgG Alexa Fluor 488	Invitrogen (A27012)	Rabbit	
Anti-Goat IgG Alexa Fluor 568	Invitrogen (A11079)	Rabbit	

## 2.3. Results

### 2.3.1. Progression of DSS-colitis

After DSS administration (Figure 2.2), significant body weight loss was observed on Days 4–8 as compared to those of controls (water only) ( $p < 0.05$ ) (Figure 2.3A). DAI scores showed elevating values after three days of DSS administration, reaching a peak on Day 8 (figure 2.3B).

Colon shortening, a marker of the severity of colorectal inflammation [20], was significantly greater in DSS-colitis mice as compared to the control group by Day 8 (Figure 2.3C). Histological observation of the colon was subsequently performed using HE-staining, which showed a normal morphology of crypts, abundant goblet cells, muscular layer, submucosa and mucosa in the control mice. However, DSS-colitis mice revealed severe epithelial damage with mucosa thickening, massive cellular infiltration into the lamina propria and colon mucosa, crypt distortion, goblet cells loss, and complete destruction of the architecture (Figure 2.3D). These histological changes indicated severe inflammatory colitis.

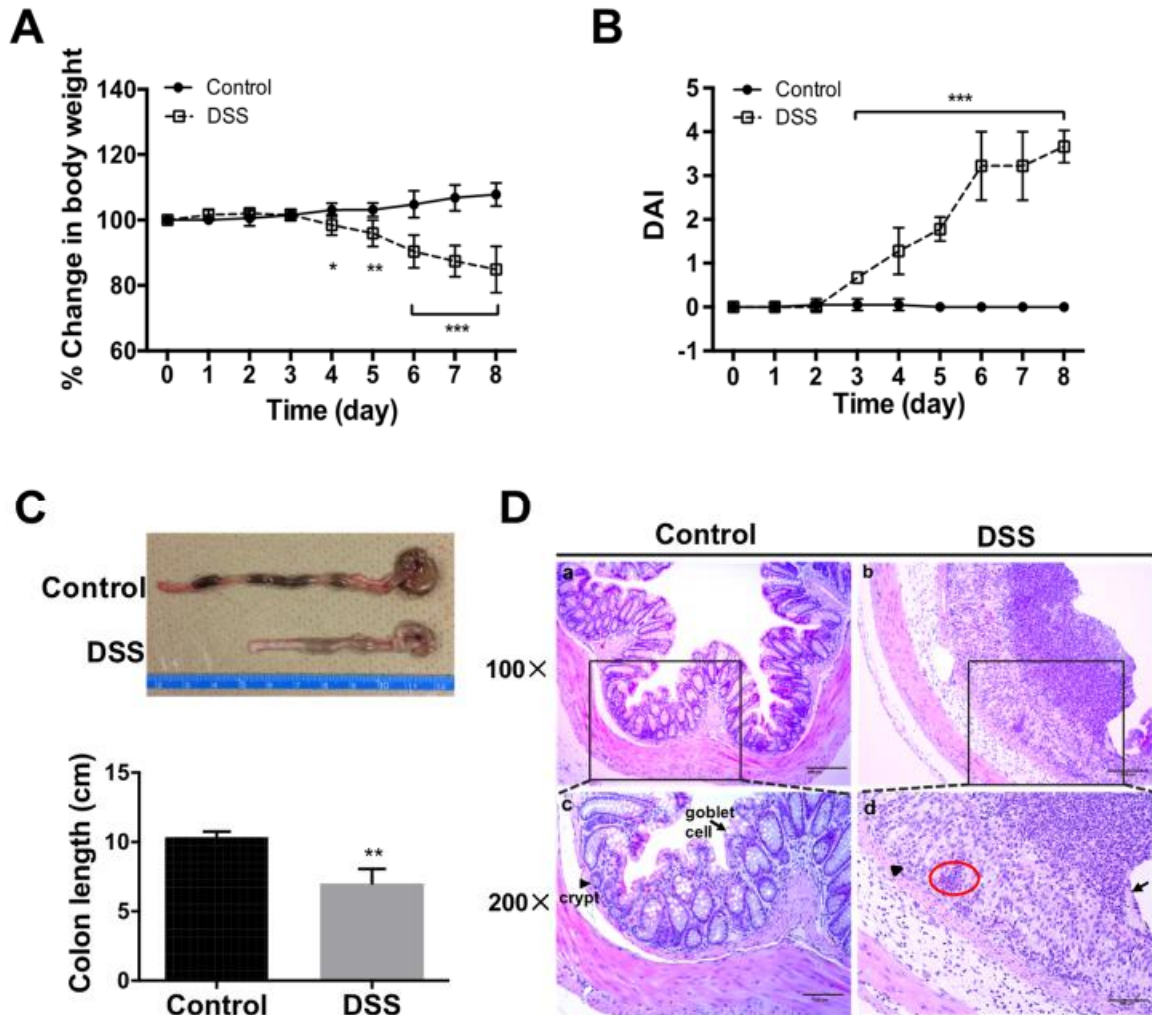


**Figure 2.3.** Macro- and microscopic changes to bowel in mice with DSS-induced colitis. Changes in body weight (A) and disease activity index (DAI) (B) were evaluated daily. Colon length was measured after sacrifice (C). Hematoxylin and eosin (HE) staining (D) showed distortion of crypts (arrowhead), loss of goblet cells (arrow), and infiltration of inflammatory cells (red circle) in colon sections from DSS-treated mice. All values are given as mean  $\pm$  SEM ( $n = 6$  mice per group); \*  $p < 0.05$ , \*\*  $p < 0.01$ , and \*\*\*  $p < 0.001$  vs. control. Scale bars: 200  $\mu\text{m}$  (a,b); and 100  $\mu\text{m}$  (c,d). **Abbreviation:** DSS, dextran sulfate sodium.

### 2.3.2. Renal Morphology and Histological Changes in DSS-colitis Mice

Human and mouse studies have indicated the involvement of non-intestinal organs in IBD [10–15]. I therefore investigated renal changes in DSS-colitis mice. Kidney size and weight of DSS-colitis mice were decreased in mice after eight days of treatment as compared to those in controls ( $p < 0.01$ ) (Figure 2.4A, B). To detect structural histological damage, glomerular morphology was examined in tissue sections by PAS and Masson's trichrome staining. Deep pink color (PAS-positive matrix) representing deposition of matrix glycoprotein was apparent at the GBM and mesangium, confirming increased matrix in the glomeruli of DSS-colitis mice (Figure 2.4C). Masson's trichrome staining was performed to detect the collagen deposition and fibrosis associated with renal disease, and blue to blue-violet staining presence of collagen in tissues. The result showed lightly stained collagen in the GBM and tubular basement membrane. On the other hand, significant collagen deposition among the glomerular capillaries and surrounding the Bowman's capsules were observed in DSS-colitis mice after eight days of DSS administration (Figure 2.4D) compared to control mice.

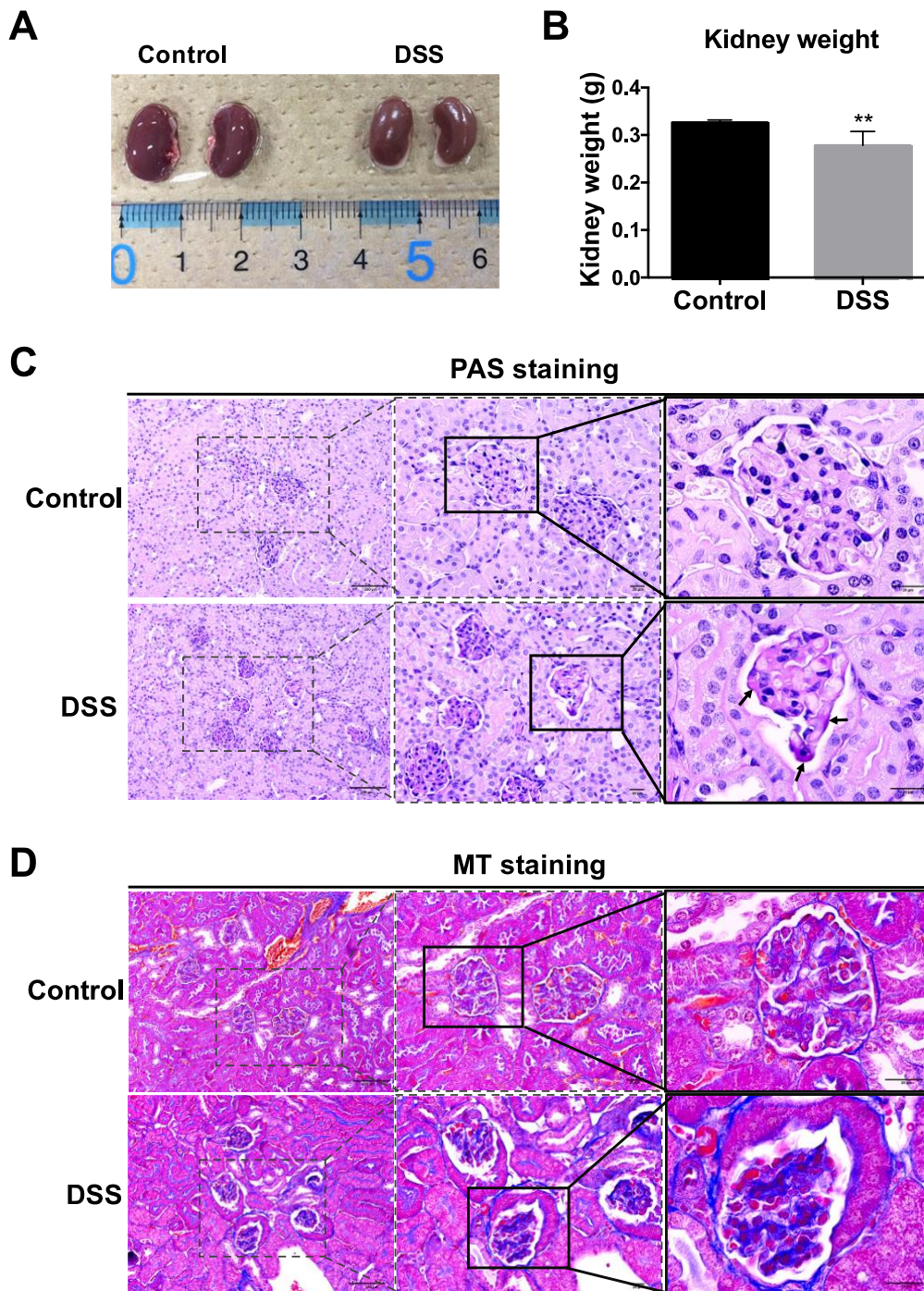


**Figure 2. 4.** Macro- and microscopic changes to the kidney and glomeruli in mice after DSS. Mouse kidney appearance (A) and weight (B) were determined at harvest. Histological manifestations were determined by PAS staining to assess the basement membrane of glomeruli (C), and MT staining to assess collagen deposition (D), respectively. Compared to control mice, glomerular accumulation of PAS-positive matrix (arrow) was prominent in matrix (arrow) was prominent in DSS-treated mice (C). Blue staining indicates the presence of collagen fibers in tissues (D). All values are given as mean  $\pm$  SEM ( $n = 6$  mice per group); \*\* $p < 0.01$  vs. control. **Abbreviation:** PAS, periodic acid-Schiff; MT, Masson's trichrome.

### 2.3.3. Collagen Changes in Glomeruli

Glomerular collagens including COL4 (a typical collagen of the basement membrane matrix), COL1 (an interstitial matrix collagen) and COL5 (a typical collagen that only appears at kidney development and in kidney diseases such as collagenofibrotic glomerulopathy) [36,37] were investigated by immunofluorescent microscopy and Western blot analysis. The results showed decreased COL4 in GBM and Bowman's capsules (Figure 2.5A-a') in DSS-colitis mice as compared to controls (Figure 2.5A-a). In contrast to COL4, COL1 and COL5 increased in the glomerular and renal interstitium (Figure 2.5A-b',-c') of DSS-colitis mice as compared to those in controls (Figure 2.5A-b,-c).

Consistent with immunofluorescent microscopy results, Western blotting analysis also showed declining expressions of COL4 ( $p < 0.05$ ) (Figure 2.5B-a), and increasing expressions of COL1 and COL5 ( $p < 0.05$ ) (Figure 2.5B-b,-c) in the renal cortex of DSS-administered mice, indicating the influence of DSS on changes in glomerular collagens. The above results are illustrated in Figure 2.5C.

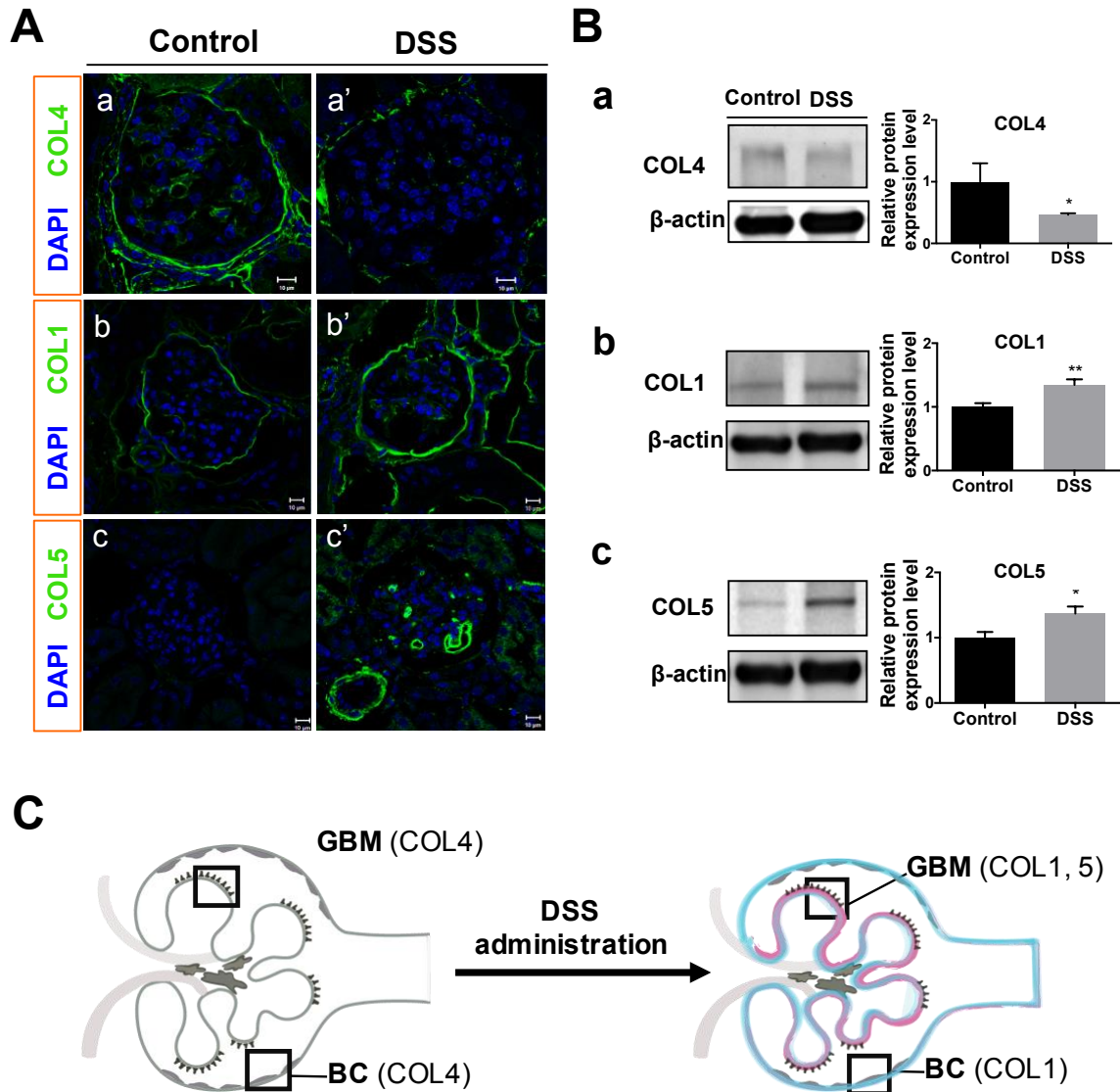


**Figure 2. 5.** Changes in glomerular collagens in mice after DSS administration. Immunofluorescent microscopy (A) and Western blot analysis of protein expression (B) for COL4 (A-a, A-a'; B-a; 160–190 kDa), COL1 (A-b, A-b'; B-b; 150 kDa), and COL5 (A-c, A-c'; B-c; 220 kDa) were conducted for control and DSS-colitis mice. Representative bands (B, left) and relative band intensity ratios were analyzed (B, right). (C) Illustration of glomerular collagens changes in this study. All values are means  $\pm$  SEM ( $n = 6$ ); \*  $p < 0.05$  and \*\*  $p < 0.01$  vs. control. Scale bars = 10  $\mu$ m. Abbreviations: GBM, glomerular basement membrane; BC, Bowman's capsule. **Abbreviation:** GBM, glomerular basement membrane; BC, Bowman's capsule. COL4, type IV collagen; COL1, type I collagen; COL5, type V collagen.

#### 2.3.4. Changes in GFB-related Proteins

The GFB comprises glomerular endothelial cells, the GBM and podocytes [28,29]. Podocytes and glomerular endothelial cells are located on opposite side of the GBM. Immunofluorescent investigation of podocyte-associated proteins in glomeruli (including synaptopodin, podocalyxin, and nephrin) were performed to detect changes in podocytes. The results showed that synaptopodin, podocalyxin, and nephrin were significantly expressed at capillary tufts of normal glomeruli in the control mice (Figure 2.6A-a, -b, -c), but declined in DSS-colitis mice after DSS administration (Figure 2.6A-a', -b', -c'). Similarly, the vascular-specific junctional molecule VE-cadherin in endothelial cells on the GBM, which is associated with the regulation of vascular permeability and glomerular filtration, showed lower immunofluorescence and discontinuous expression in DSS-colitis mice (Figure 2.6A-d') as compared to that in controls (Figure 2.6A-d).

Western blot analysis of these four proteins in glomeruli showed declines in all proteins ( $p < 0.05$ ) (Figure 2.6B), consistent with the results from immunofluorescence (Figure 2.6A).

These findings confirmed that DSS administration caused podocyte damage (reductions in synaptopodin, podocalyxin and nephrin) and changes to endothelial adherens junctions in glomerular endothelium (reductions in VE-cadherin). These results are shown in Figure 2.6C.

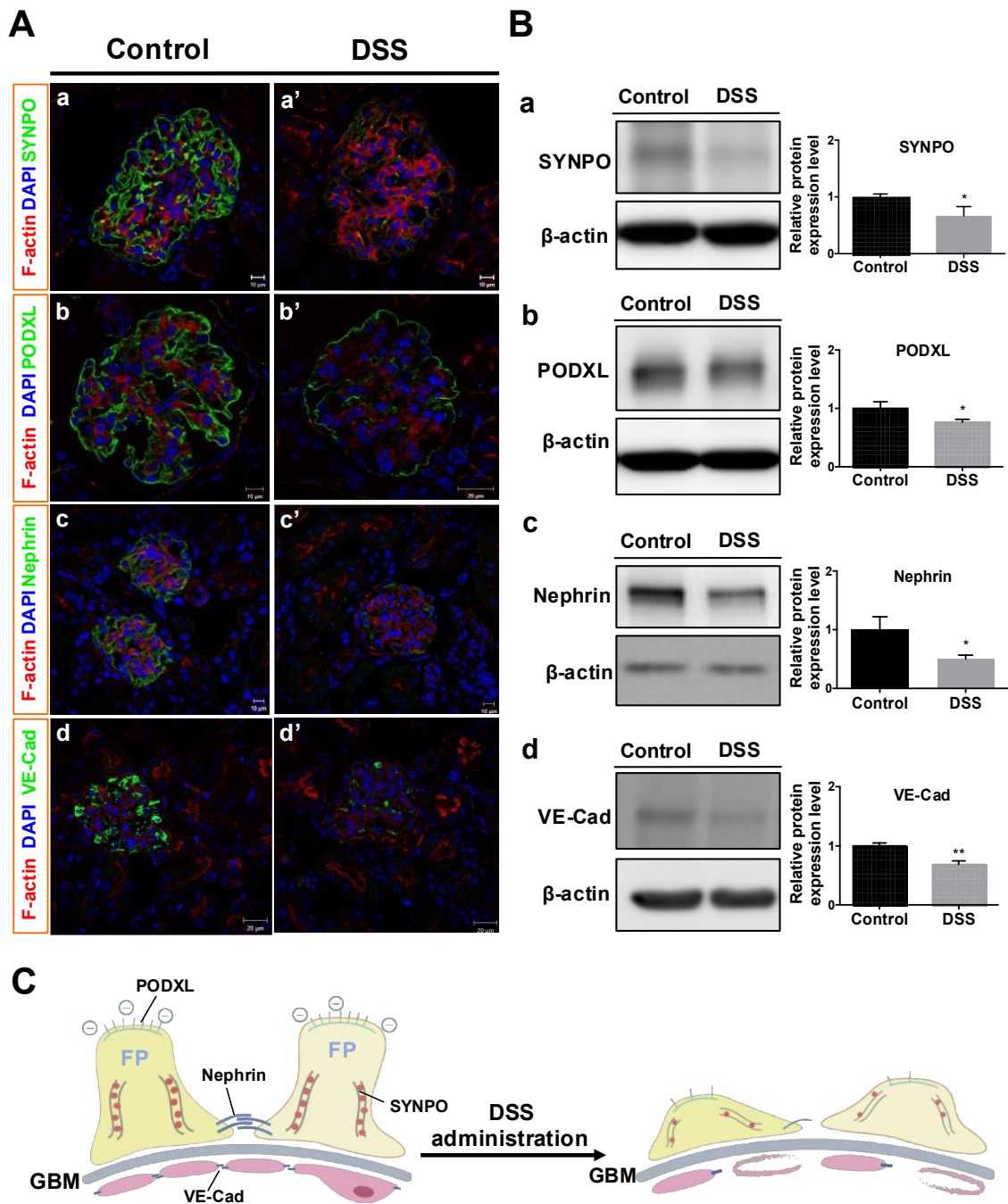


**Figure 2. 6.** Changes in GFB-related proteins in mice after DSS administration. Immunofluorescent microscopy (A) and Western blot analysis of protein expression (B) against synaptopodin (A-a, A-a'; B-a; 100 kDa), podocalyxin (A-b, A-b'; B-b; 130 kDa), nephrin (A-c, A-c'; B-c; 185 kDa) and VE-cadherin (A-d, A-d'; B-d; 130 kDa) in glomeruli were conducted for control and DSS-colitis mice. (B) Representative bands (left), and relative band intensity ratios (right) were analyzed. (C) Illustration of GFB-related proteins changes in this study. All values are means  $\pm$  SEM ( $n = 6$ ), \*  $p < 0.05$  and \*\*  $p < 0.01$  vs. control. Scale bars = 10  $\mu\text{m}$  (A-a, A-a', A-b, A-c, A-c'); 20  $\mu\text{m}$  (A-b', A-d, A-d'). **Abbreviation:** SYNPO, synaptopodin; PODXL, podocalyxin; VE-Cad, VE-cadherin; FP, foot processes.

### 2.3.5. Inflammatory Cytokines and Mediators in Kidneys after DSS Administration

To investigate inflammation in the kidney after DSS administration colitis, western blot analysis against inflammatory cytokines and mediators were performed. The results showed that protein levels of inflammatory cytokines TNF- $\alpha$ , IL-6 and TGF- $\beta$ 1, as well as inflammatory mediators COX-2 and iNOS, were higher than those in controls (Figure 2.7). These data indicated that increasing expression of proinflammatory cytokines in renal tissue were involved in DSS-induced colitis mouse model.

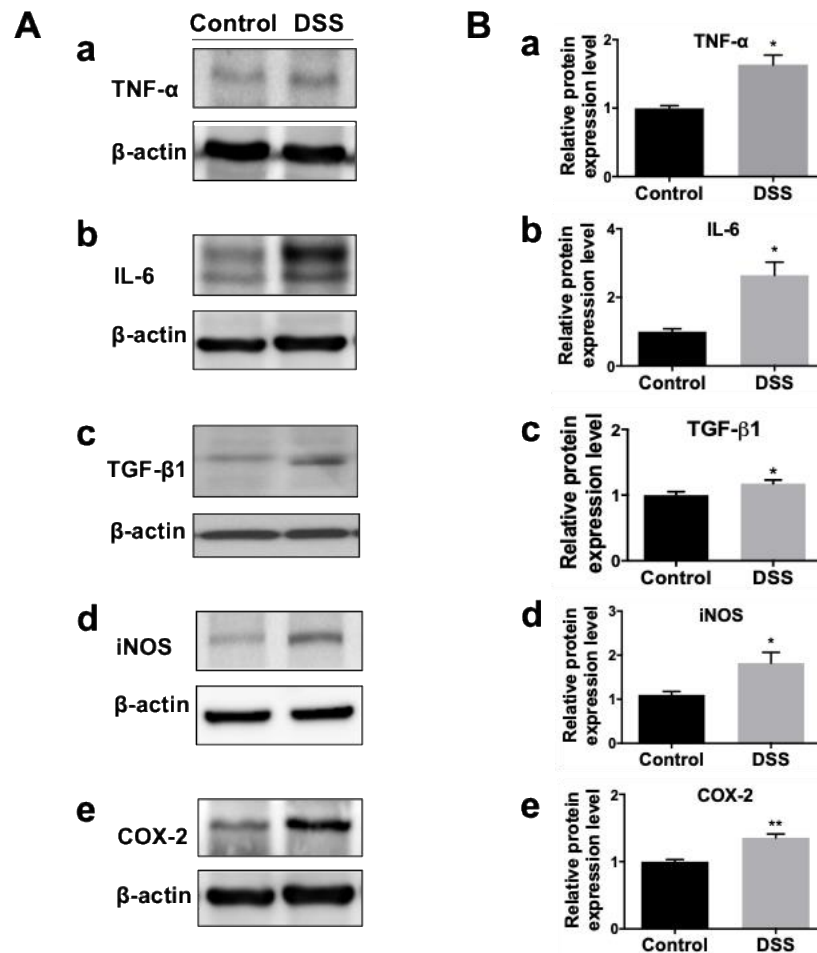


**Figure 2. 7.** The protein expressions of inflammatory cytokines and mediators in renal cortex after DSS administration. Western blot analysis of protein expression against TNF- $\alpha$  (a), IL-6 (b), TGF- $\beta$ 1 (c), iNOS (d) and COX-2 (e) in renal cortex from each group were detected. Representative bands are shown (A), and the relative band intensity ratio was analyzed (B). All the values are expressed as mean  $\pm$  SEM (n = 6 mice), \* $p$  < 0.05, \*\* $p$  < 0.01 vs. the control. **Abbreviation:** TNF- $\alpha$ , tumor necrosis factor- $\alpha$ ; IL-6, interleukin-6; TGF- $\beta$ 1, transforming growth factor- $\beta$ 1 (TGF- $\beta$ 1).

## 2.4. Discussions

Renal manifestations and complications in patients with IBD have been reported in several clinical and experimental studies from recent years [10–17,39]. However, the coexistence of renal disease and IBD, and the related glomerular structural changes in particular, have rarely been discussed. This study provided novel data showing not only the changes in renal glomerular collagen types in a DSS-induced colitis mouse model, but also revealed the interesting fact that proteins located on both the glomerular podocyte slit diaphragm and endothelial junction declined in expression in DSS-colitis mice, reflecting GFB damage.

This study adopted the DSS-induced colitis mouse model and confirmed symptoms of DSS-induced colitis such as body weight loss, diarrhea, gross bleeding and colon architecture destruction (Figures 1, 2), similar to IBD symptoms in humans [18,40]. Although some previous reports have mentioned that DSS might influence kidney function in mice after observing acute inflammatory responses associated with pro-inflammatory cytokine and chemokine expression in both intestines and kidneys, as well as renal tubular injury [21,22], the glomerular damage, especially the GFB damage in this DSS model still lacks detailed evidence. In this study, detailed investigations into changes in the renal glomerular histology, GBM, and GFB-related protein expression were conducted, to illustrate renal damage in the DSS-induced colitis mouse model.

I noticed that kidney size and weight were decreased in DSS-colitis mice after DSS administration (Figure 3), since kidney size and weight are important indicators of renal pathology during disease development [41]. The decreased kidney size may correlate with body weight loss [41,42], and this phenomenon has been found in human patients with

IBD [43]. Moreover, PAS staining revealed increasing deposition of glycoprotein matrix in GBM and mesangium, and Masson's trichome staining revealed collagen deposition was markedly increased around the glomerulus and Bowman's capsules in DSS-colitis mice. Such matrix and collagen depositions in glomeruli were also found in glomerular impairment, implicating excess ECM production as a factor in glomerular disease [38,44,45]. These observations suggest the DSS mice might show some glomerular abnormality.

To clarify the assumption that DSS induces renal structural change, the changes in specific types of collagens in the glomeruli were investigated. The results in this study showed that COL4 was decreased in the GBM, whereas COL1 and COL5 increased in the renal glomerular capillary loops and interstitium of DSS-colitis mice (Figure 4). COL4 is well known to be the major component of the ECM in GBM, Bowman's capsule and tubular basement membranes in normal kidneys [46]. Decreased expression of COL4 in GBM has been reported with the increased GBM degradation associated with kidney dysfunction [46–49]. On the other hand, COL1 and COL5 belong to interstitial ECM and excessive deposition is known to form scar tissue in the interstitial space during fibrosis [50,51]. In fact, COL1 seldom appears in renal vessels and glomeruli under normal conditions but is deposited in the early stage of renal fibrosis [38,50]. COL5 has been reported to spread widely in glomeruli during glomerulopathy, wound healing and kidney development [37,52,53]. This present study of a decrement in COL4 in GBM and increments in both COL1 and COL5 in renal glomerular capillary loops and interstitium suggested that DSS administration could cause these collagens changes, which may lead to glomerular structure damage.

Renal disease has been reported in human IBD patients, but GFB-related protein changes have not been closely investigated. The present study investigated four proteins (synaptopodin, podocalyxin, nephrin and VE-cadherin) to clarify GFB damage, because these proteins have not been investigated in the kidneys of DSS-colitis mice, and the relevance of GBM damage in the DSS-induced colitis mouse model has not been reported yet. This present study showed declined expression of all four proteins in glomeruli after DSS administration (Figure 5). Podocytes locating on the GBM are known to serve as the final filtration barriers of glomeruli and contain the special proteins synaptopodin, podocalyxin and nephrin. These proteins have been suggested to represent important biomarkers of podocyte deficiency [54]. Synaptopodin is known to maintain podocyte foot processes and downregulation of the podocyte actin cytoskeleton has been observed in human and rodent glomerular diseases [54]. Decreased synaptopodin expression in podocytes reflects the foot processes are associated with a loss of cytoskeletal destruction [55]. Podocalyxin is a highly electronegative sialoglycoprotein located at the apical surface of podocyte foot processes and functions to maintain the negative charge of the glomerular filtration slit diaphragm and podocyte shape by linking to the actin cytoskeleton [56]. *In vivo* and *in vitro* studies have reported that decreased podocalyxin is associated with reduced adhesiveness of cells to the GBM [54,56]. Moreover, the loss of nephrin, a structural protein located between the podocyte foot processes, causes decreased podocyte integrity of slit diaphragms, resulting in eventual damage to the GFB [25,57]. Furthermore, glomerular endothelial cells serve as the first filtration barrier through their tight adhesion to the basement membrane, and a decrease in endothelial cells can therefore worsen renal failure [26,27]. VE-cadherin is an adherens junction protein between endothelial cells that

maintains vascular integrity and decreased VE-cadherin expression has been observed in the glomerular endothelium of end-stage renal disease patients [58–60].

Abnormal immune response as shown by the high levels of the inflammatory cytokines and mediators such as TNF- $\alpha$ , IL-6, TGF- $\beta$ 1, iNOS and COX-2 were investigated in inflamed biopsy areas from both Ulcerative colitis and Crohn's disease IBD patients [39, 61–64]. The effect of these cytokines on the intestine has been directly related to the induction of tissue injury. However, the influence of the above inflammatory cytokines on renal injury of IBD patients still remains unclear. In this study, higher expression of inflammatory cytokines including TNF- $\alpha$ , IL-6 and TGF- $\beta$ 1, as well as inflammatory mediators iNOS and COX-2 were discovered in the renal tissue of DSS-colitis mice. Those inflammatory cytokines and mediators have been detected in serum of IBD patients. Thus, this study revealed that renal inflammation was involved in this DSS-induced colitis mouse model.

Taken together, the results in this chapter imply that DSS administration could cause the glomerular collagen changes, including decreased COL4 as a supporting ECM of GBM structure and deposition of COL1 and COL5 in renal interstitium. These collagen changes might lead to structural damage to podocytes such as a loss of polarity and detachment from the GBM, as well as loss of endothelial cell junctions, eventually causing renal disease. Loss of the podocyte cytoskeletal proteins synaptopodin and podocalyxin and the slit diaphragms protein nephrin, as well as the defective endothelial cells adherens junction protein (VE-cadherin) which may be associated with podocyte damage. On the other hand, renal inflammation may involve in IBD related extraintestinal manifestations and complications through the increased levels of inflammatory cytokines and mediators.

Based on these findings, the lack or insufficiency of these GFB-related proteins in DSS-colitis mice might cause glomerular structural damage, and consequently lead to damage not only to podocytes, but also to adherens junctions in the vasculature, which might result in GFB damage.

## 2.5. Conclusion

In conclusion, this study used the DSS-induced colitis mouse model, a very common experimental model of colitis, and clarified changes in glomerular collagens and GFB-related proteins after DSS administration. This study showed similar phenomena to the IBD patients with renal disease, which indicated that this DSS-induced colitis mouse model could lead to novel uses of the animal model for further investigations into IBD-associated renal disease.

## References

1. Sartor, R.B. Current concepts of the etiology and pathogenesis of ulcerative colitis and Crohn's disease. *Gastroenterol. Clin. N. Am.* **1995**, *24*, 475–507.
2. Ricart, E.; Panaccione, R.; Loftus, E.V.; Tremaine, W.J.; Harmsen, W.S.; Zinsmeister, A.R.; Sandborn, W.J. Autoimmune disorders and Extraintestinal manifestations in First-degree familial and sporadic inflammatory bowel disease. *Inflamm. Bowel Dis.* **2004**, *10*, 207–214.
3. Nemeth, Z.H.; Bogdanovski, D.A.; Barratt-Stopper, P.; Paglinco, S.R.; Antonioli, L.; Rolandelli, R.H. Crohn's Disease and Ulcerative Colitis Show Unique Cytokine Profiles. *Cureus.* **2017**, *9*, e1177.

4. Ince, M.N.; Elliott, D.E. Immunologic and molecular mechanisms in inflammatory bowel disease. *Surg. Clin. N. Am.* **2007**, *87*, 681–696.
5. Elsässer-Beile, U.; von Kleist, S.; Gerlach, S.; Gallati, H.; Mönting, J.S. Cytokine production in whole blood cell cultures of patients with Crohn's disease and ulcerative colitis. *J. Clin. Lab. Anal.* **1994**, *8*, 447–451.
6. Sklyarov, A.Y.; Panasyuk, N.B.; Fomenko, I.S. Role of nitric oxide-synthase and cyclooxygenase/ lipooxygenase systems in development of experimental ulcerative colitis. *J. Physiol. Pharmacol.* **2011**, *62*, 65–73.
7. Hosoi, T.; Goto, H.; Arisawa, T.; Niwa, Y.; Okada, N.; Ohmiya, N.; Hayakawa, T. Role of nitric oxide synthase inhibitor in experimental colitis induced by 2,4,6-trinitrobenzene sulphonic acid in rats. *Clin. Exp. Pharmacol. Physiol.* **2001**, *28*, 9–12.
8. Christodoulou, D.K.; Katsanos, K.H.; Kitsanou, M.; Stergiopoulou, C.; Hatzis, J.; Tsianos, E.V. Frequency of extraintestinal manifestations in patients with inflammatory bowel disease in northwest Greece and review of the literature. *Dig. Liver Dis.* **2002**, *34*, 781–786.
9. Scott, R.P.; Quaggin, S.E. The cell biology of renal filtration. *J Cell Biol.* **2015**, *209*, 119–210.
10. Ambruzs, J.M.; Walker, P.D.; Larsen, C.P. The histopathologic spectrum of kidney biopsies in patients with inflammatory bowel disease. *Clin. J. Am. Soc. Nephrol.* **2014**, *9*, 265–270.
11. Ambruzs, J.M.; Larsen, C.P. Renal Manifestations of Inflammatory Bowel Disease. *Rheum. Dis. Clin. N. Am.* **2018**, *44*, 699–714.
12. Rabin, B.S.; Rogers, S. Pathologic changes in the liver and kidney produced by immunization with intestinal antigens. *Am. J. Pathol.* **1972**, *84*, 201–210.
13. Kreisel, W.; Wolf, L.M.; Grotz, W.; Grieshaber, M. Renal tubular damage: An extraintestinal manifestation of chronic inflammatory bowel disease. *Eur. J. Gastroenterol. Hepatol.* **1996**, *8*, 461–468.

14. Khosroshahi, H.T.; Shoja, M.M. Tubulointerstitial disease and ulcerative colitis. *Nephrol. Dial. Transplant.* **2006**, *21*, 2340.
15. Corica, D.; Romano, C. Renal Involvement in Inflammatory Bowel Diseases. *J. Crohns Colitis* **2016**, *10*, 226–235.
16. Fraser, J.S.; Muller, A.F.; Smith, D.J.; Newman, D.J.; Lamb, E.J. Renal tubular injury is present in acute inflammatory bowel disease prior to the introduction of drug therapy. *Aliment. Pharmacol. Ther.* **2001**, *15*, 1131–1137.
17. Tokuyama, H.; Wakino, S.; Konishi, K.; Hashiguchi, A.; Hayashi, K.; Itoh, H. Acute interstitial nephritis associated with ulcerative colitis. *Clin. Exp. Nephrol.* **2010**, *14*, 483–486.
18. Chassaing, B.; Aitken, J.D.; Malleshappa, M.; Vijay-Kumar, M. Dextran Sulfate sodium (DSS)-induced Colitis in mice. *Trends Pharmacol. Sci.* **2014**, *104*, doi:10.1002/0471142735.im1525s104
19. de Lange, K.M.; Barrett, J.C. Understanding inflammatory bowel disease via immunogenetics. *J. Autoimmun.* **2015**, *64*, 91–100.
20. Eichele, D.D.; Kharbanda, K.K. Dextran sodium sulfate colitis murine model: An indispensable tool for advancing our understanding of inflammatory bowel diseases pathogenesis. *World J. Gastroenterol.* **2017**, *23*, 6016–6029.
21. Ranganathan, P.; Jayakumar, C.; Santhakumar, M.; Ramesh, G. Netrin-1 regulates colon-kidney cross talk through suppression of IL-6 function in a mouse model of DSS-colitis. *Am. J. Physiol. Renal Physiol.* **2013**, *304*, 1187–1197.
22. Ranganathan, P.; Jayakumar, C.; Manicassamy, S.; Ramesh, G. CXCR2 knockout mice are protected against DSS-colitis-induced acute kidney injury and inflammation. *Am. J. Physiol. Renal Physiol.* **2013**, *305*, 1422–1427.
23. Meyer, T.W. Tubular injury in glomerular disease. *Kidney Int.* **2003**, *63*, 774–787.

24. Kriz, W.; LeHir, M. Pathways to nephron loss starting from glomerular diseases- Insights from animal models. *Kidney Int.* **2005**, *67*, 404–419.
25. Lennon, R.; Randles, M.J.; Humphries, M.J. The Importance of Podocyte Adhesion for a Healthy Glomerulus. *Front. Endocrinol.* **2014**, *5*, 160.
26. Arif, E.; Nihalani, D. Glomerular Filtration Barrier Assembly: An insight. *Postdoc. J.* **2013**, *1*, 33–45.
27. Scott, R.P.; Quaggin, S.E. The cell biology of renal filtration. *J. Cell Biol.* **2015**, *209*, 199–210.
28. Miner, J.H. Glomerular basement membrane composition and the filtration barrier. *Pediatr. Nephrol.* **2011**, *26*, 1413–1417.
29. Byron, A.; Randles, M.J.; Humphries, J.D.; Mironov, A.; Hamidi, H.; Harris, S.; Mathieson, P.W.; Saleem, M.A.; Satchell, S.C.; Zent, R.; et al. Glomerular Cell Cross-Talk Influences Composition and Assembly of Extracellular Matrix. *J. Am. Soc. Nephrol.* **2014**, *25*, 953–966.
30. Chen, Y.M.; Miner, J.H. Glomerular basement membrane and related glomerular disease. *Transl. Res.* **2012**, *160*, 291–297.
31. Chew, C.; Lennon, R. Basement Membrane Defects in Genetic Kidney Diseases. *Front. Pediatr.* **2018**, *6*, 11.
32. Murthy, S.N.; Cooper, H.S.; Shim, H.; Shah, R.S.; Ibrahim, S.A.; Sedergran, D.J. Treatment of dextran sulfate sodium-induced murine colitis by intracolonic cyclosporine. *Dig. Dis. Sci.* **1993**, *38*, 1722–1734.
33. McManus, J.F. The Periodic Acid Routine Applied to the Kidney. *Am. J. Pathol.* **1948**, *24*, 643–653.
34. Cohen, A.H. Masson's trichrome stain in the evaluation of renal biopsies. An appraisal. *Am. J. Clin. Pathol.* **1976**, *65*, 631–643.

35. Nishimura, Y.; Hsu, H.H.; Wang, P.C. Detection of initial angiogenesis from dorsal aorta into metanephroi and elucidation of its role in kidney development. *Regener. Ther.* **2016**, *4*, 27–35.
36. Hsu, H.H.; Murasawa, Y.; Qi, P.; Nishimura, Y.; Wang, P.C. Type V collagen fibrils in mouse metanephroi. *Biochem. Biophys. Res. Commun.* **2013**, *441*, 649–654.
37. Nagao, T.; Suzuki, K.; Utsunomiya, K.; Matsumura, M.; Saiga, K.; Wang, P.C.; Minamitani, H.; Aratani, Y.; Nakayama, T.; Suzuki, K. Direct activation of glomerular endothelial cells by anti-moesin activity of anti-myeloperoxidase antibody. *Nephrol. Dial. Transplant.* **2011**, *26*, 2752–2760.
38. Genovese, F.; Manresa, A.A.; Leeming, D.; Karsdal, M.; Boor, P. The extracellular matrix in the kidney: A source of novel non-invasive biomarkers of kidney fibrosis. *Fibrogenes. Tissue Repair* **2014**, *7*, 4.
39. Levine, J.S.; Burakoff, R. Extraintestinal manifestations of inflammatory bowel disease. *Gastroenterol. Hepatol.* **2011**, *7*, 235–241.
40. Da Silva, A.P.; Pollett, A.; Rittling, S.R.; Denhardt, D.T.; Sodek, J.; Zohar, R. Exacerbated tissue destruction in DSS-induced acute colitis of OPN-null mice is associated with downregulation of TNF- $\alpha$  expression and non-programmed cell death. *J. Cell Physiol.* **2006**, *208*, 629–639.
41. Sandilands, E.A.; Dhaun, N.; Dear, J.W.; Webb, D.J. Measurement of renal function in patients with chronic kidney disease. *Br. J. Clin. Pharmacol.* **2013**, *76*, 504–515.
42. Emamian, S.A.; Nielsen, M.B.; Pedersen, J.F.; Ytte, L. Kidney dimensions at sonography: Correlation with age, sex, and habitus in 665 adult volunteers. *Am. J. Roentgenol.* **1993**, *160*, 83–86.
43. Lauritzen, D.; Andreassen, B.U.; Heegaard, N.H.H.; Klinge, L.G.; Walsted, A.M.; Neland, M.; Nielsen, R.G.; Wittenhagen, P. Pediatric Inflammatory Bowel Diseases: Should We Be Looking for Kidney Abnormalities? *Inflamm. Bowel Dis.* **2018**, *24*, 2599–2605.

44. Kashgarian, M.; Sterze, B. The pathobiology of the mesangium. *Kidney Int.* **1992**, *41*, 524–529.
45. Duffield, J.S. Cellular and molecular mechanisms in kidney fibrosis. *J. Clin. Investig.* **2014**, *124*, 2299–2306.
46. Miner, J.H. Renal basement membrane components. *Kidney Int.* **1999**, *56*, 2016–2024.
47. Niu, H.; Li, Y.; Li, H.; Chi, Y.; Zhuang, M.; Zhang, T.; Liu, M.; Nie, L. Matrix metalloproteinase 12 modulates high-fat-diet induced glomerular fibrogenesis and inflammation in a mouse model of obesity. *Sci. Rep.* **2016**, *6*, 20171.
48. Tamsma, J.T.; van den Born, J.; Bruijn, J.A.; Assmann, K.J.; Weening, J.J.; Berden, J.H.; Wieslander, J.; Schrama, E.; Hermans, J.; Veerkamp, J.H. Expression of glomerular extracellular matrix components in human diabetic nephropathy: Decrease of heparan sulphate in the glomerular basement membrane. *Diabetologia* **1994**, *37*, 313–320.
49. Morita, M.; Uchigata, Y.; Hanai, K.; Ogawa, Y.; Iwamoto, Y. Association of urinary type IV collagen with GFR decline in young patients with type 1 diabetes. *Am. J. Kidney Dis.* **2011**, *58*, 915–920.
50. Yoshioka, K.; Tohda, M.; Takemura, T.; Akano, N.; Matsubara, K.; Ooshima, A.; Maki, S. Distribution of type I collagen in human kidney diseases in comparison with type III collagen. *J. Pathol.* **1990**, *162*, 141–148.
51. Sumiyoshi, H.; Kitamura, H.; Matsuo, N.; Tatsukawa, S.; Ishikawa, K.; Okamoto, O.; Fujikura, Y.; Fujiwara, S.; Yoshioka, H. Transient expression of mouse Pro- $\alpha$ 3(V) collagen gene (Col5a3) in wound healing. *Connect. Tissue Res.* **2012**, *5*, 313–317.
52. Morita, H.; Hasegawa, T.; Minamoto, T.; Oda, Y.; Inui, K.; Tayama, H.; Nakao, N.; Nakamoto, Y.; Ideura, T.; Yoshimura, A. Collagenofibrotic glomerulopathy with a widespread expression of type-v collagen. *Virchows Arch.* **2003**, *442*, 163–168.

53. Murasawa, Y.; Hayashi, T.; Wang, P.C. The role of type V collagen fibril as an ECM that induces the motility of glomerular endothelial cells. *Exp. Cell Res.* **2008**, *314*, 3638–3653.
54. Sekulic, M.; Pichler, S. A compendium of urinary biomarkers indicative of glomerular podocytopathy. *Pathol. Res. Int.* **2013**, *2013*, 782395.
55. Kwon, S.K.; Kim, S.J.; Kim, H.Y. Urine synaptopodin excretion is an important marker of glomerular disease progression. *Korean J. Intern Med.* **2016**, *31*, 938–943.
56. Nielsen, J.S.; McNagny, K.M. The role of podocalyxin in health and disease. *J. Am. Soc. Nephrol.* **2009**, *20*, 1669–1676.
57. Greka, A.; Mundel, P. Cell biology and pathology of podocytes. *Annu. Rev. Physiol.* **2012**, *74*, 299–323.
58. Spagnuolo, R.; Corada, M.; Orsenigo, F.; Zanetta, L.; Deuschle, U.; Sandy, P.; Schneider, C.; Drake, C.J.; Breviario, F.; Dejana, E. Gas1 is induced by VE-cadherin and vascular endothelial growth factor and inhibits endothelial cell apoptosis. *Blood* **2004**, *103*, 3005–3012.
59. Giannotta, M.; Trani, M.; Dejana, E. VE-Cadherin and endothelial Adherens Junctions: Active guardians of vascular integrity. *Dev. Cell* **2013**, *26*, 441–454.
60. Hernandez, N.M.; Casselbrant, A.; Joshi, M.; Johansson, B.R.; Sumitran-Holgersson, S. Antibodies to kidney endothelial cells contribute to a “leaky” glomerular barrier in patients with chronic kidney diseases. *Am. J. Physiol. Renal Physiol.* **2012**, *302*, F884–F894.
61. Korolkova, O.Y.; Myers, J.N.; Pellom, S.T.; Wang, L.; M'Koma A.E. Characterization of Serum Cytokine Profile in Predominantly Colonic Inflammatory Bowel Disease to Delineate Ulcerative and Crohn's Colitides. *Clin Med Insights Gastroenterol.* **2015**, *8*, 29–44.

62. Wedrychowicz, A.; Kowalska-Duplaga, K.; Jedynek-Wasowicz, U.; Pieczarkowski, S.; Sladek, M.; Tomasik, P.; Fyderek, K. Serum concentrations of VEGF and TGF- $\beta$ 1 during exclusive enteral nutrition in IBD. *J Pediatr Gastroenterol Nutr.* **2011**, *53*, 150–155.
63. Sturm, A.; Schulte, C.; Schatton, R.; Becker, A.; Cario, E.; Goebell, H.; Dignass, AU. Transforming growth factor-beta and hepatocyte growth factor plasma levels in patients with inflammatory bowel disease. *Eur J Gastroenterol Hepatol.* **2000**, *12*, 445–450.
64. Neurath, M.F. Cytokines in inflammatory bowel disease. *Nat Rev Immunol.* **2014**, *14*, 329–342.

---

## Chapter III

# Development of an *In Vitro* Renal Disease Model to Study the Influence on Mesangial Cell Behavior

---

### 3.1. Introduction

Kidney disease due to acute kidney injury and/or chronic kidney diseases is frequent in different diseases and disorders, such as glomerulonephritis, inflammatory bowel diseases (IBD), diabetic nephropathy and renal fibrosis [1–3]. It is characterized by reduced kidney function, which includes mesangial cell (MC) proliferation and glomerular and tubular damage with loss of glomerular filtration function [3].

Mesangium expansion, caused by aberrant mesangial cell proliferation, is a common histopathological abnormality widely found, not only in glomerular diseases, but also in IBD-associated renal disease [1,2]. Over-proliferation of MCs can lead to accumulation of excessive extracellular matrix (ECM) in the mesangial matrix (MM) [4,5]. The accumulated ECM then results in renal fibrosis, and finally leads to end-stage renal failure [6].

MCs are specialized cells of the renal glomerulus and are located in the center of the intercapillary region that sits between the capillary loops. Figure 3.1 shows the illustration of glomerulus morphology and structure in normal and diseased glomeruli. MCs are

---

embedded in the MM that they secrete and are attributed an important role in controlling blood flow by contracting themselves to regulate the size of the capillary lumen [1,7]. Normal MCs have an irregular stellate shape with numerous pseudopods extending into the MM and are connected to the glomerular basement membrane *in vivo* [8]. Fusiform and elongated MCs indicate a high proliferative rate, whereas the stellate cells have a very humble growth response [9]. In addition, normal adult MCs extend actin filament contained bundles beneath the endothelium toward the mesangial angles of the glomerular basement membrane (GBM) where they are attached to the GBM [10-11]. This process in normal differentiated MCs is limited to express the subtype of actin protein,  $\beta$ - and  $\gamma$ -cytoplasmic actins [12]. There is little or no alpha-smooth muscle actin ( $\alpha$ -SMA) expressed in normal adult MCs *in vivo*. However, MCs express  $\alpha$ -SMA during embryonic development and in experimental and human glomerular disease [13]. MCs form myofibroblasts and express  $\alpha$ -SMA, which is considered a marker of MC activation and proliferation during glomerular injury and disease [1,10–12]. Activated and proliferated MCs in injured glomeruli secrete inflammatory mediators and produce excessive abnormal ECM components which lead to mesangium expansion [1,4,5]. Hence, MCs are critical players in the initiation and progression of several glomerular diseases [1,14].

MCs are also responsible for generating and controlling MM turnover, which provides structural support for the glomerular capillary structure [15]. MM is a basement membrane-like structure that is predominantly composed of type IV collagen (COL4), laminin, fibronectin and heparan sulfate proteoglycan under normal conditions *in vivo* [9,16]. Within these ECM components, COL4 forms the major skeleton of MM [16,17]. In diseased conditions, interstitial matrix components, such as type I collagen (COL1) and fibronectin, have been reported to accumulate in MM, and they directly result in

mesangium expansion and contribute to a variety of glomerular diseases [2,9]. COL1 is the main interstitial ECM component, and does not appear in normal MM [18]. My previous study indicated that altered glomerular collagen components, including an increase in COL1 and a decrease in COL4, are involved in an IBD animal model [2]. Other previous studies using *in vitro* flat 2D culture systems have demonstrated that MCs cultured on COL1 gels result in increased proliferation and increased expression of COL1, fibronectin and transforming growth factor beta 1 (TGF- $\beta$ 1), compared to those cultured on COL4 gels [19–22], suggesting that abnormal MM components can alter cell functions. TGF- $\beta$ 1 is recognized as a key pro-fibrotic mediator that initially stimulates MC proliferation and promotes MM production, resulting in mesangium expansion [21]. Thus, modulation of TGF- $\beta$ 1 expression might be a physiologically based strategy to attenuate mesangium expansion and glomerular fibrosis.

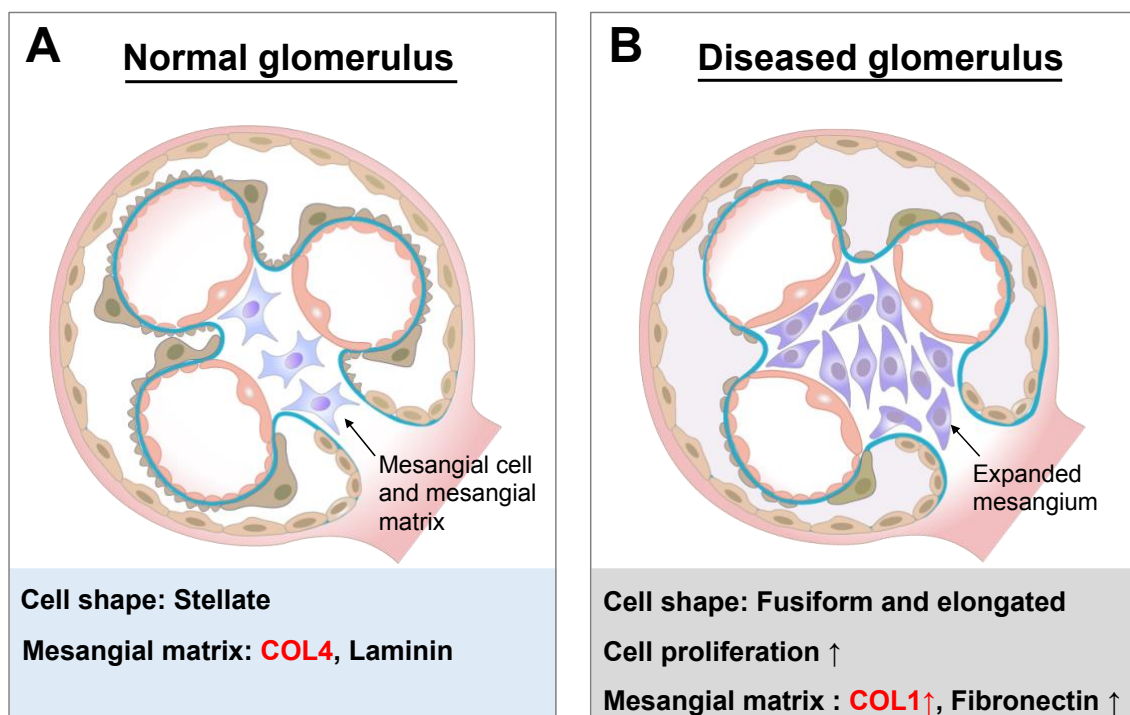


**Figure 3. 1.** Illustration of normal glomerulus morphology and structural changes in diseased glomerulus.  
**Abbreviation:** COL4, type IV collagen; COL1, type I collagen

Since the components of MM play a critical role in maintaining MC morphology, the structure of MM is important to regulate MC behavior, even for renal function [16]. However, the influence of a diseased MM 3D nanostructure on MC behavior is not yet understood. Native collagen fibers are arranged into a 3D structure and are around 300 nm to 1  $\mu\text{m}$  in diameter [23,24]. They are hierarchically structured from collagen fibrils in 40 to 100 nm diameters that are identifiable in the MM [25]. In addition, the renal basement membrane consists of a meshwork-forming structure with pores ranging from 4 to 50 nm [26]. The varying diameter of collagen fibers is correlated with health and disease conditions [27]. Thus, it is very important to investigate the cell behavior response to native nano-topologies. To address these issues, advanced nanofabrication techniques, such as electron beam lithography (EBL), offer novel tools to closely mimic the *in vivo* natural structure and to elucidate the mechanisms that influence cell responses to ECM by creating various nanopatterned topographical features [28–30]. Although the precise mechanism underlying the cell behavior as influenced by nano-topography is still unclear, it is possible that cells recognize the changed microenvironment by sensing the ECM nano-topography, triggering ECM remodeling [31]. Therefore, mimicking the abnormal nano-topography in diseased environments is critical to understanding how cells modulate their cellular function and activities to respond to pathological change.

This chapter is aimed to develop an *in vitro* renal disease model to study the influence on mesangial cell behavior. Nanopatterning to mimic the diseased MM nano-topography was performed on a titanium dioxide ( $\text{TiO}_2$ ) substrate by EBL and atomic layer deposition (ALD), as previously reported [32]. The influence of disease-mimic nanopatterned topographies on MC functions, including proliferation and expressions of specific types of ECM components, and comparing them with those of a normal-mimic nanopattern were

investigated. In addition, the possible mechanisms by which disease-mimic nanotopographical features influence MC behavior were also investigated. The results showed that the disease-mimic nanostructure guides MCs to display disease-like behavior. These findings are important for further establishing a disease model that mimics MM to study the molecular mechanisms of its pathogenesis, as well as to screen for and develop new drugs specific for patients with glomerular disease.

## **3.2. Materials and Methods**

### **3.2.1. Fabrication of Nanopatterned TiO<sub>2</sub> Substrates**

TiO<sub>2</sub> substrates were fabricated as previously described [33,34]. ZEP-520A positive-tone EBL resist (Nippon Zeon Co. Japan) was spin-coated on cleaned Si (100) substrates diluted in anisole (1:2 ratio) by a spin coater (Mikasa 1H-D7) at 6000 rpm, and then pre-baked at 180 °C for 3 min. Once the sample cooled to room temperature, a water-soluble conductive material called Espacer (Showa Denko Co. Japan) was spin-coated at 2000 rpm to obtain a very thin layer (10–20 nm). Next, the lithography patterns were written on the substrate with an EBL system (Elionix ELS-7500EX, acceleration voltage = 50 kV, electron beam (EB) amperage = 220 pA). The precise size of the fabricated substrate resulting from each EB was confirmed by scanning electron microscopy (SEM, FEG-SEM, Hitachi SU8230, Toronto ON, Canada). The exposed resist film was developed using n-amyl acetate and methyl isobutyl ketone (89%) /isopropyl alcohol (11%) (Wako Co. Japan), then rinsed by H<sub>2</sub>O and dried with nitrogen gas. The substrates were then etched by inductively coupled plasma-reactive ion etching at antenna power 50 W, bias 5W and

tetrafluoromethane flue with 6.5 standard cubic centimeter/minute (SCCM), followed by removing the resist film using O<sub>2</sub> plasma, dimethyl acetamide and SPM solution (H<sub>2</sub>SO<sub>4</sub> + H<sub>2</sub>O<sub>2</sub>, 3:1), respectively. The substrates were then coated with a photoresist (AZ-5214E, Germany) which is used as the mask for ALD, subjected to UV irradiation with a photomask, reversal baking at 120 °C, flood exposure to UV, and development by hexamethyl disilazane and 2.38% tetramethyl ammonium hydroxide (Wako Co. Japan) for 1 min, then rinsed with deionized water. Finally, the TiO<sub>2</sub> thin films were deposited on Si substrates using atomic layer deposition (Picosun SUNALE R-150) with 500 Pa of the chamber pressure and at 100 °C. The thickness of the TiO<sub>2</sub> layer was controlled by the number of cycles: 70 cycles gave a thickness of 5 nm. The TiO<sub>2</sub> precursor [tetra(dimethylamino)titanate] was pumped into the chamber, followed by argon gas to remove the undeposited precursor. Next, H<sub>2</sub>O vapor was pumped in to form the inorganic TiO<sub>2</sub> layer from the organic precursor, and then argon gas was pumped in to remove residual H<sub>2</sub>O. Fabricated TiO<sub>2</sub> nanopattern surfaces were characterized by SEM (SU8230) and atomic force microscopy (AFM, Ti950, Hysitron, MN, USA). Further experiments were performed using the fabricated substrates after dry heat sterilization of the substrate at 170 °C for 1 h. A non-patterned flat surface was used as a control. The fabrication process of Nanopatterned TiO<sub>2</sub> substrates is illustrated in Figure 3.2.

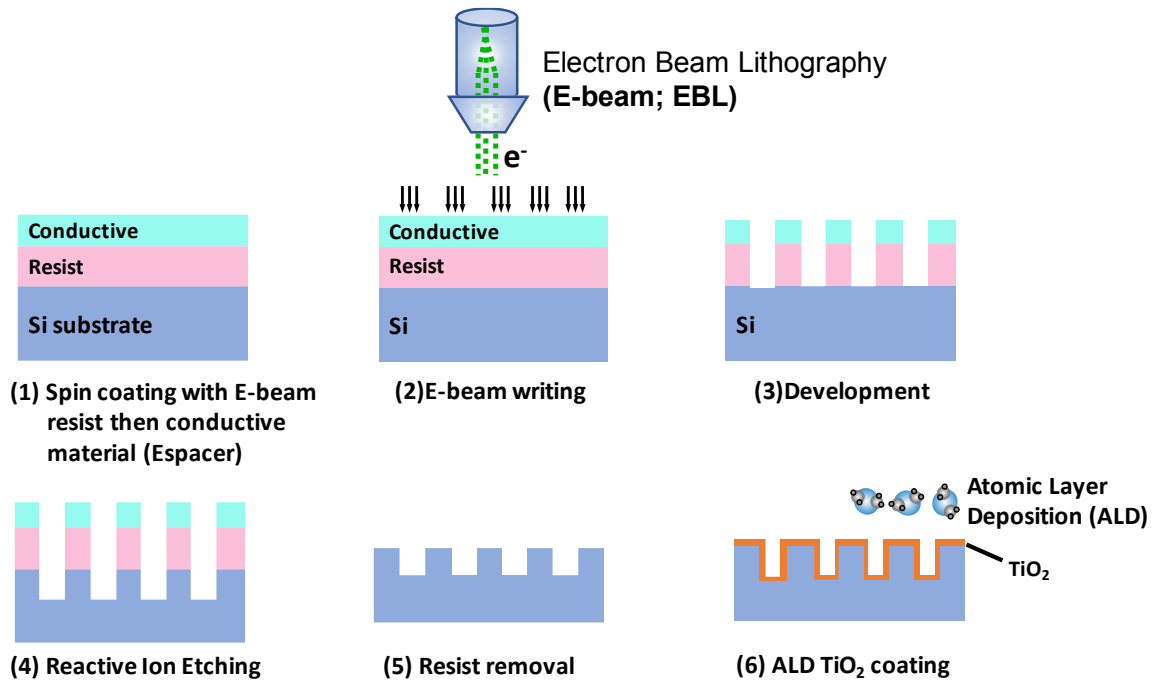


**Figure 3. 2.** Illustration of the steps required for nanopatterned TiO<sub>2</sub> substrates fabrication process.

### 3.2.2. Cell Culture

A mouse immortalized mesangial cell line, SV40MES13 (MES13), was purchased from the American Type Culture Collection (Manassas, VA, USA). Cells were cultured in a 3:1 mixture of Dulbecco's modified Eagle's medium (DMEM)/Ham's F12 medium (Nacalai Tesque, Kyoto, Japan) with supplemented 5% fetal bovine serum (FBS) (Corning Life Sciences, NY, USA), 14 mM HEPES (Gibco, MD, USA), 2 mM glutamine (Gibco) and 100 U/mL penicillin/streptomycin (Nacalai Tesque). Cells were incubated in a humidified incubator at 37 °C with 5% CO<sub>2</sub>. All experiments were performed between passages 8 and 9 to minimize the effects of phenotypic variation in continuous culture. Cells were serum-starved with 1% FBS for 24 h or 48 h prior to examination.

### **3.2.3. Cell Proliferation Assay**

The proliferation of cells grown on the nanopattern was evaluated by EdU incorporation using an EdU proliferation kit (iFluor 488) (Abcam, Cambridge, UK) and detected according to the manufacturer's instructions. Briefly, cells were seeded on various TiO<sub>2</sub> nanopatterns or flat substrate at a concentration of  $4 \times 10^4$  cells/well with serum-starved medium (1% FBS) for 24 and 48 hours in 24-well plates, then incubated with 10  $\mu$ M EdU solution for 2 h at 37 °C in 5% CO<sub>2</sub>. Subsequently, the cells were fixed with 4% formaldehyde for 15 min. After rinsing with 3% bovine serum albumin (BSA) in phosphate buffered saline (PBS, pH 7.4, Sigma-Aldrich, St. Louis, MO, USA), cells were permeated with 0.5% Triton X-100 in PBS, incubated with iFluor 488 azide, and stained with 300 nM 4', 6-diamidino-2-phenylindole (DAPI, Abcam) for 30 min. All images were acquired with a Zeiss LSM 510 META confocal microscope system (Carl Zeiss, Jena, Germany). At least 400 nuclei were counted per experiment.

### **3.2.4. Immunofluorescence Staining and Confocal Imaging**

Immunofluorescence staining was performed using a previously described method [2]. Briefly, cells were grown on TiO<sub>2</sub> nanopatterns for 24 or 48 h, then washed three times with PBS. Cells were fixed in 4% formaldehyde at room temperature for 20 min, permeabilized by 0.05% saponin (Sigma-Aldrich) in Tris-buffered saline (TBS, 50 mM Trizma, 150 mM NaCl, pH 7.6) for 15 min, then blocked by 3% BSA (Sigma, USA) in TBS for 1 h at room temperature. Then cells were sequentially incubated with primary antibodies against COL1, COL4,  $\alpha$ -SMA (Abcam), fibronectin, laminin  $\alpha$ 1 (Santa Cruz

Biotechnology, CA, USA), vinculin (Sigma-Aldrich), TGF- $\beta$ 1 (R&D Systems, Minneapolis, MN, USA) and integrin  $\alpha$ 5 $\beta$ 1 (Merck, Darmstadt, Germany), respectively, at 4 °C overnight followed by incubation with secondary antibodies conjugated to Alexa Fluor® 488 or 594 (Invitrogen, Carlsbad, CA, USA). Nuclei were stained with 1.5  $\mu$ M DAPI and double-stained with rhodamine-conjugated phalloidin (Life Technologies, Gaithersburg, MD, USA) to label the actin filament. All images were acquired with a Zeiss LSM 510 META confocal microscope system. The antibodies used in this study were listed in Table 3.1.

**Table 3. 1.** List of antibodies used in immunofluorescence staining.

<b>Primary antibodies used</b>	<b>Source</b>	<b>Host</b>
Type I collagen (COL1)	Abcam (ab34710)	Rabbit
Type IV collagen (COL4)	Abcam (ab6586)	Rabbit
$\alpha$ -SMA	Abcam (ab5694)	Rabbit
Fibronectin	SantaCruz (sc-271098)	Mouse
Laminin $\alpha$ 1	SantaCruz (sc-6017)	Goat
Vinculin	Sigma-Aldrich (V9131)	Mouse
TGF- $\beta$ 1	R&D Systems (MAB240)	Mouse
Integrin $\alpha$ 5 $\beta$ 1	Merck (MAB2514)	Rabbit
<b>Secondary antibodies used</b>	<b>Source</b>	<b>Host</b>
Anti-Rabbit IgG Alexa Fluor 488	Invitrogen (A11008)	Goat
Anti-mouse IgG Alexa Fluor 488	Abcam (ab150113)	Goat
Anti-Goat IgG Alexa Fluor 568	Invitrogen (A11079)	Rabbit

### 3.2.5. SEM for Cell Morphology

SEM images (SU8230) were used to investigate cellular morphology by following the method described previously [34]. After being grown on TiO<sub>2</sub> nanopatterns for 24 h, the cells were washed three times with PBS, fixed with 2.5% glutaraldehyde (Wako, Osaka,

Japan) at 4 °C for 2 h, followed by post-fixation in 1% osmium tetroxide in PBS for at least 24 h, and then dehydrated in gradient concentrations of ethanol (50% to 100%) for 10 min. Finally, cells were dried with hexamethyldisilazane and air-dried before observation by SEM.

### **3.2.6. Statistical Analysis**

Statistical analyses were performed using Prism 8 software (GraphPad, CA, USA). All data are expressed as means  $\pm$  standard error of the mean (SEM) from five replicates from each group in at least three independent experiments. The significance of differences between groups was analyzed using one-way Analysis of Variance (ANOVA) and Tukey's *post hoc* test for multiple comparisons. A probability level of  $p < 0.05$  was considered significant.

## **3.3. Results**

### **3.3.1. Design and Fabrication of Disease- and Normal-mimic Nanopatterned TiO<sub>2</sub> Substrates**

In this study, whether disease-mimic nano-topographical features would influence MC behavior by affecting cell morphology was examined. To investigate MC behavior influenced by disease-mimic nano-topographical features, three different fibril-forming nanopatterns were designed. In addition, one network-forming nanopattern and an unpatterned flat control were also used.

The nanopatterning in this study was inspired by the fact that the diameters of collagen fibrils in natural MM are 40 to 100 nm [25]. However, due to the limitations of the ALD of samples on the patterns fabricated by EBL, approximately 80 nm was the minimum dimension. The dimensions and topographical variations of fabricated nanopatterns were characterized with SEM and AFM as shown in Figure 3.3. To optimize the disease-mimic nanopattern, three different nano-gratings of fibril-forming nanopatterns were used: 1) F80/80 nanopattern with ridges and grooves of 80 nm in width; 2) F80/200 nanopattern with 80 nm ridges and 200 nm grooves and 3) F200/80 nanopattern with 200 nm ridges and 80 nm grooves, which mimic the collagen fibril and fibril spacing. The network-forming nanopattern mimics the normal MM nanostructure (normal-mimic) with pores approximately 50 nm in diameter, 80 nm spacing, and 80 nm in depth. All the nanopatterns were 80 nm in depth. The unpatterned flat substrate presented a comparatively smooth surface. SEM and AFM images showed that the dimensions of the ridge/groove-nanopatterns were highly uniform and well defined, without obvious defects.

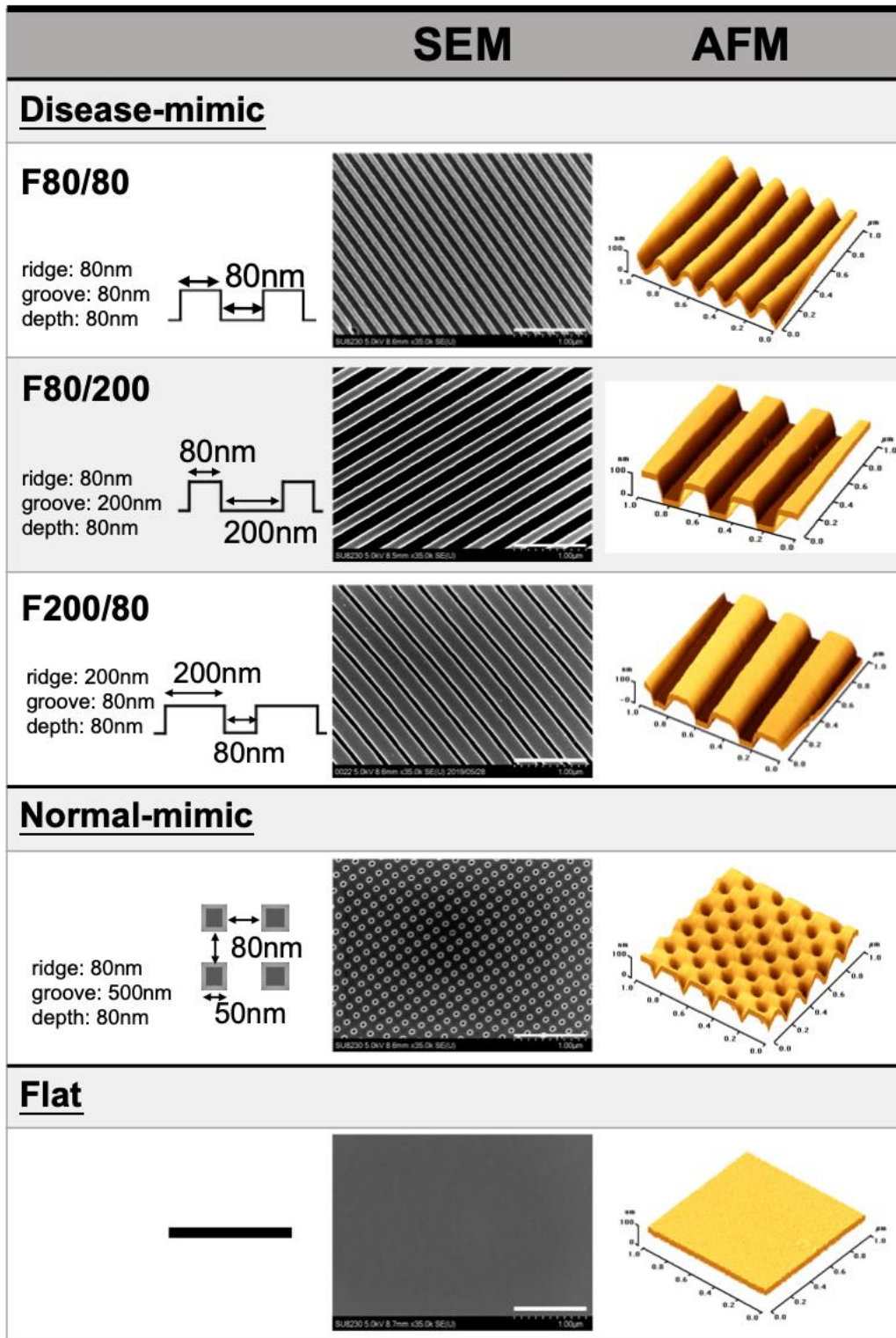


**Figure 3. 3.** Characterization of each fabricated titanium dioxide (TiO<sub>2</sub>) nanopatterns used in this study including groove/ridge width and depth. Scanning electron microscopy (SEM) was utilized to confirm the morphologies of three disease-mimic nanopatterns, normal-mimic nanopattern, and the flat control. Illustrations show the approximate dimensions of ridge/groove pattern arrays. Scale bar = 1  $\mu$ m. **Abbreviations:** SEM, scanning electron microscopy; AFM, atomic force microscopy.

### 3.3.2. MES13 Cell Proliferation on Disease-mimic Nanopatterns

Aberrant MC proliferation in mesangium is commonly observed in patients with glomerular disease [35,36]. To screen for nano-topographical features that closely mimic diseased MM, 5-ethynyl-2'-deoxyuridine (EdU) proliferation assays were performed by counting the percentage of MES13 cells with incorporated EdU, which indicates newly synthesized DNA (shown in green). Fluorescence images shown in Figure 3.4A and Figure 3.5A revealed EdU incorporation in the nuclei of cells after 24 and 48 hours of seeding on disease-mimic nanopatterns, including F80/80 (Figure 3.4a; 3.5a), F80/200 (Figure 3.4a; 3.5a), F200/80 (Figure 3.4c; 3.5c), normal-mimic nanopattern (Figure 3.4d; 3.5d) and flat control (Figure 3.4e; 3.5e). Figure 3.4B shows the percentage of EdU-positive cells after 24 hours of seeding. The results showed that a significant increase in cell proliferation was observed in cells cultured on disease-mimic nanopatterns, including F80/80, F80/200 and F200/80 after 24 hours of seeding. In addition, the proliferation of cells cultured on the F80/200 nanopattern was significantly higher than that of cells cultured on F80/80 and F200/80 nanopatterns. In contrast, cells grown on the normal-mimic nanopattern showed cell proliferation as low as those on the flat control.

Moreover, after 48 hours of seeding, the proliferation of cells cultured on the F80/200 nanopattern was significantly higher than that of cells cultured on other nanopatterns and flat control ( $p < 0.005$ ), whereas the decreased proliferation was shown in cell cultured on flat control. Figure 3.5B shows the percentage of EdU-positive cells after 48 hours of seeding.

These results revealed that the disease-mimic nanopattern F80/200 dramatically enhanced MES13 cell proliferation.

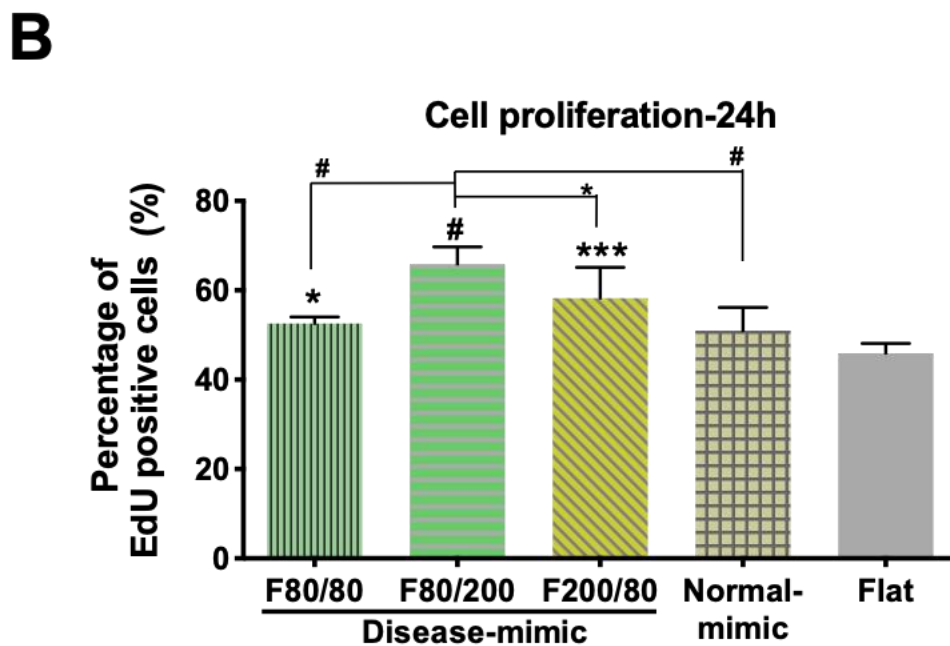
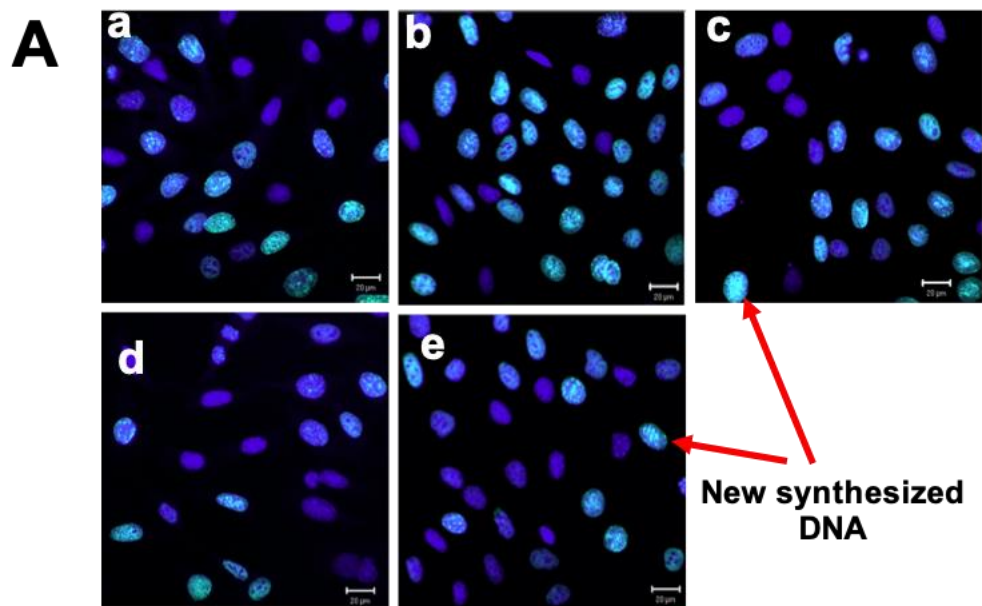
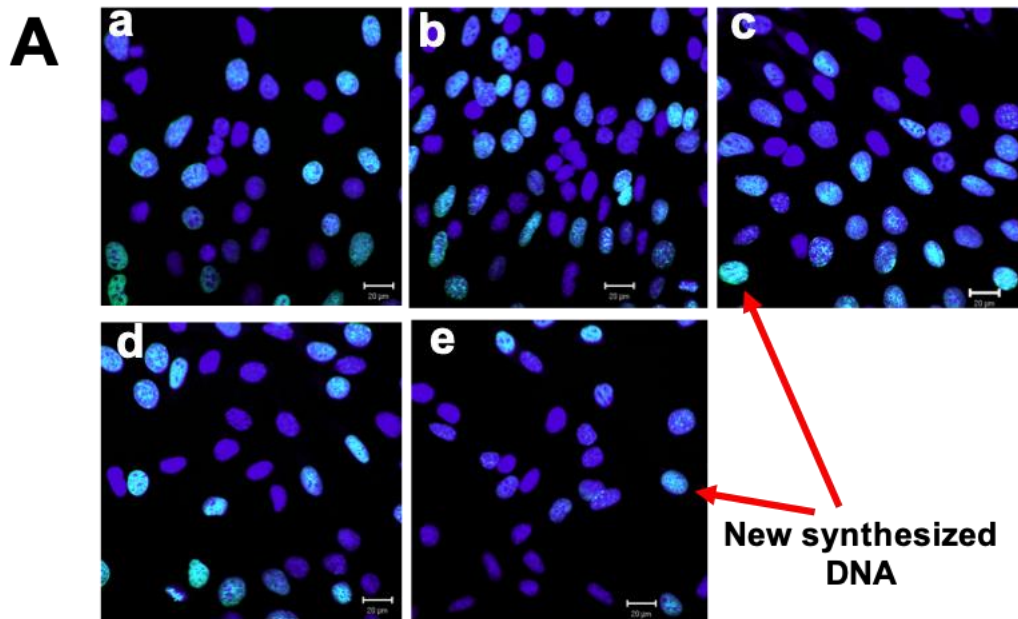


**Figure 3. 4.** Proliferation of MES13 cells cultured on disease- and normal-mimic nanopatterns. (A) Cells were cultured on F80/80 (a), F80/200 (b), F200/80 (c), normal-mimic (d) and flat control (e) for 24 h, and then proliferation was determined by the 5-ethynyl-2'-deoxyuridine (EdU) assay. Fluorescence images show EdU incorporation into the nuclei of cells. EdU-positive cells are green, and nuclei stained with 4',6-diamidino-2-phenylindole (DAPI) are blue. (B) Percentage of EdU-positive cells. Data are reported as means  $\pm$  SEM for three independent experiments. Statistically significant at \*  $p < 0.05$ , \*\*\*  $p < 0.001$ , and #  $p < 0.0001$  analysis of variance (ANOVA). Scale bar = 20  $\mu$ m.



**B**

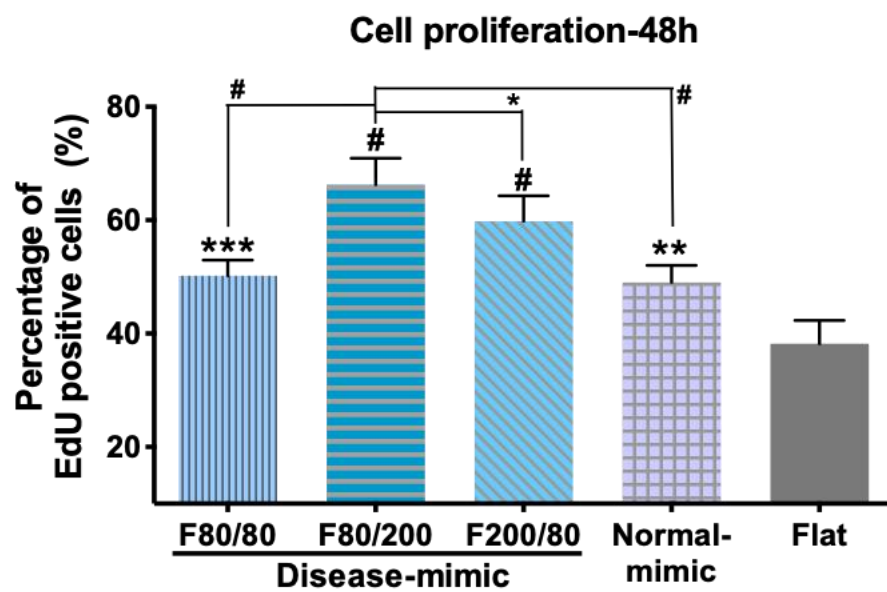


**Figure 3. 5.** Proliferation of MES13 cells cultured on disease- and normal-mimic nanopatterns. (A) Cells were cultured on F80/80 (a), F80/200 (b), F200/80 (c), normal-mimic (d) and flat control (e) for 48 h, and then proliferation was determined by EdU assay. (B) Percentage of EdU-positive cells. Data are reported as means  $\pm$  SEM for three independent experiments. Statistically significant at \*  $p < 0.05$ , \*\*  $p < 0.01$ , \*\*\*  $p < 0.001$ , and #  $p < 0.0001$  analysis of variance (ANOVA). Scale bar = 20  $\mu\text{m}$ .

### 3.3.3. Expressions of Specific ECM Components in MES13 Cells

One critical role of mesangial cells is to synthesize MM to provide support to glomerular capillaries [1]. To examine the influence of disease-mimic nanopatterns on ECM component expression in MES13 cells, immunofluorescence staining was performed for abnormal ECM component, COL1 and fibronectin and normal ECM component, COL4 and laminin  $\alpha 1$ , after cells were grown on TiO<sub>2</sub> nanopatterns for 48 h.

As the results show in Figure 3.6, increased COL1 (Figure 3.6A) and fibronectin (Figure 3.6B) expressions were detected in cells on the F80/80, F200/80 and particularly the F80/200 nanopattern, when compared to the normal-mimic nanopattern and flat control. In contrast, decreased COL4 expression was detected in cells grown on F80/80, F80/200 and F200/80 nanopatterns, compared to those grown on the normal-mimic nanopattern and flat control (Figure 3.7A). Consistently, an obvious decrease in laminin  $\alpha 1$  expression was observed in cells on F80/80, F80/200 and F200/80 nanopatterns (Figure 3.7B).

These results indicated that MES13 cells expressed disease-like MM components when grown on the F80/200 fibril nanopattern, which is similar to diseased MCs.

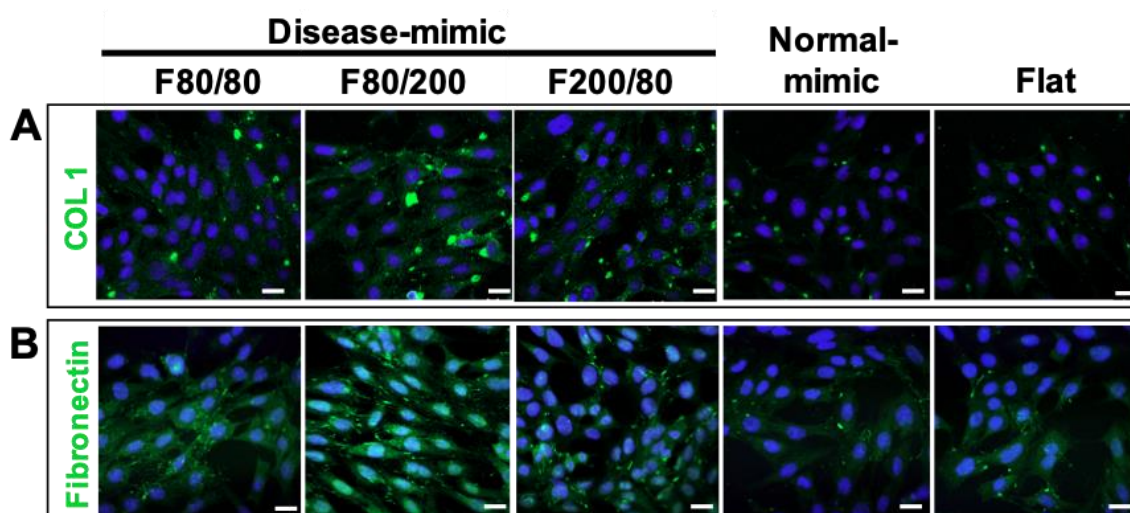


**Figure 3. 6.** Expressions of diseased ECM components in MES13 cells cultured on disease- and normal-mimic nanopatterns. Cells were cultured on various TiO<sub>2</sub> nanopatterns for 48 h and immunostained for the following ECM components: COL1 (A, green) and fibronectin (B, green). The nuclei were stained with 4',6-diamidino-2-phenylindole (DAPI) (blue), and the fluorescence images were taken with a confocal microscope. Scale bar = 20 μm. **Abbreviations:** COL1, type I collagen.

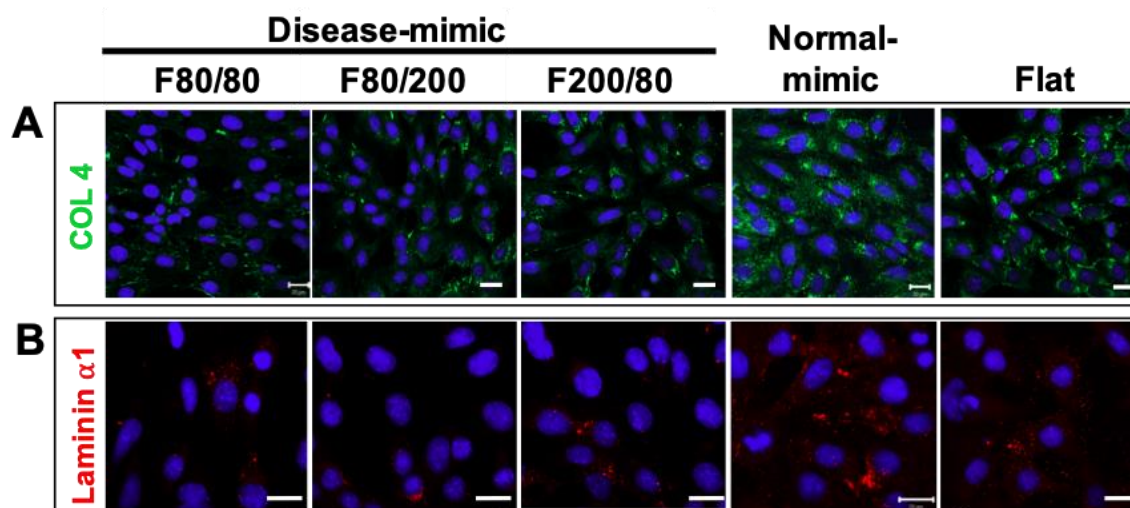


**Figure 3. 7.** Expressions of normal ECM components in MES13 cells cultured on disease- and normal-mimic nanopatterns. Cells were cultured on various TiO<sub>2</sub> nanopatterns for 48 h and immunostained for the following ECM components: COL4 (A, green) and laminin α1 (B, red). The nuclei were stained with 4',6-diamidino-2-phenylindole (DAPI) (blue), and the fluorescence images were taken with a confocal microscope. Scale bar = 20 μm. **Abbreviations:** COL4, type IV collagen.

### 3.3.4. MES13 Cell Morphological and Cytoskeletal Changes

The altered morphology of MCs may affect cell functions such as cell adhesion, proliferation and MM component secretion [4,9,37]. To investigate the influence of nanotopographical features on MES13 cell morphology and cytoskeletal changes after 24 h of seeding on TiO<sub>2</sub> nanopatterns, a qualitative assessment of the morphology was performed using SEM, and results showed cell attachment and spreading on all nanopatterns (Figure 3.8). MES13 cells exhibited a fusiform and elongated morphology, which is characteristic of activated myofibroblasts, when grown on the F80/200 nanopattern (Figure 3.8B), revealing that cells orient along the direction of the nanopattern 80 nm wide and 200 nm apart. However, cells did display a multipolar and stellate morphology on the F80/80, F200/80, normal-mimic and flat control nanopatterns (Figures 3.8A, C–E).

In immunofluorescent images, actin stress fibers and vinculin can be observed on MES13 cells growing on TiO<sub>2</sub> nanopatterns. The staining of F-actin filaments by rhodamine-conjugated phalloidin revealed a cytoskeletal arrangement that corresponds to the cell morphology stretched along the long axis of the cells. Cells grown on the F80/200 nanopattern showed an elongated morphology consistent with SEM images, and were mostly parallel to one another (Figure 3.8G). In addition, fewer stress fibers were observed in cells grown on the flat control (Figure 3.8J) compared to the other nanopatterns (Figures 3.8F–I).

The actin-binding protein vinculin has been reported to associate with the actin cytoskeleton via focal adhesion (FA) [38]. Vinculin immunostaining was performed to further characterize cell morphology during growth on various nanopatterns. The results showed that cells grown on the F80/80, F80/200 and F200/80 nanopatterns (Figures 3.8K–

M) had diffused vinculin staining in the cytosol, whereas clear FA spots were distributed throughout the cell bodies. However, slightly diffused vinculin staining in the cytosol and smaller FA spots appeared in cells grown on the F80/200 nanopattern (Figure 3.8L). Less vinculin diffusion was detected in cells on the normal-mimic nanopattern, with clear FA spots distributed both at the cell periphery and throughout the cell bodies (Figure 3.8N). Cells grown on the flat control displayed diffused vinculin staining in the cytosol, and FA spots were distributed only at the cell periphery (Figure 3.8O). Diffused localization of vinculin is indicative of limited FA maturation in cells. These findings revealed that the F80/200 nanopattern reduced FA maturation, whereas the normal-mimic nanopattern promoted cells to form mature FAs. These findings indicated that the disease-mimic F80/200 nanopattern affected cellular morphology and focal adhesion.

### **3.3.5. $\alpha$ -SMA Expression in MES13 Cells**

$\alpha$ -SMA has been identified as a marker of MC activation that is expressed during glomerular injury [10,39]. To determine whether the disease-mimic nanopatterns influenced MES13 cell activation,  $\alpha$ -SMA expression and localization were performed by immunofluorescence staining. The results showed that the cells had a higher expression of  $\alpha$ -SMA when grown on the F80/200 nanopattern than when grown on the other nanopatterns (Figure 3.9). In addition,  $\alpha$ -SMA is localized to the cytoplasm in cells (indicated by arrow) grown on the F80/200 nanopattern. Large  $\alpha$ -SMA localization to the nuclei of cells grown on F200/80, the normal-mimic and the flat control nanopattern, revealed that the F80/200 nanopattern induced MES13 cell activation similar to the diseased condition.

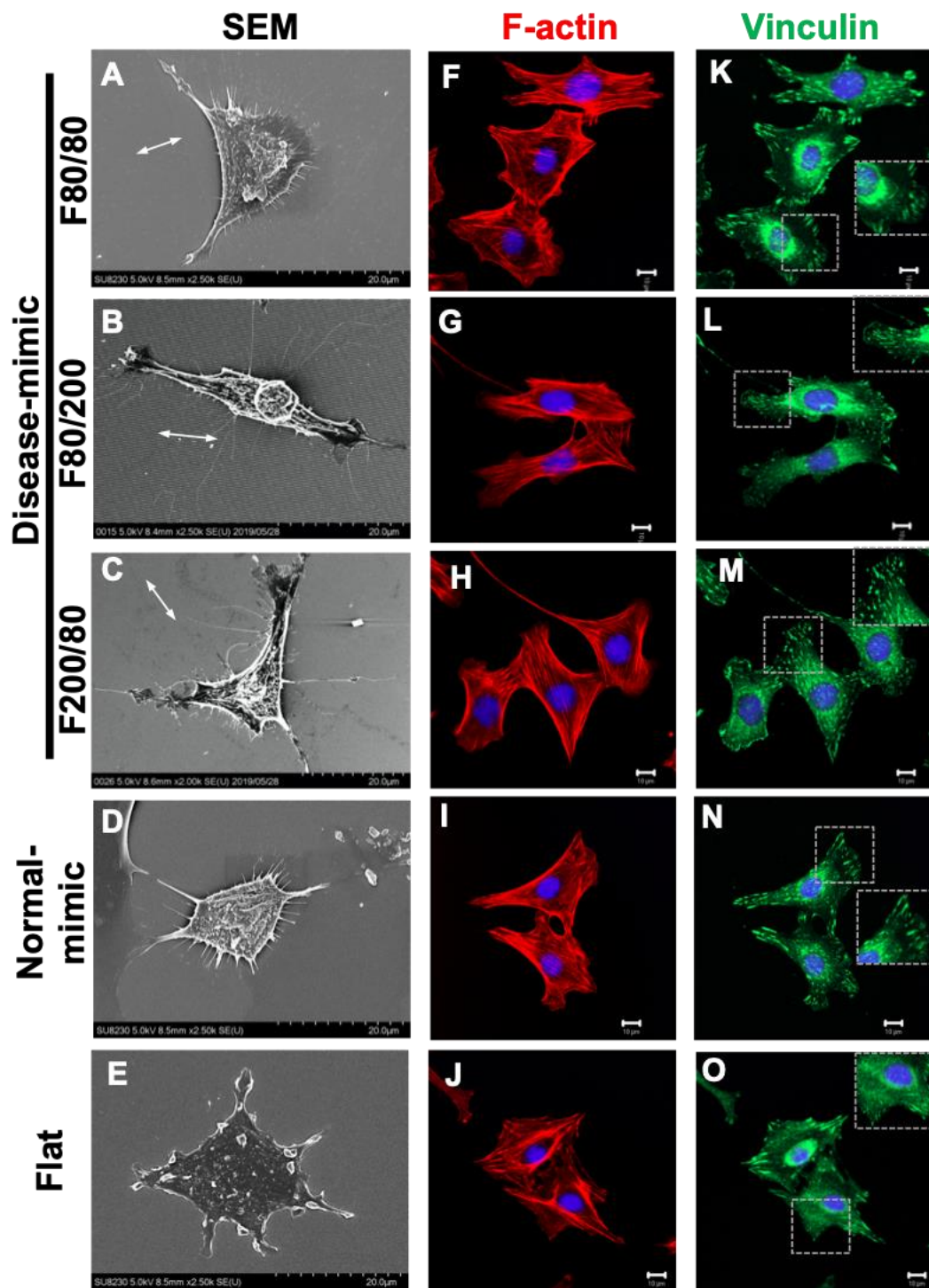


**Figure 3. 8.** MES13 cell morphological and cytoskeletal changes in disease- and normal-mimic nanopatterns. Cells were adhered to various TiO<sub>2</sub> nanopatterns for 24 h, and cellular morphology was observed by SEM micrographs (A–E). Confocal microscopy images show the actin cytoskeleton (F–J, red), the cytoskeletal protein vinculin (K–O, green) and nuclei (blue) in cells after culturing on TiO<sub>2</sub> nanopatterns for 24 h. The inlay highlights the focal adhesion spots. Scale bar = 20 μm (A–E) or 10 μm (F–O). The white arrow indicates the direction of the nano-gratings.

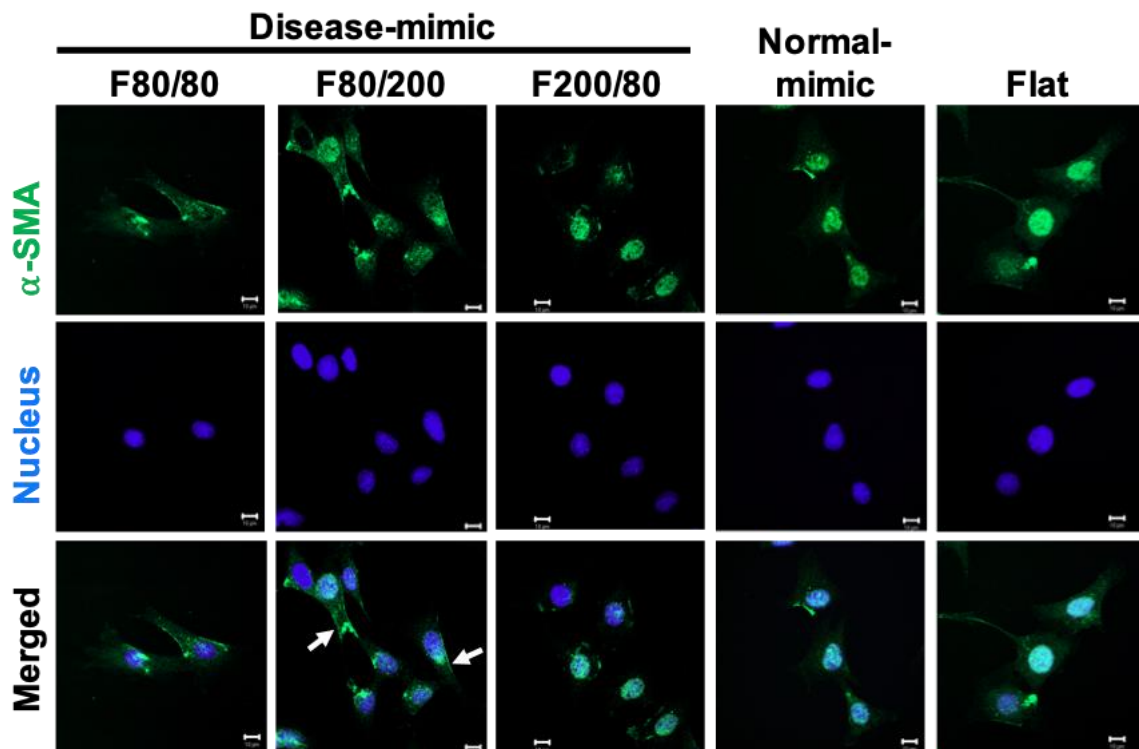


**Figure 3. 9.** Alpha-smooth muscle actin ( $\alpha$ -SMA) expression in MES13 cells influenced by disease- and normal-mimic nanopatterns. Confocal microscopy images show  $\alpha$ -SMA (green) and nuclei (blue) in cells after culturing on TiO<sub>2</sub> nanopatterns for 24 h. Scale bar = 10  $\mu$ m. **Abbreviation:**  $\alpha$ -SMA, alpha-smooth muscle actin.

### 3.3.6. TGF- $\beta$ 1 Expression in MES13 Cells

TGF- $\beta$ 1 is a key mediator in the progression of renal fibrosis [20]. It has been demonstrated that TGF- $\beta$ 1 stimulates  $\alpha$ -SMA expression in MCs during the progression of the disease [12,41]. Thus, to further examine whether TGF- $\beta$ 1 is involved in the influence of the disease-mimic nanopattern on ECM components and  $\alpha$ -SMA expression, TGF- $\beta$ 1 expression and localization were determined by immunofluorescence staining. As a result, higher TGF- $\beta$ 1 expression was detected along the cell leading edge when grown on the F80/200 nanopattern compared to the other nanopatterns (Figure 3.10), revealing

that the F80/200 nanopattern-induced ECM component and  $\alpha$ -SMA expression changes could be mediated by TGF- $\beta$ 1.

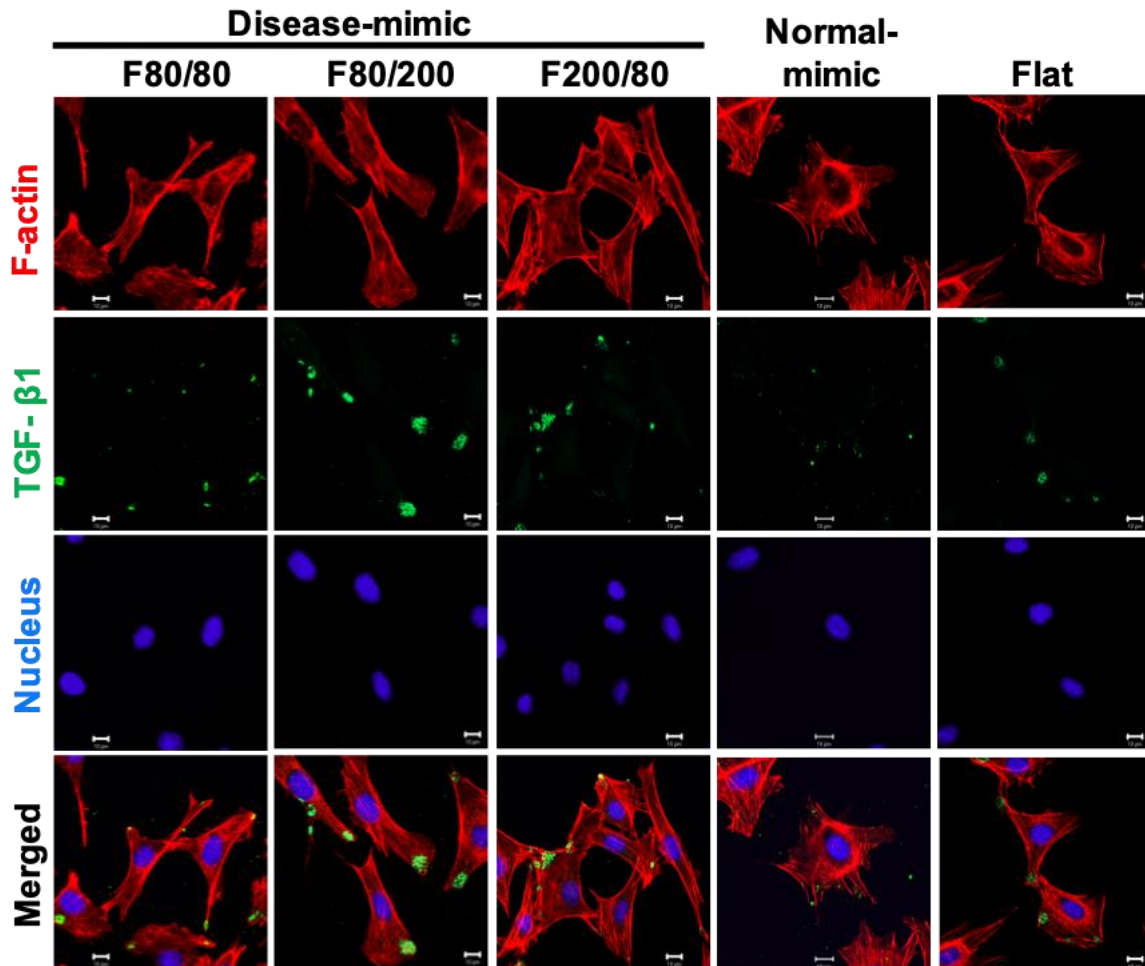


**Figure 3. 10.** Transforming growth factor beta 1 (TGF- $\beta$ 1) expression in MES13 cells influenced by disease- and normal-mimic nanopatterns. Confocal microscopy images show TGF- $\beta$ 1 (green), actin cytoskeleton (red), and nuclei (blue) in cells after culturing on TiO<sub>2</sub> nanopatterns for 24h. Scale bar =10 $\mu$ m. **Abbreviation:** TGF- $\beta$ 1, transforming growth factor beta 1.

### 3.3.7. Integrin $\alpha 5\beta 1$ Expression in MES13 Cells

Integrin  $\alpha 5\beta 1$  is a crucial molecule in mediating human mesangial cell adhesion to fibronectin [42]. To assess the correlation of fibronectin matrix production in MES13 cells when grown on various nano-topographical scaffolds, the expression of integrin  $\alpha 5\beta 1$  was determined by immunofluorescence staining. The results showed an obvious expression of integrin  $\alpha 5\beta 1$  in cells (indicated by arrow) grown on the F80/200 nanopattern compared to the other nanopatterns (Figure 3.11), revealing that F80/200-nanopatterned topography-induced fibronectin accumulation could be mediated by integrin  $\alpha 5\beta 1$ .

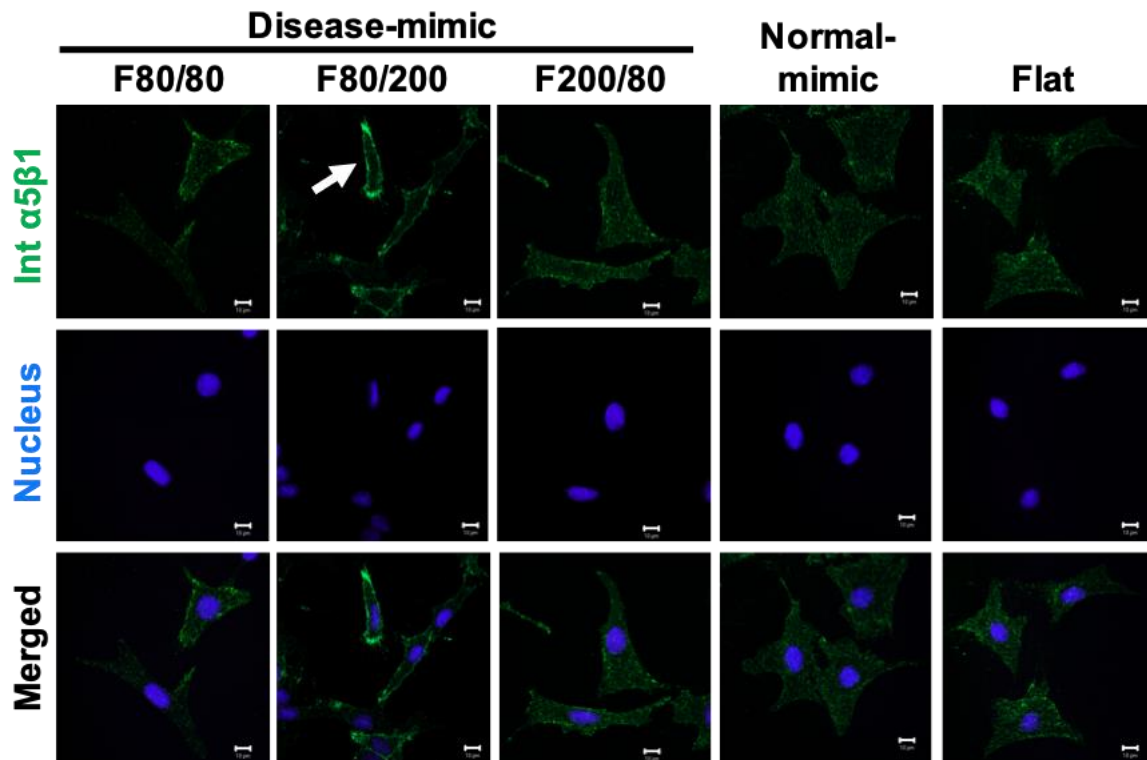


**Figure 3. 11.** Integrin  $\alpha 5\beta 1$  expression in MES13 cells influenced by disease- and normal-mimic nanopatterns. Confocal microscopy images show integrin  $\alpha 5\beta 1$  (Int  $\alpha 5\beta 1$ , green) and nuclei (blue) in cells after culturing on TiO<sub>2</sub> nanopatterns for 24 h. Scale bar =10  $\mu$ m. **Abbreviation:** Int  $\alpha 5\beta 1$ , integrin  $\alpha 5\beta 1$ .

### 3.4. Discussion

In this chapter, TiO<sub>2</sub>-based nanopatterns with specific sizes of topographic ridges and grooves that mimic the diseased native MM 3D structure that influences MES13 cell functions, including cell proliferation, ECM components and morphological changes, were investigated.

To better mimic the *in vivo* native nanostructure, nano-fabrication techniques such as EBL can create the patterns at the nanoscale [28,29]. However, there are still some challenges with the throughput of electron beam projection systems, which are severely limited by the available optical field size and can only pattern relatively small areas with a long writing time. EB irradiation-induced defects also need to be considered. Thus, to overcome these challenges, approximately 80 nm was the minimum dimension used in this study to closely mimic the native collagen scaffold of MM. In this study, highly uniform and well-defined nanostructures with 80 to 200 nm lateral dimensions and various geometries without obvious defects were fabricated. A substrate with dimensions smaller than 80 nm is difficult to achieve due to the EBL and ALD limitations.

Five different TiO<sub>2</sub>-based nanopatterns, disease-mimic nanopatterns F80/80, F80/200 and F200/80, a normal-mimic and an unpatterned flat control, were fabricated to test the hypothesis in this study that disease-mimic nano-topographical features influence MC function by controlling cell morphology. The nanopatterns with different ridges/grooves were designed to mimic COL1 fiber-forming structures in diseased MM. One normal-mimic nanopattern with pores approximately 50 nm in diameter, 80 nm spacing, and 80 nm in depth was also created to mimic the COL4 network-forming structure in normal MM.

In mammals, the diameter of collagen fibers, bundles of closely packed collagen fibrils, depends on the tissue and stage of development [43]. It has been found that COL1 fibers are located in parallel with one another, and are about 77 nm in diameter in the MM of diabetic nephropathy patients [44,45]. Moreover, a previous clinical study indicated that a significantly loosened, enlarged meshwork structure is detected in nephropathy MM [45]. These reports are consistent with my finding that the disease-mimic nanopattern F80/200, which is 80 nm wide with enlarged spacing (200 nm), closely mimics the diseased MM structure. MC proliferation and ECM accumulation are the major features in a variety of glomerular diseases [1,2,5,46]. The results of this chapter showed that cultured MES13 cells grown on the F80/200 nanopattern had higher proliferation, decreased normal MM components (COL4 and laminin  $\alpha$ 1) and secreted excessive abnormal ECM components (COL1 and fibronectin). On the other hand, cells grown on the normal-mimic nanopattern exhibited normal MC functions, such as low proliferation, and produced normal MM components (Figures 3.2, 3.4 and 3.5). In fact, COL1 is absent in glomeruli under normal conditions, and excessive COL1 deposition is usually found in the early stage of renal fibrosis [47]. In addition, the accumulation of COL1 and fibronectin in mesangium by proliferating MCs is the direct result of mesangial expansion in many *in vivo* models and types of glomerular disease [2,18,48–50]. Laminin  $\alpha$ 1 is an essential ECM component in MM and plays a critical role in mesangial homeostasis by regulating the MC population and MM deposition through TGF- $\beta$ /Smad signaling [15]. Downregulated laminin  $\alpha$ 1 in MM has been shown to affect MC function and result in mesangium expansion [50]. Increased TGF- $\beta$ 1-mediated fibronectin accumulation in MM is also involved in several renal diseases [51].

MM components can cause MC morphology alterations and differentiation, as well as affect the MC secretion of ECM [9]. MCs maintain the structural integrity of the glomerular microvascular to regulate blood flow by their contractile cytoskeleton, which is formed by F-actin-containing stress fibers [52]. F-actin forms FA protein complexes at stress fiber ends and co-localizes with the actin-binding protein vinculin [38]. The results of this chapter demonstrated that MES13 cells grown on the F80/200 nanopattern showed elongated and fusiform morphologies with diffused vinculin, which was slightly different from those grown on other nanopatterns, indicating that the F80/200 nanopattern influenced MC activation, but had less effect on FA maturation [53]. Compared with the normal-mimic, F80/80 and F200/80 nanopatterns showed cells that were stellate in shape with abundant F-actin stress fibers with vinculin, suggesting that cells were more developed on these nanopatterned topographies than on the flat control. These findings suggested that the disease-mimic nanopattern (F80/200) influence on cell proliferation and altered MM components might be related to the change in cell morphology.

Although the phenomenon of cellular responses to nano-topography has been known for decades [29,34,54], the underlying mechanism remains poorly understood. One possible mechanism is that cells sense nano-topography of ECM by integrin molecules, and trigger integrins assemble to form integrin clusters, following signal processes such as a clustered adhesion complex formation and also linking the cell cytoskeleton to ECM, and then trigger ECM remodeling that modulate cell morphology [31,55,56]. Hence, nanopatterns with different ridges, grooves and pores could influence cellular integrin clusters formation. Figure 3.12 illustrated the possible mechanisms that cells sense nanopattern substrates.

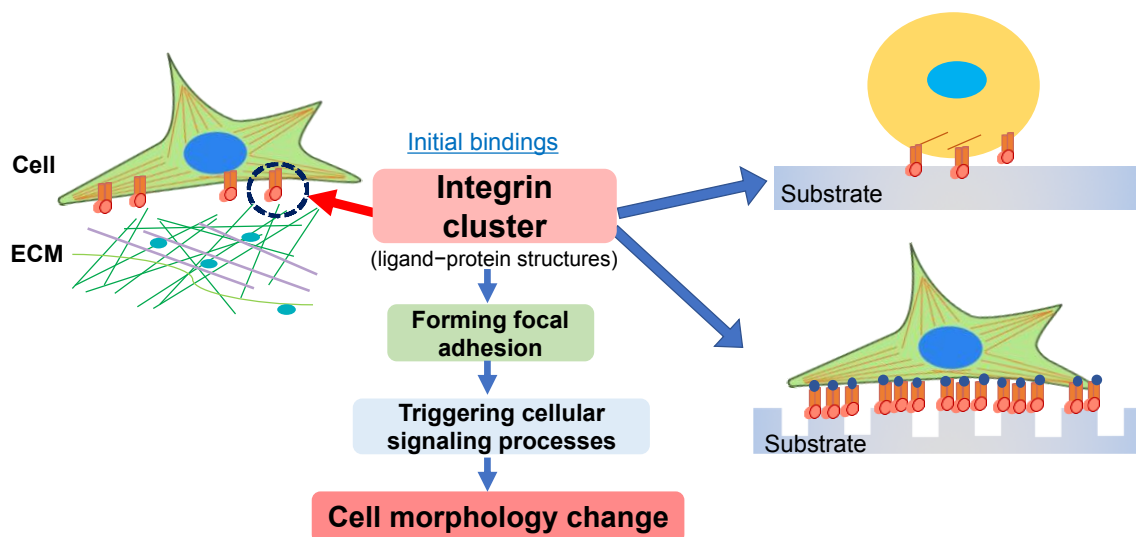


**Figure 3. 12.** The possible mechanism of cells sense nanopatterned substrates through the integrins assembly and integrin clusters formation.

To further clarify the possible mechanism of MES13 changes in cell behavior when cultured on various nano-topographies, the expressions of three proteins,  $\alpha$ -SMA, TGF- $\beta$ 1 and integrin  $\alpha$ 5 $\beta$ 1 were evaluated. The  $\alpha$ -SMA expressed in mesangium region is associated with the mesangial cell proliferation and represents a marker of cell activation [13]. MCs express  $\alpha$ -SMA, during proliferation and repair processes after severe injury [10–12]. However,  $\alpha$ -SMA is absent in normal MCs [10,39].  $\alpha$ -SMA is also known as a marker of MC myofibroblast activation and differentiation in glomerular disease, and is mediated by TGF- $\beta$ 1, a key mediator in the progression of renal fibrosis [40,57,58]. Moreover, TGF- $\beta$ 1 has been demonstrated to induce  $\alpha$ -SMA expression by upregulating the fibronectin receptor, integrin  $\alpha$ 5 $\beta$ 1, in human MCs during renal fibrosis *in vivo* and *in vitro* [42,59,60]. Increased expression of TGF- $\beta$ 1 by MCs has also been demonstrated when MCs are cultured on COL1 gels [19]. In this chapter, the F80/200 nanopattern induced higher  $\alpha$ -SMA, TGF- $\beta$ 1, and integrin  $\alpha$ 5 $\beta$ 1 expressions in MES13 cells, which is

similar to MCs under disease status, revealing that increased COL1 and fibronectin might be modulated by TGF- $\beta$ 1 produced by activated MCs.

MCs also act to regulate the glomerular filtration rate (GFR) by modulating the capillaries' surface area [1]. Injured MCs could trigger TGF- $\beta$ 1 release, and this then results in ECM accumulation in mesangium and tubular damage, and finally contributes to renal insufficiency [61]. As a limitation of this study, the exact molecular pathway correlating with inflammatory effect and ECM accumulation in disease-like MCs induced by the disease-mimic nanopattern has not been identified yet. However, additional experiments to further validate this speculation need to be conducted.

### **3.5. Conclusions**

The results in this chapter showed that disease-mimic nano-topographies influence MES13 cell functions, including changes in cell proliferation and altered MM components. A disease-mimic nanopattern with 80 nm depth, 80 nm ridges and enlarged grooves (200 nm apart) guided cells to adopt disease-like behaviors, including increased proliferation, excessive abnormal MM component production, decreased normal MM component production and changed cell morphologies. These phenomena are consistent with the glomerular structural change in the DSS-induced colitis mouse model I established previously. These findings could be important to further establish a disease-mimic culture system for elucidating the molecular mechanisms underlying glomerular disease, and also important for a drug screening platform.

## References

1. Scindia, Y.M.; Deshmukh, U.S.; Bagavant, H. Mesangial pathology in glomerular disease: targets for therapeutic intervention. *Adv Drug Deliv Rev* **2010**, *62* (14), 1337-43.
2. Chang, C.J.; Wang, P.C.; Huang, T.C.; Taniguchi, A. Change in Renal Glomerular Collagens and Glomerular Filtration Barrier-Related Proteins in a Dextran Sulfate Sodium-Induced Colitis Mouse Model. *Int J Mol Sci* **2019**, *20* (6).
3. Zylka, A.; Dumnicka, P.; Kusnierz-Cabala, B.; Gala-Bladzinska, A.; Ceranowicz, P.; Kucharz, J.; Zabek-Adamska, A.; Maziarz, B.; Drozd, R.; Kuzniewski, M. Markers of Glomerular and Tubular Damage in the Early Stage of Kidney Disease in Type 2 Diabetic Patients. *Mediators Inflamm* **2018**, *2018*, 7659243.
4. Giehl, K.; Graness, A.; Goppelt-Struebe, M. The small GTPase Rac-1 is a regulator of mesangial cell morphology and thrombospondin-1 expression. *Am J Physiol Renal Physiol* **2008**, *294* (2), F407-13.
5. Schlondorff, D.; Banas, B. The mesangial cell revisited: no cell is an island. *J Am Soc Nephrol* **2009**, *20* (6), 1179-87.
6. Guo, L.; Luo, S.; Du, Z.; Zhou, M.; Li, P.; Fu, Y.; Sun, X.; Huang, Y.; Zhang, Z. Targeted delivery of celastrol to mesangial cells is effective against mesangioproliferative glomerulonephritis. *Nat Commun* **2017**, *8* (1), 878.
7. Kreisberg, J. I.; Karnovsky, M. J. Glomerular cells in culture. *Kidney Int* **1983**, *23* (3), 439-47.
8. Davies, M. The mesangial cell: a tissue culture view. *Kidney Int* **1994**, *45* (2), 320-7.
9. Kashgarian, M.; Sterzel, R.B. The pathobiology of the mesangium. *Kidney Int* **1992**, *41* (3), 524-9.

10. Dubus, I.; L'Azou, B.; Gordien, M.; Delmas, Y.; Labouyrie, J.P.; Bonnet, J.; Combe, C. Cytoskeletal reorganization by mycophenolic acid alters mesangial cell migration and contractility. *Hypertension* **2003**, *42* (5), 956-61.
11. Sakai, T.; Kriz, W. The structural relationship between mesangial cells and basement membrane of the renal glomerulus. *Anat Embryol (Berl)* **1987**, *176* (3), 373-86.
12. Stephenson, L.A.; Haney, L.B.; Hussaini, I.M.; Karns, L.R.; Glass, W.F. 2nd, Regulation of smooth muscle alpha-actin expression and hypertrophy in cultured mesangial cells. *Kidney Int* **1998**, *54* (4), 1175-87.
13. Lopez-Novoa, J.M.; Rodriguez-Pena, A.B.; Ortiz, A.; Martinez-Salgado, C.; Lopez Hernandez, F.J. Etiopathology of chronic tubular, glomerular and renovascular nephropathies: clinical implications. *J Transl Med* **2011**, *9*, 13.
14. Schena, F.P.; Gesualdo, L.; Grandaliano, G.; Montinaro, V. Progression of renal damage in human glomerulonephritides: is there sleight of hand in winning the game? *Kidney Int* **1997**, *52* (6), 1439-57.
15. Kurihara, H.; Sakai, T. Cell biology of mesangial cells: the third cell that maintains the glomerular capillary. *Anat Sci Int* **2017**, *92* (2), 173-186.
16. Kitamura, M.; Mitarai, T.; Maruyama, N.; Nagasawa, R.; Yoshida, H.; Sakai, O. Mesangial cell behavior in a three-dimensional extracellular matrix. *Kidney Int* **1991**, *40* (4), 653-61.
17. Alexakis, C.; Maxwell, P.; Bou-Gharios, G. Organ-specific collagen expression: implications for renal disease. *Nephron Exp Nephrol* **2006**, *102* (3-4), e71-5.
18. Glick, A.D.; Jacobson, H.R.; Haralson, M.A. Mesangial deposition of type I collagen in human glomerulosclerosis. *Hum Pathol* **1992**, *23* (12), 1373-9.
19. Ortega-Velazquez, R.; Gonzalez-Rubio, M.; Ruiz-Torres, M.P.; Diez-Marques, M.L.; Iglesias, M.C.; Rodriguez-Puyol, M.; Rodriguez-Puyol, D. Collagen I upregulates extracellular matrix gene expression and secretion of TGF-beta 1 by cultured human mesangial cells. *Am J Physiol Cell Physiol* **2004**, *286* (6), C1335-43.

20. Ruef, C.; Kashgarian, M.; Coleman, D.L. Mesangial cell-matrix interactions. Effects on mesangial cell growth and cytokine secretion. *Am J Pathol* **1992**, *141* (2), 429-39.
21. Knupp, C.; Squire, J. M. Molecular packing in network-forming collagens. *Adv Protein Chem* **2005**, *70*, 375-403.
22. Schocklmann, H.O.; Lang, S.; Sterzel, R.B. Regulation of mesangial cell proliferation. *Kidney Int* **1999**, *56* (4), 1199-207.
23. Yang, Y.; Wang, K.; Gu, X.; Leong, K. W. Biophysical Regulation of Cell Behavior- Cross Talk between Substrate Stiffness and Nanotopography. *Engineering (Beijing)* **2017**, *3* (1), 36-54.
24. Kim, D.H.; Provenzano, P.P.; Smith, C.L.; Levchenko, A. Matrix nanotopography as a regulator of cell function. *J Cell Biol* **2012**, *197* (3), 351-60.
25. Dong, J.; Wei, H.; Han, M.; Guan, Y.; Wu, Y.; Li, H. Collagen type III glomerulopathy: A case report and review of 20 cases. *Exp Ther Med* **2015**, *10* (4), 1445-1449.
26. Hironaka, K.; Makino, H.; Yamasaki, Y.; Ota, Z. Renal basement membranes by ultrahigh resolution scanning electron microscopy. *Kidney Int* **1993**, *43* (2), 334-45.
27. Erisken, C.; Zhang, X.; Moffat, K.L.; Levine, W. N.; Lu, H.H. Scaffold fiber diameter regulates human tendon fibroblast growth and differentiation. *Tissue Eng Part A* **2013**, *19* (3-4), 519-28.
28. Bae, H.; Chu, H.; Edalat, F.; Cha, J.M.; Sant, S.; Kashyap, A.; Ahari, A.F.; Kwon, C. H.; Nichol, J.W.; Manoucheri, S.; Zamanian, B.; Wang, Y.; Khademhosseini, A. Development of functional biomaterials with micro- and nanoscale technologies for tissue engineering and drug delivery applications. *J Tissue Eng Regen Med* **2014**, *8* (1), 1-14.
29. Ermis, M.; Antmen, E.; Hasirci, V. Micro and Nanofabrication methods to control cell-substrate interactions and cell behavior: A review from the tissue engineering perspective. *Bioact Mater* **2018**, *3* (3), 355-369.

30. von der Mark, K.; Park, J.; Bauer, S.; Schmuki, P. Nanoscale engineering of biomimetic surfaces: cues from the extracellular matrix. *Cell Tissue Res* **2010**, *339* (1), 131-53.
31. Ozguldez, H.O.; Cha, J.; Hong, Y.; Koh, I.; Kim, P. Nanoengineered, cell-derived extracellular matrix influences ECM-related gene expression of mesenchymal stem cells. *Biomater Res* **2018**, *22*, 32.
32. Abdellatef, S.A.; Ohi, A.; Nabatame, T.; Taniguchi, A. Induction of hepatocyte functional protein expression by submicron/nano-patterning substrates to mimic in vivo structures. *Biomaterials Science* **2014**, *2* (3), 330-338.
33. Abdellatef, S.A.; Ohi, A.; Nabatame, T.; Taniguchi, A. The Effect of Physical and Chemical Cues on Hepatocellular Function and Morphology. *International Journal of Molecular Sciences* **2014**, *15* (3), 4299-4317.
34. Abdellatef, S.A.; Tange, R.; Sato, T.; Ohi, A.; Nabatame, T.; Taniguchi, A. Nanostructures Control the Hepatocellular Responses to a Cytotoxic Agent "Cisplatin". *Biomed Res Int* **2015**, *2015*, 925319.
35. Kim, D.; Li, H.Y.; Lee, J.H.; Oh, Y.S.; Jun, H.S. Lysophosphatidic acid increases mesangial cell proliferation in models of diabetic nephropathy via Rac1/MAPK/KLF5 signaling. *Exp Mol Med* **2019**, *51* (2), 18.
36. Ishimura, E.; Sterzel, R.B.; Morii, H.; Kashgarian, M. Extracellular matrix protein: gene expression and synthesis in cultured rat mesangial cells. *Nihon Jinzo Gakkai Shi* **1992**, *34* (1), 9-17.
37. Bussolati, B.; Mariano, F.; Biancone, L.; Foa, R.; David, S.; Cambi, V.; Camussi, G. Interleukin-12 is synthesized by mesangial cells and stimulates platelet-activating factor synthesis, cytoskeletal reorganization, and cell shape change. *Am J Pathol* **1999**, *154* (2), 623-32.
38. Thwaites, T.R.; Pedrosa, A.T.; Peacock, T.P.; Carabeo, R.A. Vinculin Interacts with the Chlamydia Effector TarP Via a Tripartite Vinculin Binding Domain to Mediate Actin Recruitment and Assembly at the Plasma Membrane. *Front Cell Infect Microbiol* **2015**, *5*, 88.
-

39. Xie, X.; Xia, W.; Fei, X.; Xu, Q.; Yang, X.; Qiu, D.; Wang, M. Relaxin Inhibits High Glucose-Induced Matrix Accumulation in Human Mesangial Cells by Interfering with TGF-beta1 Production and Mesangial Cells Phenotypic Transition. *Biol Pharm Bull* **2015**, *38* (10), 1464-9.
40. Iwano, M.; Akai, Y.; Fujii, Y.; Dohi, Y.; Matsumura, N.; Dohi, K. Intraglomerular expression of transforming growth factor-beta 1 (TGF-beta 1) mRNA in patients with glomerulonephritis: quantitative analysis by competitive polymerase chain reaction. *Clin Exp Immunol* **1994**, *97* (2), 309-14.
41. O'Connor, J.W.; Mistry, K.; Detweiler, D.; Wang, C.; Gomez, E.W. Cell-cell contact and matrix adhesion promote alphaSMA expression during TGFbeta1-induced epithelial-myofibroblast transition via Notch and MRTF-A. *Sci Rep* **2016**, *6*, 26226.
42. Adler, S.; Brady, H.R. Cell adhesion molecules and the glomerulopathies. *Am J Med* **1999**, *107* (4), 371-86.
43. Canty, E.G.; Starborg, T.; Lu, Y.; Humphries, S.M.; Holmes, D.F.; Meadows, R.S.; Huffman, A.; O'Toole, E.T.; Kadler, K.E. Actin filaments are required for fibripositor-mediated collagen fibril alignment in tendon. *J Biol Chem* **2006**, *281* (50), 38592-8.
44. Makino, H.; Shikata, K.; Hironaka, K.; Kushiro, M.; Yamasaki, Y.; Sugimoto, H.; Ota, Z.; Araki, N.; Horiuchi, S. Ultrastructure of nonenzymatically glycosylated mesangial matrix in diabetic nephropathy. *Kidney Int* **1995**, *48* (2), 517-26.
45. Herrera, G.A.; Turbat-Herrera, E.A. Renal diseases with organized deposits: an algorithmic approach to classification and clinicopathologic diagnosis. *Arch Pathol Lab Med* **2010**, *134* (4), 512-31.
46. Cove-Smith, A.; Hendry, B.M. The regulation of mesangial cell proliferation. *Nephron Exp Nephrol* **2008**, *108* (4), e74-9.
47. Genovese, F.; Manresa, A.A.; Leeming, D.J.; Karsdal, M.A.; Boor, P. The extracellular matrix in the kidney: a source of novel non-invasive biomarkers of kidney fibrosis? *Fibrogenesis Tissue Repair* **2014**, *7* (1), 4.
-

48. Hubchak, S.C.; Sparks, E.E.; Hayashida, T.; Schnaper, H.W. Rac1 promotes TGF-beta-stimulated mesangial cell type I collagen expression through a PI3K/Akt-dependent mechanism. *Am J Physiol Renal Physiol* **2009**, *297* (5), F1316-23.
49. Brodeur, A.C.; Roberts-Pilgrim, A.M.; Thompson, K.L.; Franklin, C.L.; Phillips, C.L. Transforming growth factor-beta1/Smad3-independent epithelial-mesenchymal transition in type I collagen glomerulopathy. *Int J Nephrol Renovasc Dis* **2017**, *10*, 251-259.
50. Ning, L.; Kurihara, H.; de Vega, S.; Ichikawa-Tomikawa, N.; Xu, Z.; Nonaka, R.; Kazuno, S.; Yamada, Y.; Miner, J.H.; Arikawa-Hirasawa, E. Laminin alpha1 regulates age-related mesangial cell proliferation and mesangial matrix accumulation through the TGF-beta pathway. *Am J Pathol* **2014**, *184* (6), 1683-94.
51. Hu, C.; Sun, L.; Xiao, L.; Han, Y.; Fu, X.; Xiong, X.; Xu, X.; Liu, Y.; Yang, S.; Liu, F.; Kanwar, Y.S. Insights into the Mechanisms Involved in the Expression and Regulation of Extracellular Matrix Proteins in Diabetic Nephropathy. *Curr Med Chem* **2015**, *22* (24), 2858-70.
52. Cortes, P.; Mendez, M.; Riser, B.L.; Guerin, C.J.; Rodriguez-Barbero, A.; Hassett, C.; Yee, J. F-actin fiber distribution in glomerular cells: structural and functional implications. *Kidney Int* **2000**, *58* (6), 2452-61.
53. Lutz, R.; Pataky, K.; Gadhari, N.; Marelli, M.; Brugger, J.; Chiquet, M. Nano-stenciled RGD-gold patterns that inhibit focal contact maturation induce lamellipodia formation in fibroblasts. *PLoS One* **2011**, *6* (9), e25459.
54. Wang, K.; Bruce, A.; Mezan, R.; Kadiyala, A.; Wang, L.; Dawson, J.; Rojanasakul, Y.; Yang, Y. Nanotopographical Modulation of Cell Function through Nuclear Deformation. *ACS Appl Mater Interfaces* **2016**, *8* (8), 5082-92.
55. Ruprecht, V.; Monzo, P.; Ravasio, A.; Yue, Z.; Makhija, E.; Strale, P.O.; Gauthier, N.; Shivashankar, G.V.; Studer, V.; Albiges-Rizo, C.; Viasnoff, V. How cells respond to environmental cues - insights from bio-functionalized substrates. *J Cell Sci* **2017**, *130* (1), 51-61.

56. Kechagia, J.Z.; Ivaska, J.; Roca-Cusachs, P. Integrins as biomechanical sensors of the microenvironment. *Nat Rev Mol Cell Biol* **2019**, *20* (8), 457-473.
57. Hewitson, T.D.; Holt, S.G.; Tan, S.J.; Wigg, B.; Samuel, C.S.; Smith, E.R. Epigenetic Modifications to H3K9 in Renal Tubulointerstitial Cells after Unilateral Ureteric Obstruction and TGF-beta1 Stimulation. *Front Pharmacol* **2017**, *8*, 307.
58. Meran, S.; Steadman, R. Fibroblasts and myofibroblasts in renal fibrosis. *Int J Exp Pathol* **2011**, *92* (3), 158-67.
59. Huang, G.; Brigstock, D.R. Integrin expression and function in the response of primary culture hepatic stellate cells to connective tissue growth factor (CCN2). *J Cell Mol Med* **2011**, *15* (5), 1087-95.
60. Weston, B.S.; Wahab, N.A.; Mason, R.M. CTGF mediates TGF-beta-induced fibronectin matrix deposition by upregulating active alpha5beta1 integrin in human mesangial cells. *J Am Soc Nephrol* **2003**, *14* (3), 601-10.
61. Ghayur, M.N.; Krepinsky, J.C.; Janssen, L.J.; Contractility of the Renal Glomerulus and Mesangial Cells: Lingering Doubts and Strategies for the Future. *Med. Hypotheses Res.* **2008**, *4*, 1-9.

---

## Chapter IV

# Evaluation of Physical and Chemical Cues on Disease-mimic Culture System as a Drug Screening Platform

---

### 4.1. Introduction

Discovery of new drugs is a highly complex and multidisciplinary process [1]. During the initial discovery process, an intensive screening is performed to find a small synthetic molecule or large biomolecule, typically called a drug candidate that will further progress into pre-clinical and clinical development, and ultimately be a marketed medicine [2]. Hence, drug screening is important to obtain the evidence of drug safety, efficacy and mechanism of response on representative biological models [3].

Over the past few decades, most *in vitro* studies have been performed to examine the effects of candidate drug compounds on cell-based culture system on the flat plastic surfaces [4,5]. Mammalian cell cultures provide a wealth of benefits for *in vitro* studies as a platform, to investigate cellular responses to stimulations from biophysical and biochemical cues to disease processes [6-8]. Nevertheless, these culture systems poorly reflect the natural microenvironment and lack the complex environment of the extracellular matrix (ECM) in native tissues, including nano- to micrometer scale structures such as collagen fibrils [9]. In addition, the complex micro/nanoenvironment

---

consists of cell populations and ECM molecules, which forms an intricate system that includes chemical properties such as cytokines and physical properties such as topography, which are critical for cell fate, inducing tissue-specific differentiation, and promoting developmental morphogenesis [10]. Furthermore, numerous animal/cell-based disease models have been developed, and aimed to understand the etiologies of human diseases and treatment strategies [11,12]. Therefore, developing an appropriate disease-mimic model as a screening platform for human diseases is necessary for use in drug discovery. Figure 4.1 illustrated the scheme of the drug screening platform using a disease-mimic model for new drug discovery.

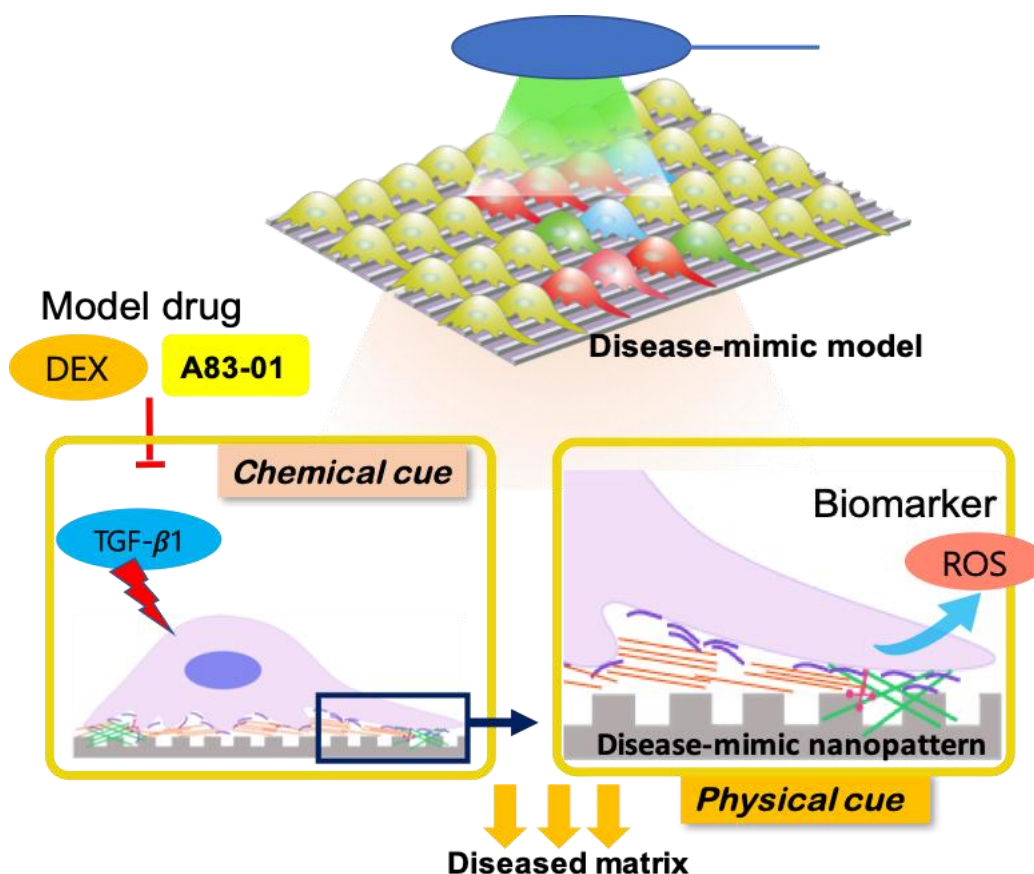


**Figure 4. 1.** Scheme of drug screening platform using a disease-mimic model for new drug discovery. **Abbreviations:** TGF- $\beta$ 1, transforming growth factor-beta 1; DEX, dexamethasone; ROS, reactive oxygen species.

A biomarker is an objectively measured and evaluated indicator of the biological process, pathological process or a cellular response to a therapeutic intervention, to verify that the test is reliable, reproducible and of adequate sensitivity and specificity [13]. Biomarkers thus play a critical role in improving the diagnosis, monitoring drug activity and therapeutic response in drug development process for various diseases [14,15]. These biomarkers need to be detectable, measurable and stable through a variety of methods including physical examination, laboratory assays, and medical imaging [16].

Reactive oxygen species (ROS) are derived from many sources including mitochondria, xanthine oxidase, uncoupled nitric oxide synthases and NADPH oxidase [17]. ROS play an important role in mediating transforming growth factor-beta 1 (TGF- $\beta$ 1) induced ECM induction and pro-fibrotic activity during kidney injury and in the progression of renal diseases [15]. Therefore, the present study used ROS as a biomarker for the disease-mimic model.

The human kidney regulates fluid homeostasis, electrolyte balance, and waste product removal by filtering the blood through glomeruli, the specialized filtration barrier structure within each nephron [18,19]. Blood enters the glomerulus from an afferent arteriole and passes through a fenestrated endothelial capillary bed surrounded by podocytes. Mesangial cells (MCs) are specialized cells of the renal glomerulus and are located in the center of the intercapillary space that sits between the capillary loops. MCs and mesangial matrix (MM) are attributed the important role of controlling blood flow by contracting themselves to regulate the size of the capillary lumen [20].

In my previous study, the TiO<sub>2</sub>-based disease-mimic nanopattern with 80 nm depth, 80 nm ridges and 200 grooves, has been shown to induce MES13 cell proliferation and

diseased MM components such as type I collagen (COL1) [21], which suggests this disease-mimic nanopattern as a physical cue inducing disease-like cell behavior. TGF- $\beta$ 1 has been shown to mediated COL1 synthesis in MES13 cells on disease-mimic nanopattern [21]. Thus, TGF- $\beta$ 1 is also an important factor as a chemical cue in regulating cell fate under disease situation.

This chapter is aimed to evaluate the disease-mimic culture system using physical and chemical cues for establishing the drug screening platform. Development of a new drug screening platform using disease-mimic condition including chemical and physical cues was evaluated by cell proliferation and diseased matrix components synthesis. A83-01, a selective inhibitor of TGF- $\beta$  type I receptor ALK5 kinase, and Glucocorticoids anti-inflammatory drug, dexamethasone (DEX), were used as model drug (positive control). ROS production was evaluated for use as a biomarker in this disease-mimic culture system.

## **4.2. Materials and Methods**

### **4.2.1. Fabrication of Nanopatterned TiO<sub>2</sub> Substrates**

TiO<sub>2</sub> substrates were fabricated as previously described [21]. ZEP-520A positive-tone EBL resist (Nippon Zeon Co. Japan) was spin-coated on cleaned Si (100) substrates diluted in anisole (1:2 ratio) by a spin coater (Mikasa 1H-D7) at 6000 rpm, and then pre-baked at 180 °C for 3 min. Once the sample cooled to room temperature, a water-soluble conductive material called Spacer (Showa Denko Co. Japan) was spin-coated at 2000 rpm to obtain a very thin layer (10–20 nm). Next, the lithography patterns were written on the substrate with an EBL system (Elionix ELS-7500EX, acceleration voltage = 50 kV, electron beam

(EB) amperage = 220 pA). The precise size of the fabricated substrate resulting from each EB was confirmed by SEM (FEG-SEM, Hitachi SU8230, Toronto ON, Canada). The exposed resist film was developed using n-amyl acetate and methyl isobutyl ketone (89%) /isopropyl alcohol (11%) (Wako Co. Japan), then rinsed by H<sub>2</sub>O and dried with nitrogen gas. The substrates were then etched by inductively coupled plasma-reactive ion etching at antenna power 50 W, bias 5W and tetrafluoromethane flue with 6.5 standard cubic centimeter/minute (SCCM), followed by removing the resist film using O<sub>2</sub> plasma, dimethyl acetamide and SPM solution (H<sub>2</sub>SO<sub>4</sub> + H<sub>2</sub>O<sub>2</sub>, 3:1), respectively. The substrates were then coated with a photoresist (AZ-5214E, Germany) which is used as the mask for ALD, subjected to UV irradiation with a photomask, reversal baking at 120 °C, flood exposure to UV, and development by hexamethyl disilazane and 2.38% tetramethyl ammonium hydroxide (Wako Co. Japan) for 1 min, then rinsed with deionized water. Finally, the TiO<sub>2</sub> thin films were deposited on Si substrates using atomic layer deposition (Picosun SUNALE R-150) with 500 Pa of the chamber pressure and at 100 °C. The thickness of the TiO<sub>2</sub> layer was controlled by the number of cycles: 70 cycles gave a thickness of 5 nm. The TiO<sub>2</sub> precursor [tetra(dimethylamino)titanate] was pumped into the chamber, followed by argon gas to remove the undeposited precursor. Next, H<sub>2</sub>O vapor was pumped in to form the inorganic TiO<sub>2</sub> layer from the organic precursor, and then argon gas was pumped in to remove residual H<sub>2</sub>O. Fabricated TiO<sub>2</sub> nanopattern surfaces were characterized by SEM (SU8230, Hitachi) and AFM (Ti950, Hysitron, MN, USA). Further experiments were performed using the fabricated substrates after dry heat sterilization of the substrate at 170 °C for 1 h. A non-patterned flat surface was used as a control.

#### **4.2.2. Cell Culture**

A mouse immortalized mesangial cell line, SV40MES13 (MES13), was purchased from the American Type Culture Collection (Manassas, VA, USA). Cells were cultured in a 3:1 mixture of Dulbecco's modified Eagle's medium (DMEM)/Ham's F12 medium (Nacalai Tesque, Kyoto, Japan) with supplemented 5% fetal bovine serum (FBS) (Corning Life Sciences, NY, USA), 14 mM HEPES (Gibco, MD, USA), 2 mM glutamine (Gibco) and 100 U/mL penicillin/streptomycin (Nacalai Tesque). Cells were incubated in a humidified incubator at 37 °C with 5% CO<sub>2</sub>. All experiments were performed between passages 8 and 9 to minimize the effects of phenotypic variation in continuous culture. Cells were serum-starved with 1% FBS for 24 h or 48 h prior to examination.

#### **4.2.3. Cell Viability Assay**

MES13 cell viability was measured by WST-1 Cell Proliferation Reagent (a salt of 4-[3-(4-iodophenyl)-2-(4-nitrophenyl)-2H-5-tetrazolio]-1,3-benzene disulfonate) according to the manufacturer's protocol. This method is based on the ability of viable cells to metabolize water-soluble tetrazolium salt WST-1 to formazan by mitochondrial dehydrogenases. Briefly, 1×10<sup>5</sup> cells per well were seeded onto 96-well plate (Iwaki Laboratories, Iwaki, Japan) and the plate was preincubated overnight in 5% CO<sub>2</sub> incubator at 37 °C. Following exposure of cells to various concentrations of TGF-β<sub>1</sub> (0–1 μg/mL), TGF-β type I receptor inhibitors, A83-01 (0–100 μM) or glucocorticosteroid drug, dexamethasone (DEX, 0–100 μM) with growth medium containing 1% FBS for 24 or 48 hours. Control (untreated, 0) cells received an equivalent volume of phosphate buffered

saline (PBS, pH 7.4, Sigma-Aldrich, St. Louis, MO, USA). After incubation, the culture medium was first removed from each well of the 96-well plate and replaced with fresh culture medium solution containing 10% WST-1 reagent (Roche Diagnostics GmbH, Germany) was then added per well and incubated in a 37 °C humidified CO<sub>2</sub> incubator for 2 h. For the background control, the same volume per well of growth medium and WST-1 was used. After 2 hours the absorbance was read by a scanning microplate spectrophotometer (Spark 10M; Tecan Japan) under a wavelength of 450 nm and a reference wavelength of 630 nm for the cleavage of the tetrazolium salt WST-1 to formazan. The absorbance values were then used to calculate the cells' viability.

#### **4.2.4. Cell Proliferation Assays**

The proliferation of cells grown on the nanopattern was evaluated by EdU incorporation using an EdU proliferation kit (iFluor 488) (Abcam, Cambridge, UK) and detected according to the manufacturer's instructions. Briefly, cells were seeded on TiO<sub>2</sub> nanopatterns, which mimics the disease or normal MM at a concentration of  $4 \times 10^4$  cells/well with serum-starved medium (1% FBS) and preincubated overnight in 5% CO<sub>2</sub> incubator at 37 °C. Unpatterned flat substrate was used as control. Cells were pretreated with A83-01 or DEX for 1 hour before TGF- $\beta$ 1 stimulation. After treatment with or without TGF- $\beta$ 1 for 24 h, cells were then incubated with 10  $\mu$ M EdU solution for 2 h at 37 °C in 5% CO<sub>2</sub>. Subsequently, the cells were fixed with 4% formaldehyde for 15 min. After rinsing with 3% BSA in PBS, cells were permeated with 0.5% Triton X-100 in PBS, incubated with iFluor 488 azide, and stained with 300 nM 4',6-diamidino-2-phenylindole (DAPI, Abcam) for 30 min. All images were acquired with a Zeiss LSM 510 META

---

confocal microscope system (Carl Zeiss, Jena, Germany). At least 400 nuclei were counted per experiment.

#### 4.2.5. Immunofluorescence Staining and Confocal Imaging

Immunofluorescence staining was performed using a previously described method [21]. Briefly, cells grown on TiO<sub>2</sub> nanopatterns were treated with or without TGF- $\beta$ 1 for 24 or 48 h. Cells were pretreated with A83-01 or DEX for 1 hour before TGF- $\beta$ 1 stimulation. And then washed three times with PBS. Cells were fixed in 4% formaldehyde at room temperature for 20 min, permeabilized by 0.05% saponin (Sigma-Aldrich) in Tris-buffered saline (TBS, 50 mM Trizma, 150 mM NaCl, pH 7.6) for 15 min, then blocked by 3% BSA (Sigma, USA) in TBS for 1 h at room temperature. Then cells were sequentially incubated with primary antibodies against type I collagen (COL1) and type IV collagen (COL4) (Abcam), respectively, at 4 °C overnight followed by incubation with secondary antibodies conjugated to Alexa Fluor® 488 (Invitrogen, Carlsbad, CA, USA). Nuclei were stained with DAPI and double-stained with rhodamine-conjugated phalloidin (Life Technologies, Gaithersburg, MD, USA) for F-actin filaments. All images were acquired with a Zeiss LSM 510 META confocal microscope system. The antibodies used in this study were listed in Table 4.2.

**Table 4. 1.** List of antibodies used in immunofluorescence staining.

<b>Primary antibodies used</b>	<b>Source</b>	<b>Host</b>
Type I collagen (COL1)	Abcam (ab34710)	Rabbit
Type IV collagen (COL4)	Abcam (ab6586)	Rabbit
<b>Secondary antibodies used</b>	<b>Source</b>	<b>Host</b>
Anti-Rabbit IgG Alexa Fluor 488	Invitrogen (A11008)	Goat

#### 4.2.6. Evaluation of ROS Content in MES13 Cells

The level of ROS in MES13 cells were determined using CellROX® Green reagent (Thermo Fisher Scientific, Waltham, MA), according to the manufacturer's instructions onto a 96 well plate reader and confocal fluorescence microscopy. CellROX® is a cell-permeable and non-fluorescent while in the reduced state. Upon oxidation, the reagent binds DNA and exhibits a strong fluorogenic signal that has absorption/emission maxima of 508/525 nm and remains localized to the nucleus and cytoplasm. Briefly, MES13 cells were seeded onto a black 96-well flat bottom plate (Thermo Fisher Scientific Inc. USA) at a concentration of  $1 \times 10^5$  cells per well and allowed to adhere overnight. Following exposure of cells to the presence or absence of 1 ng/ml TGF- $\beta$ 1 with growth medium containing 1% FBS for 1 to 24 hours. Cells were pretreated with A83-01 or DEX for 1 hour before TGF- $\beta$ 1 stimulation. After treatment, CellROX® reagent was added to a final concentration of 5  $\mu$ M with fresh culture medium, and cells were incubated for 30 min at 37 °C. After incubation, cells were then rinsed with Hank's balanced salt solution (HBSS). The fluorescence intensity of CellROX® reagent was measured at excitation/emission maxima at 488/585 nm using a multimode microplate reader (Spark 10M; Tecan Japan)

For microscopy images, cells were incubated with CellROX® reagent after treatment. After incubation, cells were fixed with 4% formaldehyde at room temperature for 20 min and then stained with 1.5  $\mu$ M DAPI to label the nuclei. Confocal imaging of ROS indicator CellROX® was performed on the Zeiss LSM META 510 confocal microscope (Carl Zeiss, Jena, Germany) and with an excitation of 488nm. The laser excitation power and detector gain were kept constant for all measurements.

For image quantitative, expressions of COL1, COL4 and ROS production were shown as mean  $\pm$  SEM by analyzing mean fluorescence intensity (MFI) in three separate experiments using Fiji ImageJ (NIH Image, MD, USA)

#### **4.2.7. Statistical Analysis**

Data analysis was performed using Prism 8 software (GraphPad, CA, USA). All data are expressed as means  $\pm$  standard error of the mean (SEM) from six replicate sample from each group in at least three independent experiments. Statistical analysis was performed using one-way Analysis of Variance (ANOVA) and Tukey's *post hoc* test for multiple comparisons. Differences between variables were considered statistically significant for  $p$ -values  $< 0.05$ .  $p$ -Values are represented as follows: \* $p < 0.05$ , \*\* $p < 0.01$  and \*\*\* $p < 0.001$ .

### **4.3. Results**

#### **4.3.1. Cell Viability in TGF- $\beta$ 1 Treated MES13 Cells**

This chapter is aimed to evaluate the effects of a chemical cue (TGF- $\beta$ 1) and a physical cue (disease-mimic nanopattern) on MES13 cells for establishing a drug screening platform. Experiments on concentration and incubation time were performed from dose response experiments and time course experiments (24 and 48 h) to optimize the appropriate concentration of TGF- $\beta$ 1, A83-01 and DEX for MES13 cell response. First of

all, in order to identify the optimum dosage of TGF- $\beta$ 1, the present study determined the cell viability with and without TGF- $\beta$ 1 treatment by WST-1 cell viability assay. The results showed that the cell viability gradually decreased when TGF- $\beta$ 1 concentration increased from 0.1 ng/ml to 1  $\mu$ g/ml, with the lowest cell viability (64.26 %) at 1  $\mu$ g/ml (Figure 4.2A) after 24 h of treatment. After 48 h of treatment, the cell viability did not change significantly at the concentration of TGF- $\beta$ 1 from 0.1 to 10 ng/ml. Cell viability decreased to 95.25 % and 94.18 % after 48 h of treatment with 100 ng/ml and 1  $\mu$ g/ml (Figure 4.2B). The optimum concentration of TGF- $\beta$ 1-mouse recombinant protein (1 ng/ml) with 79.56 % cell viability was selected for subsequent TGF- $\beta$ 1 stimulation experiments.

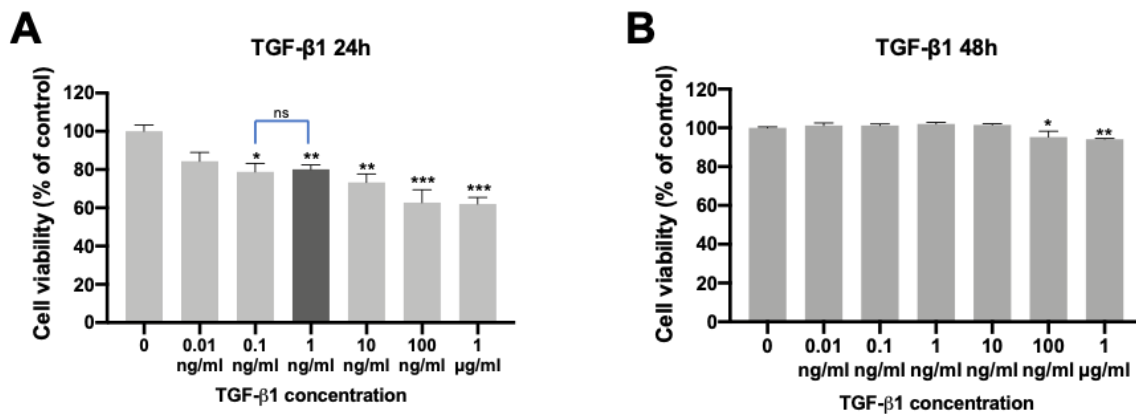


**Figure 4. 2.** Effect of various concentrations of TGF- $\beta$ 1 on MES13 cell viability in 96-well plates. MES13 cells were treated with TGF- $\beta$ 1 at the indicated concentrations for (A) 24 h and (B) 48 h. All the values are expressed as means  $\pm$  SEM for three independent experiments. Statistically significant at \*  $p < 0.05$ , \*\*  $p < 0.005$  and \*\*\*  $p < 0.001$  vs. control analysis of variance (ANOVA). **Abbreviation:** TGF- $\beta$ 1, transforming growth factor-beta 1.

To examine the cytotoxic effect of the TGF- $\beta$  type I receptor kinase inhibitor IV, A83-01, on MES13 cells, cell viability assay with A83-01 concentrations ranging from 0–100  $\mu\text{M}$  for 24 and 48 h was performed. As shown in Figure 4.3, A83-01 dose dependently decreased the cell viability from 1–100  $\mu\text{M}$  concentration ( $p < 0.05$ ) after 24 and 48 h of treatment. All further experiments were carried out with A83-01 at 1  $\mu\text{M}$  concentration.

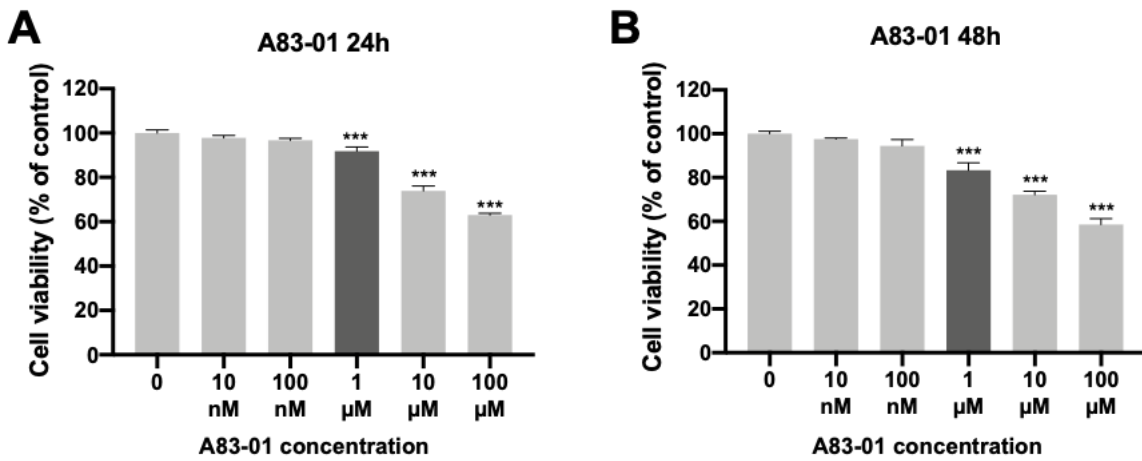


**Figure 4. 3.** Effect of various concentrations of A83-01 on MES13 cell viability in 96-well plates. MES13 cells were treated with A83-01 at the indicated concentrations for (A) 24 h and (B) 48 h. All the values are expressed as means  $\pm$  SEM for three independent experiments. Statistically significant at \*\*\*  $p < 0.001$  analysis of variance (ANOVA).

In this study, DEX, an anti-inflammatory glucocorticosteroid drug, was used as a model drug to assess the efficacy of this *in vitro* disease model. In order to determine whether DEX contributed directly to MES13 cell cytotoxicity, cell viability assay with varying concentrations of DEX were performed. As shown in Figure 4.4A, DEX significantly decreased the cell viability at the concentration from 10 nM–100  $\mu\text{M}$  ( $p < 0.05$ ) after 24 h

of treatment. After 48 h of treatment, the cell viability was gradually decreased as DEX concentration was increased (Figure 4.4B). To avoid the cytotoxicity caused by DEX (<70% viability), all further experiments were carried out with DEX at 10 nM concentration.

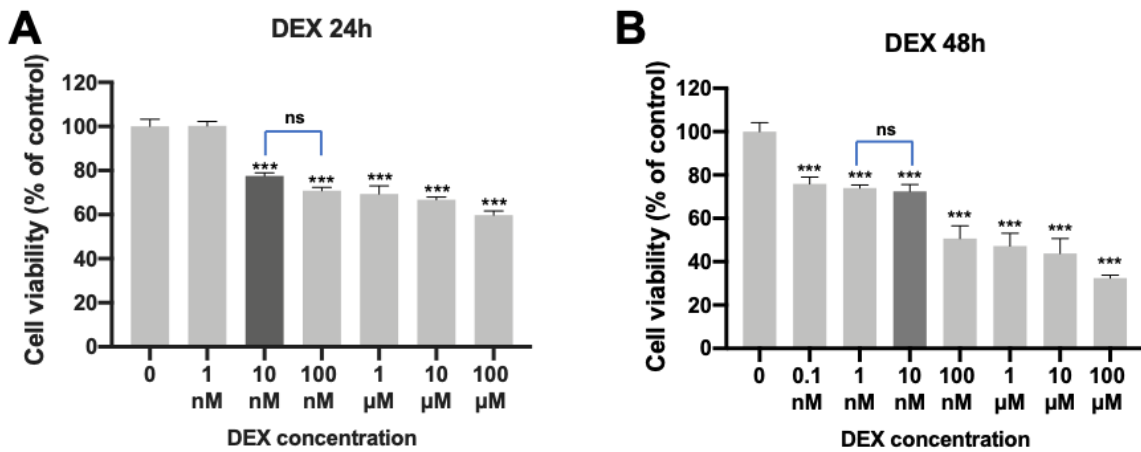
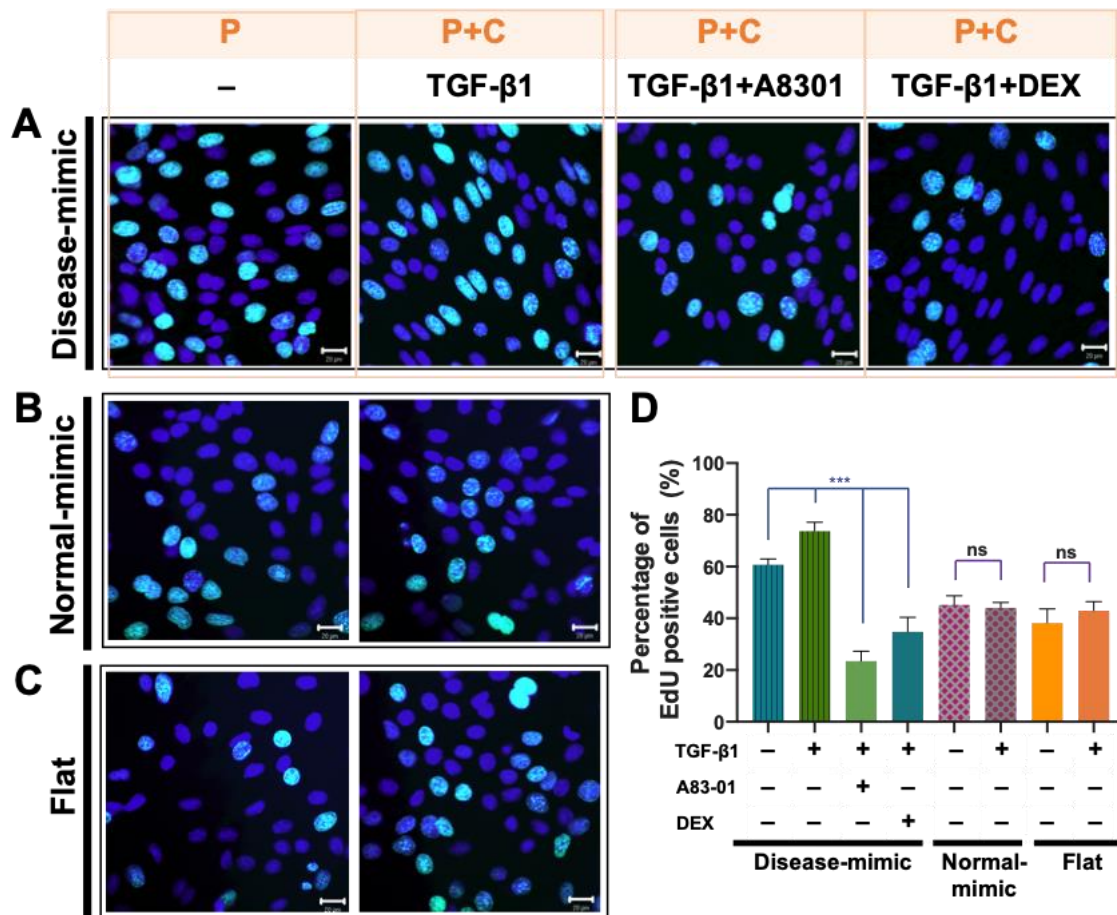


**Figure 4. 4.** Effect of various concentrations of DEX on MES13 cell viability in 96-well plates. MES13 cells were treated with DEX at the indicated concentrations for (A) 24 h and (B) 48 h. All the values are expressed as means  $\pm$  SEM for three independent experiments. Statistically significant at \*\*\*  $p < 0.001$  analysis of variance (ANOVA). **Abbreviation:** DEX, dexamethasone.

#### 4.3.2. The Effect of Disease-mimic Culture System on MES13 Cells Proliferation

Aberrant MC proliferation in mesangium is commonly observed in patients with glomerular disease and is initially stimulated by TGF- $\beta$ 1 [22]. To assess the effect of the disease-mimic culture system including chemical cue and physical cue on MES13 cells proliferation, disease-mimic nanopattern with 80 nm ridges and 200 nm grooves and 80nm depth as physical cue and MES cell treated by TGF- $\beta$ 1 as chemical cue were used. On the

other hand, normal-mimic nanopattern with pores approximately 50 nm in diameter, 80 nm spacing, and 80 nm in depth, and unpattern flat control were also used. Cell proliferation was performed by 5-ethynyl-2'-deoxyuridine (EdU) proliferation assays and counting the percentage of MES13 cells with incorporated EdU, which indicates newly-synthesized DNA (shown in green). Fluorescence images shown in Figure 4.5 revealed EdU incorporation into the nuclei of cells after 24 hours of seeding on disease-mimic nanopatterns (Figure 4.5A), normal-mimic nanopattern (Figure 4.5B) and flat control (Figure 4.5C). The results showed that a significant higher in cell proliferation (60.62 %) was observed in cells cultured on disease-mimic nanopatterns than those cultured on normal-mimic nanopattern (45.23 %) and flat control (38.21 %) after 24 hours of seeding without TGF- $\beta$ 1 treatment. After treatment with TGF- $\beta$ 1 (1 ng/ml), cell proliferation was significantly increased when cells were cultured on disease-mimic nanopatterns (68.50 %), whereas TGF- $\beta$  type I receptor inhibitor A83-01 and anti-inflammatory glucocorticosteroid drug DEX pretreatment markedly reduced the cell proliferation (23.46 % and 34.77 %, respectively) induced by not only TGF- $\beta$ 1, but also disease-mimic nanopatterns. However, there was no significant change in cell proliferation when cultured on normal-mimic nanopattern and flat control after treatment with TGF- $\beta$ 1. These results revealed that TGF- $\beta$ 1 and disease-mimic nanopatterns enhanced MES13 cell proliferation significantly, but this effect was abrogated by pretreatment with A83-01 and DEX. TGF- $\beta$ 1 did not induce significant change in proliferation when MES13 cells were grown on the normal-mimic nanopattern. These findings indicated that chemical cues strongly effected MES13 cell proliferation compared to physical cues alone on disease-mimic nanopattern. This effect did not influence cells on disease-mimic nanopattern and flat control.



**P: Physical cue**  
**C: Chemical cue**

**Figure 4. 5.** Effect of disease-mimic culture system on MES13 cell proliferation. Cells were cultured on (A) disease-mimic nanopattern, (B) normal-mimic nanopattern and (C) flat control surface and treated by 1 ng/ml of TGF- $\beta$ 1 with or without pretreatment with TGF- $\beta$  type I receptor inhibitor, A83-01, or glucocorticosteroid drug, DEX, for 24 h. Then proliferation was determined by the 5-ethynyl-2'-deoxyuridine (EdU) assay. Fluorescence images show EdU incorporation into the nuclei of cells. EdU-positive cells are green, and nuclei stained with 4',6-diamidino-2-phenylindole (DAPI) are blue. (D) Percentage of EdU-positive cells. Data are reported as means  $\pm$  SEM for three independent experiments. Statistically significant at \*\*\* $p < 0.001$  vs. disease-mimic nanopattern analysis of variance (ANOVA). Scale bar = 20  $\mu$ m. **Abbreviations:** TGF- $\beta$ 1, transforming growth factor-beta 1; DEX, dexamethasone; P, physical cue; C, chemical cue.

### **4.3.3. The Effect of Disease-mimic Culture System on MES13 Cells ECM Component Change**

MCs act to synthesize MM and provide support to glomerular capillaries [21, 23]. TGF- $\beta$ 1 is involved in mediating the biosynthesis activity of MM production [17]. To assess the effect of physical and chemical cues on matrix component expression in MES13 cells when cultured on disease-mimic nanopattern, immunofluorescence staining was performed to detect abnormal ECM component, COL1, and normal ECM component, COL4 (as shown in green color), after cells were grown on TiO<sub>2</sub> nanopatterns for 48 h. Confocal microscopy images of expression of COL1 (Figure 4.6A–C) showed that in the absence of TGF- $\beta$ 1, cells cultured on the disease-mimic nanopatterns had slightly increased expression of COL1, whereas there was no obvious expression in those cells cultured on normal-mimic nanopattern and flat control. After treatment with 1 ng/mL of TGF- $\beta$ 1, significantly increased COL1 expression was detected in cells cultured on disease-mimic nanopattern. In contrast, there were no significant differences noted between the presence or absence of TGF- $\beta$ 1 in those cells cultured on normal-mimic nanopatterns and flat control. However, significantly decreased COL1 was detected in cells cultured on disease-mimic nanopattern after pre-treating with A83-01 DEX, even lower than disease-mimic nanopattern induced COL1 expression. The quantitative MFI for COL1 expression is shown in Figure 4.6D.

On the other hand, cells cultured on the disease-mimic nanopatterns had lower COL4 expression when compared to those on normal-mimic nanopatterns and flat control in the absence of TGF- $\beta$ 1. After treatment with TGF- $\beta$ 1, COL4 expression was significantly reduced when cells were cultured on the disease-mimic nanopatterns and flat control. Meanwhile, there were no significant differences observed between the presence or

absence of TGF- $\beta$ 1 in those cells cultured on normal-mimic nanopatterns (Figure 4.7A–C). The quantitative MFI for COL4 expression is shown in Figure 4.7D.

These results revealed that TGF- $\beta$ 1 and disease-mimic nanopatterns significantly enhanced COL1 production in MES13 cell, but this effect was markedly abrogated by pretreatment with A83-01 or DEX. TGF- $\beta$ 1 did not induced significant change in COL1 production when MES13 cells were grown on the normal-mimic nanopattern. In addition, COL4 production in MES13 cells grown on normal-mimic nanopattern were not influenced by treatment of TGF- $\beta$ 1.

These observations indicated the presence of chemical cues resulting in increased abnormal ECM and decreased normal ECM compared to physical cues alone. However, this effect did not influence cells on normal-mimic nanopattern.

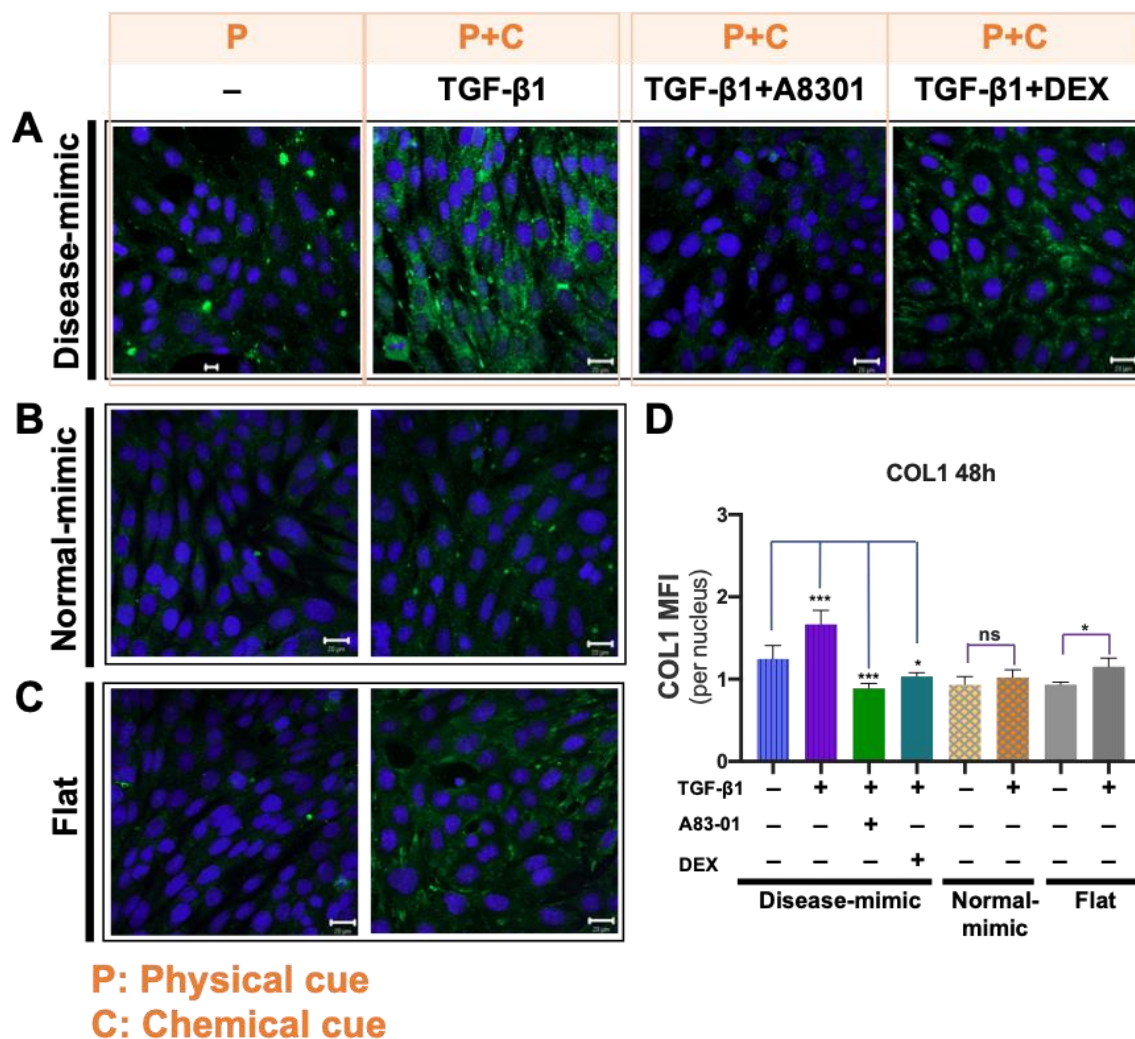


**Figure 4. 6.** Effects of TGF- $\beta$ 1 and disease-mimic nanopattern on expression of type I collagen (COL1) in MES13 cells. Cells were cultured on (A) disease-mimic nanopattern, (B) normal-mimic nanopattern and (C) flat control surface and treated by 1 ng/ml of TGF- $\beta$ 1 with or without pretreatment with A83-01 or DEX for 48 hours. (D) Quantification of COL1 fluorescent images was shown in mean fluorescence intensity per nucleus. All the values are expressed as means  $\pm$  SEM for three independent experiments. Statistically significant at \*  $p < 0.05$ , \*\*  $p < 0.005$  and \*\*\*  $p < 0.001$  vs. control analysis of variance (ANOVA). **Abbreviations:** TGF- $\beta$ 1, transforming growth factor-beta 1; DEX, dexamethasone; COL1, type I collagen; P, physical cue; C, chemical cue.

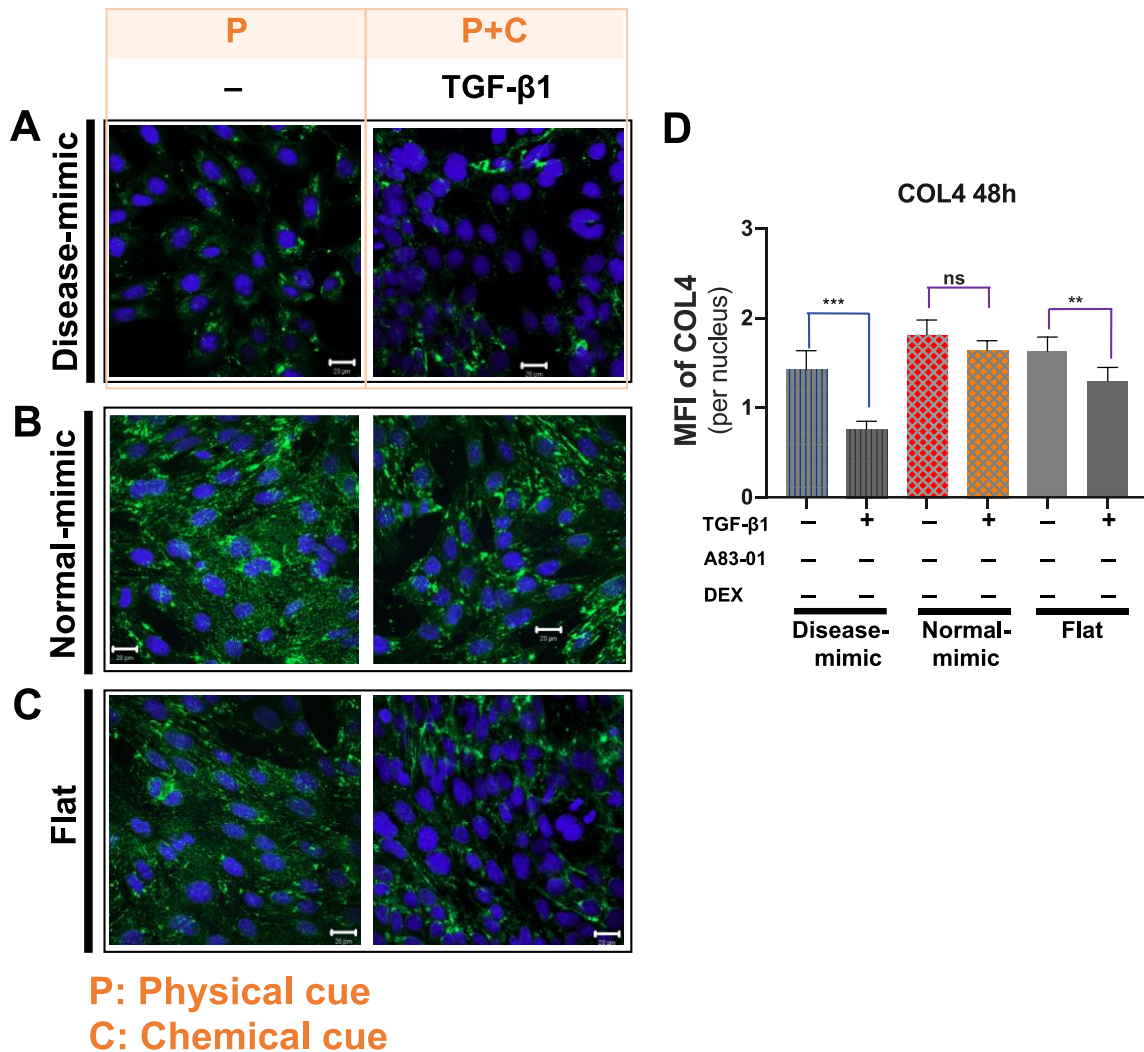


**Figure 4. 7.** The expression of type IV collagen (COL4) in MES13 cells cultured on (A) disease-mimic nanopatterns, (B) normal-mimic and (C) flat control surface after treatment with 1 ng/mL of TGF- $\beta$ 1 with or without pretreatment with A83-01, or DEX for 48 hours. (D) Quantification of COL4 fluorescent images was shown in mean fluorescence intensity per nucleus. All the values are expressed as means  $\pm$  SEM for three independent experiments. Statistically significant at \*\*  $p < 0.005$  and \*\*\*  $p < 0.001$  vs. control analysis of variance (ANOVA). **Abbreviations:** TGF- $\beta$ 1, transforming growth factor-beta 1; COL4, type IV collagen; P, physical cue; C, chemical cue.

#### **4.3.4 The Effect of Disease-mimic Culture System on MES13 Cells Intracellular ROS Production**

ROS play an important role in mediating TGF- $\beta$ 1 induced ECM induction and pro-fibrotic activity during kidney injury and in the progression of renal diseases [24]. To evaluate whether ROS can be the appropriate biomarker in this disease-mimic culture system, intracellular ROS levels were performed by the membrane-permeant fluorogenic probe, CellROX®.

It is important to study the time-course changes in ROS production due to treatments to understand the temporal changes leading to oxidative stress production. For the time-course studies, MES13 cells were incubated with 1 ng/ml TGF- $\beta$ 1, 1  $\mu$ M A83-01, or 10 nM DEX for 5 different time durations (1, 3, 6, 12 and 24 h) onto the 96-well plates. Intracellular ROS levels were performed by the membrane-permeant fluorogenic probe, CellROX®. As shown in Figure 4.8, intracellular ROS levels were significantly raised in cells treated with 1 ng/mL TGF- $\beta$ 1 for 12 h. Cells treated with neither A83-01 or DEX showed no significant change. Therefore, 12 h was selected as the upper-limit time point in the time-course results.

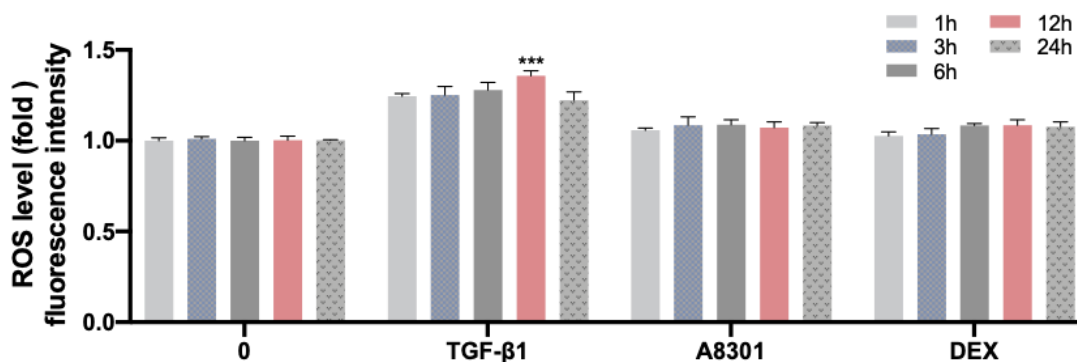


**Figure 4. 8.** ROS proliferation in MES13 cells treated with TGF-β1 (1ng/ml), A83-01 (1 μM), DEX (10nM) or untreated (0) at indicated time points in 96-well plates. All the values are expressed as means ± SEM for three independent experiments. Statistically significant at \*\*\*  $p < 0.001$  vs. control analysis of variance (ANOVA). **Abbreviations:** TGF-β1, transforming growth factor-beta 1; DEX, dexamethasone; ROS, reactive oxygen species.

Moreover, the effect of TGF-β1 on intracellular ROS production in MES13 cells cultured on disease-mimic nanopattern were further investigated using the CellROX® fluorogenic probe and the confocal microscope images was measured as the mean fluorescence intensity. As shown in Figure 4.9A-C, slightly increased ROS production was detected in cells cultured on disease-mimic nanopattern without TGF-β1 treatment, whereas no obvious ROS induction was detected in cells cultured on normal-mimic nanopattern and flat control. After treatment with TGF-β1, ROS production was dramatically enhanced when cells were cultured on the disease-mimic nanopatterns. In contrast, ROS production was gently raised in those cells cultured on normal-mimic nanopatterns and flat control. Both A83-01 and DEX markedly reduced the ROS production induced by TGF-β1, even by disease-mimic nanopatterns. The quantitative MFI for ROS production was shown in Figure 4.9D.

These findings indicated ROS production reflected the cell suffered from a disease situation that could be the appropriate biomarker in this disease-mimic culture system.

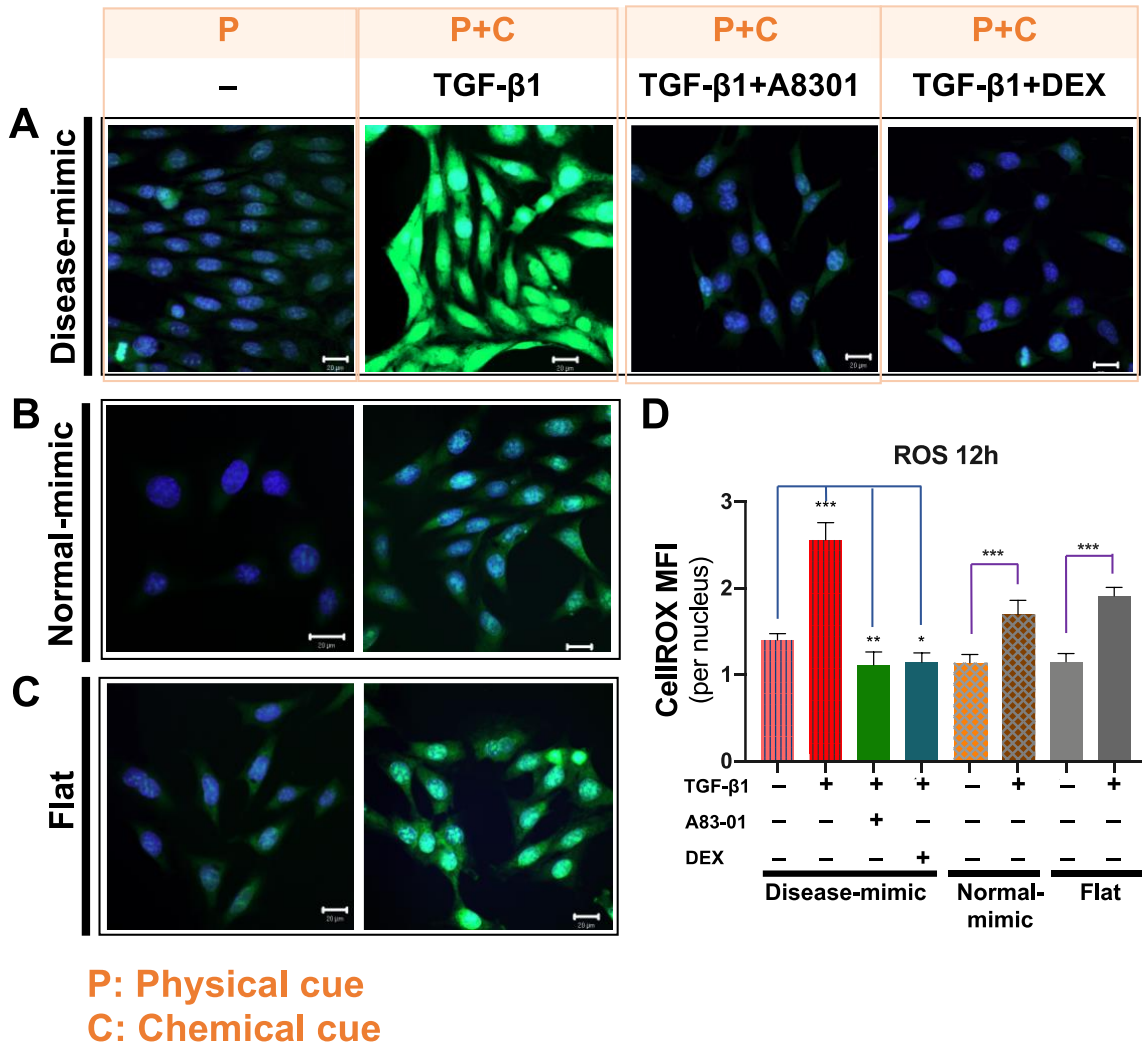


**Figure 4. 9.** Effects of TGF-β1 and disease-mimic nanopattern on ROS generation in MES13 cells. Cells were cultured on (A) disease-mimic nanopattern, (B) normal-mimic nanopattern and (C) flat control surface and treated by 1 ng/ml of TGF-β1 with or without pretreatment with A83-01 or DEX for 24 h. (D) Quantification of CellROX fluorescent images was shown in mean fluorescence intensity per nucleus. Values represent means ± SEM for three independent experiments. Statistically significant at \*  $p < 0.05$ , \*\*  $p < 0.005$  and \*\*\*  $p < 0.001$  vs. control analysis of variance (ANOVA). **Abbreviations:** TGF-β1, transforming growth factor-beta 1; DEX, dexamethasone; ROS, reactive oxygen species; P, physical cue; C, chemical cue.

#### 4.4. Discussion

In this chapter, the effects of chemical cue (TGF- $\beta$ 1) and physical cue (disease-mimic nanopattern) on MES13 cell proliferation and ECM components change were evaluated. The appropriate biomarker ROS production, in this disease-mimic culture system was also evaluated. The present results also noted that both A83-01 and DEX markedly abrogated the MES13 cells proliferation, COL1 synthesis and ROS production which was induced by TGF- $\beta$ 1 and normal-mimic nanopattern.

This *in vitro* disease-mimic culture system was established to mimic the *in vivo* renal disease condition cellular responses. The TiO<sub>2</sub>-based disease-mimic nanopattern with 80 nm depth, 80 nm ridges and 200nm grooves I previously established, was used as the physical cue for establishing the drug screening platform. This disease-mimic nanopattern had been shown to induce MES13 cells proliferation and alter MM components in my previous study [21]. Additionally, the present study designed TGF- $\beta$ 1 as a chemical cue to mimic an *in vivo* disease biological response as closely as possible. Treatment of TGF- $\beta$ 1 showed to aggravate the cellular responses mentioned above in MES13 cells cultured on disease-mimic nanopattern. However, there were no significant changes noticed in those cells cultured on normal-mimic nanopattern.

Currently, most novel culture systems with nanostructure focus on optimizing mechanical and structural properties of scaffolding matrices to better mimic the *in vivo* condition, with minimal integration of physical and chemical cues into the *in vitro* culture systems [4,25,26]. Thus, the appropriate selection of physical and chemical cues for the disease model is essential for mimicking the native environment.

The accumulation of ECM is a common phenomenon in the progression of glomerular disease [27]. Previous investigations have shown that TGF- $\beta$ 1 is a key mediator closely associated with progressive renal fibrosis that constitutes the final common pathway in numerous clinical and experimental glomerular injury response in progressive kidney diseases [27,28]. Increasing evidence indicates TGF- $\beta$ 1 promotes MC proliferation, upregulates MC expression of COL1, which could cause glomerular disease such as glomerulosclerosis [28,29]. My previous data demonstrated that MES13 cells expressed high proliferation and COL1 and fibronectin production when cultured on disease-mimic nanopattern [21]. The present study showed that 1 ng/ml of TGF- $\beta$ 1 significantly intensified the MES13 cells proliferation, COL1 production and ROS production when cultured on disease-mimic nanopattern. These results indicated that both TGF- $\beta$ 1 and disease-mimic nanopattern led MES13 cells display disease-like behavior, which has been demonstrate in several clinical and experimental studies on glomerular disease. These results suggest that the disease-mimic nanopattern and treatment of TGF- $\beta$ 1 should be appropriate for establishing a disease-mimic culture system.

Oxidative stress refers to the elevated intracellular ROS such as hydrogen peroxide ( $\text{H}_2\text{O}_2$ ), superoxide anion ( $\text{O}_2^-$ ), and hydroxyl radical ( $\text{OH}^\cdot$ ) that can cause damage to lipids, proteins and DNA [24,30]. In the kidney, ROS can be generated in MCs [30]. During the initial period of inflammation, the glomerular mesangium reacts by generating superoxide and hydrogen peroxide, mainly by NADPH oxidase [31,32]. In addition, during the disease states, elevated Angiotensin II could further induce generation of ROS in MCs [30,33]. Furthermore, TGF- $\beta$ 1 increases ROS production and suppresses antioxidant enzymes, leading to the development of fibrosis [24,33]. The present study showed TGF- $\beta$ 1 increases ROS production in MES13 cells on a disease-mimic model, even higher than

those induced by disease-mimic nanopattern, suggesting that ROS production reflect the MES13 cells were suffering from a disease-like situation.

A83-01 is a TGF- $\beta$ R1 ALK5 kinase inhibitor which can block TGF- $\beta$ -induced ECM overexpression via the downregulation of Smad2 phosphorylation levels [34]. Glucocorticoids are widely used as antiinflammatory and antifibrotic agents such as DEX are known to block the TGF $\beta$ 1-induced expression of ECM proteins both *in vitro* and *in vivo* model [35]. The present study showed that pretreatment with A83-01 and DEX respectively reduced cell proliferation, COL synthesis and ROS production in MES13 cells which was induced by TGF- $\beta$ 1 and disease-mimic nanopatterns. These results suggested that both A83-01 and DEX could attenuate the diseased condition induced by TGF- $\beta$ 1 and disease-mimic nanopatterns.

An important step of drug discovery process is screening the compound libraries, which basically contain hundreds of thousands of compounds, required by the high-throughput screening (HTS) [36,37]. HTS allows automatic and rapid testing of the biological or biochemical activity of large scale compound libraries for a specific biological target [38]. The present study not only provides a novel disease-mimic model for establishing a HTS platform in the future, but also offers a new insight into the therapeutics targeting TGF- $\beta$ -induced and ROS-dependent cellular signaling, which represents a novel approach in the specific pharmacological control of the inflammatory process or fibrotic disorders within glomerular mesangium.

## 4.5. Conclusion

This chapter evaluates the effect of a disease-mimic culture system with chemical cue (TGF- $\beta$ 1) and physical cue (disease-mimic nanopattern) on MES13 cells for establishing the drug screening platform.

The chemical cue showed to aggravate the diseased cellular responses such as cell proliferation, increased abnormal MM component, COL1, decreased normal ECM, COL4, and raised ROS proliferation in MES13 cells compared to the physical cue. In contrast, normal-mimic nanopattern seems to extenuate MES13 cells these effects. The model drugs, both A83-01 and DEX markedly reduced the COL4 and ROS production induced by TGF- $\beta$ 1, even by disease-mimic nanopatterns. This disease-mimic culture system with chemical cue (TGF- $\beta$ 1) and physical cue (disease-mimic nanopattern) showed to induced disease-like condition in cells. These results indicated that this disease-mimic culture could be used as a drug screening platform.

## References

1. Mohs, R.C.; Greig, N.H. Drug discovery and development: Role of basic biological research. *Alzheimers Dement (N Y)* **2017**, *3*, 651-657.
2. Kalaria, D.R.; Parker, K.; Reynolds, G.K.; Laru, J. An industrial approach towards solid dosage development for first-in-human studies: application of predictive science and lean principles. *Drug Discov Today* **2020**.
3. Ugolini, G.S.; Cruz-Moreira, D.; Visone, R.; Redaelli, A.; Rasponi, M. Microfabricated Physiological Models for In Vitro Drug Screening Applications. *Micromachines (Basel)* **2016**, *7*.

4. Caddeo, S.; Boffito, M.; Sartori, S. Tissue Engineering Approaches in the Design of Healthy and Pathological In Vitro Tissue Models. *Front Bioeng Biotechnol* **2017**, *5*, 40.
5. Booij, T.H.; Price, L.S.; Danen, E.H.J. 3D Cell-Based Assays for Drug Screens: Challenges in Imaging, Image Analysis, and High-Content Analysis. *SLAS Discov* **2019**, *24*, 615-627.
6. Duval, K.; Grover, H.; Han, L.H.; Mou, Y.; Pegoraro, A.F.; Fredberg, J.; Chen, Z. Modeling Physiological Events in 2D vs. 3D Cell Culture. *Physiology (Bethesda)* **2017**, *32*, 266-277.
7. Cheng, K.; Lai, Y.; Kisaalita, W.S. Three-dimensional polymer scaffolds for high throughput cell-based assay systems. *Biomaterials* **2008**, *29*, 2802-2812.
8. Francis, G.L. Albumin and mammalian cell culture: implications for biotechnology applications. *Cytotechnology* **2010**, *62*, 1-16.
9. Scharin-Mehlmann, M.; Haring, A.; Rommel, M.; Dirnecker, T.; Friedrich, O.; Frey, L.; Gilbert, D.F. Nano- and Micro-Patterned S-, H-, and X-PDMS for Cell-Based Applications: Comparison of Wettability, Roughness, and Cell-Derived Parameters. *Front Bioeng Biotechnol* **2018**, *6*, 51.
10. Muncie, J.M.; Weaver, V.M. The Physical and Biochemical Properties of the Extracellular Matrix Regulate Cell Fate. *Curr Top Dev Biol* **2018**, *130*, 1-37.
11. Nakashima, M.; Umemura, K.; Takiguchi, Y. [New animal models for drug discovery research: focus on cardiovascular diseases]. *Nihon Yakurigaku Zasshi* **1993**, *102*, 191-199.
12. Sams-Dodd, F. Strategies to optimize the validity of disease models in the drug discovery process. *Drug Discov Today* **2006**, *11*, 355-363.
13. Steuer, A.E.; Brockbals, L.; Kraemer, T. Metabolomic Strategies in Biomarker Research-New Approach for Indirect Identification of Drug Consumption and Sample Manipulation in Clinical and Forensic Toxicology? *Front Chem* **2019**, *7*, 319.

14. Schomaker, S.; Ramaiah, S.; Khan, N.; Burkhardt, J. Safety biomarker applications in drug development. *J Toxicol Sci* **2019**, *44*, 225-235.
15. Kraus, V.B. Biomarkers as drug development tools: discovery, validation, qualification and use. *Nat Rev Rheumatol* **2018**, *14*, 354-362.
16. Strimbu, K.; Tavel, J.A. What are biomarkers? *Curr Opin HIV AIDS* **2010**, *5*, 463-466.
17. Rupprecht, H.D.; Schocklmann, H.O.; Sterzel, R.B. Cell-matrix interactions in the glomerular mesangium. *Kidney Int* **1996**, *49*, 1575-1582.
18. Lennon, R.; Randles, M.J.; Humphries, M.J. The importance of podocyte adhesion for a healthy glomerulus. *Front Endocrinol (Lausanne)* **2014**, *5*, 160.
19. Arif, E.; Nihalani, D. Glomerular Filtration Barrier Assembly: An insight. *Postdoc J* **2013**, *1*, 33-45.
20. Scindia, Y.M.; Deshmukh, U.S.; Bagavant, H. Mesangial pathology in glomerular disease: targets for therapeutic intervention. *Adv Drug Deliv Rev* **2010**, *62*, 1337-1343.
21. Chang, C.J.; Minei, R.; Sato, T.; Taniguchi, A. The Influence of a Nanopatterned Scaffold that Mimics Abnormal Renal Mesangial Matrix on Mesangial Cell Behavior. *Int J Mol Sci* **2019**, *20*.
22. Loeffler, I.; Hopfer, U.; Koczan, D.; Wolf, G. Type VIII collagen modulates TGF-beta1-induced proliferation of mesangial cells. *J Am Soc Nephrol* **2011**, *22*, 649-663.
23. Kurihara, H.; Sakai, T. Cell biology of mesangial cells: the third cell that maintains the glomerular capillary. *Anat Sci Int* **2017**, *92*, 173-186.
24. Liu, R.M.; Desai, L.P. Reciprocal regulation of TGF-beta and reactive oxygen species: A perverse cycle for fibrosis. *Redox Biol* **2015**, *6*, 565-577.
25. Crosby, C.O.; Zoldan, J. Mimicking the physical cues of the ECM in angiogenic biomaterials. *Regen Biomater* **2019**, *6*, 61-73.

26. Rijal, G.; Li, W. Native-mimicking in vitro microenvironment: an elusive and seductive future for tumor modeling and tissue engineering. *J Biol Eng* **2018**, *12*, 20.
27. Schnaper, H.W.; Hayashida, T.; Hubchak, S.C.; Poncelet, A.C. TGF-beta signal transduction and mesangial cell fibrogenesis. *Am J Physiol Renal Physiol* **2003**, *284*, F243-252.
28. Hayashida, T.; Poncelet, A.C.; Hubchak, S.C.; Schnaper, H.W. TGF-beta1 activates MAP kinase in human mesangial cells: a possible role in collagen expression. *Kidney Int* **1999**, *56*, 1710-1720.
29. Francki, A.; Bradshaw, A.D.; Bassuk, J.A.; Howe, C.C.; Couser, W.G.; Sage, E.H. SPARC regulates the expression of collagen type I and transforming growth factor-beta1 in mesangial cells. *J Biol Chem* **1999**, *274*, 32145-32152.
30. Baud, L.; Ardaillou, R. Reactive oxygen species: production and role in the kidney. *Am J Physiol* **1986**, *251*, F765-776.
31. Ha, H.; Lee, H.B. Reactive oxygen species as glucose signaling molecules in mesangial cells cultured under high glucose. *Kidney Int Suppl* **2000**, *77*, S19-25.
32. Jiang, Z.; Seo, J.Y.; Ha, H.; Lee, E.A.; Kim, Y.S.; Han, D.C.; Uh, S.T.; Park, C.S.; Lee, H.B. Reactive oxygen species mediate TGF-beta1-induced plasminogen activator inhibitor-1 upregulation in mesangial cells. *Biochem Biophys Res Commun* **2003**, *309*, 961-966.
33. Ratliff, B.B.; Abdulmahdi, W.; Pawar, R.; Wolin, M.S. Oxidant Mechanisms in Renal Injury and Disease. *Antioxid Redox Signal* **2016**, *25*, 119-146.
34. Tojo, M.; Hamashima, Y.; Hanyu, A.; Kajimoto, T.; Saitoh, M.; Miyazono, K.; Node, M.; Imamura, T. The ALK-5 inhibitor A-83-01 inhibits Smad signaling and epithelial-to-mesenchymal transition by transforming growth factor-beta. *Cancer Sci* **2005**, *96*, 791-800.

35. Kuroda, M.; Sasamura, H.; Shimizu-Hirota, R.; Mifune, M.; Nakaya, H.; Kobayashi, E.; Hayashi, M.; Saruta, T. Glucocorticoid regulation of proteoglycan synthesis in mesangial cells. *Kidney Int* **2002**, *62*, 780-789.
36. Nierode, G.; Kwon, P.S.; Dordick, J.S.; Kwon, S.J. Cell-Based Assay Design for High-Content Screening of Drug Candidates. *J Microbiol Biotechnol* **2016**, *26*, 213-225.
37. Komnatnyy, V.V.; Nielsen, T.E.; Qvortrup, K. Bead-based screening in chemical biology and drug discovery. *Chem Commun (Camb)* **2018**, *54*, 6759-6771.
38. Hughes, J.P.; Rees, S.; Kalindjian, S.B.; Philpott, K.L. Principles of early drug discovery. *Br J Pharmacol* **2011**, *162*, 1239-1249.

---

## Chapter V

### Conclusions and Future Perspectives

---

#### 5.1. Conclusions

Experimental disease models with the purpose to elucidate the pathogenesis, mechanism, pharmaceutical efficacy and developing therapeutics of human disease can be achieved by *in vivo* and *in vitro* models [1-3]. However, both *in vivo* and *in vitro* models have limitations that result in discrepancy between the *in vitro* and *in vivo* studies. The one biggest limitation of *in vitro* models is that petri-dish flat surfaces with a monolayer on which cells are cultivated poorly reflect the *in vivo* nano-environment, which is a complex environment of the ECM that provides physical and chemical cues to regulate the cell behavior [4, 5]. In order to address these issues, advanced nanofabrication techniques offer novel tools to better mimic the *in vivo* nano-environment [6, 7]. This dissertation consists of five chapters.

Chapter I introduced the advantages and disadvantages of *in vivo* and *in vitro* experimental models and its importance in the human diseases related studies. Bridging the discrepancy between *in vivo* and *in vitro* models due to the difference in the natural nanoenvironment and using nanopattern to mimic the natural nanoenvironment could dissolve this issue. Herein, I firstly hypothesized that mimicking the natural

---

nanoenvironment by nanopattern could bridge the discrepancy between *in vivo* and *in vitro* models.

Chapter II established an *in vivo* disease experimental model of IBD-associated renal disease studies. The results clarified that a DSS-induced colitis mouse model induced changes in glomerular structure and renal inflammation that was consistent with the clinical reports of IBD patients with renal disease, which indicated that this DSS-induced colitis mouse model could lead to novel uses of the animal model for further investigations into IBD-associated renal disease.

Chapter III developed an *in vitro* renal disease model that mimicking the disease-like cell behavior which is consistent with the DSS-induced colitis mouse model. The results showed a disease-mimic nanopattern guided MES13 cells in adopting disease-like behaviors including increased cell proliferation, abnormal MM components (COL1 and fibronectin), higher expression of  $\alpha$ -SMA, TGF- $\beta$ 1 and integrin  $\alpha$ 5 $\beta$ 1, which indicated that this disease-mimic nanopattern could be important to further establish a disease-mimic culture system for elucidating the molecular mechanisms underlying glomerular disease

Chapter IV evaluated the physical and chemical cues on disease-mimic culture system. The results showed that disease-mimic culture system with chemical cue (TGF- $\beta$ 1) and physical cue (disease-mimic nanopattern) aggravated the diseased cellular responses such as cell proliferation, increased abnormal MM component, COL1, decreased normal ECM, COL4, and raised ROS proliferation in MES13 cells, which indicated that this disease-mimic culture system could induced disease-like condition in MES13 cells and could be used as a drug screening platform.

In conclusions, an *in vivo* IBD animal model, DSS-colitis mice model, showed consistent results with clinical reports of IBD patients who have renal disease. In addition, an *in vitro* disease-mimic culture system with chemical cue (TGF- $\beta$ 1) and physical cue (disease-mimic nanopattern) showed the consistent results with DSS-colitis mice model, which indicated that this disease-mimic culture system could provide a platform to study cell behaviors that mimic *in vivo* diseased conditions. These results verified my hypothesis that mimicking the natural nanoenvironment by nanopattern could bridge the discrepancy between *in vivo* and *in vitro* models. This work could be beneficial for the future pre-clinal *in vivo* studies.

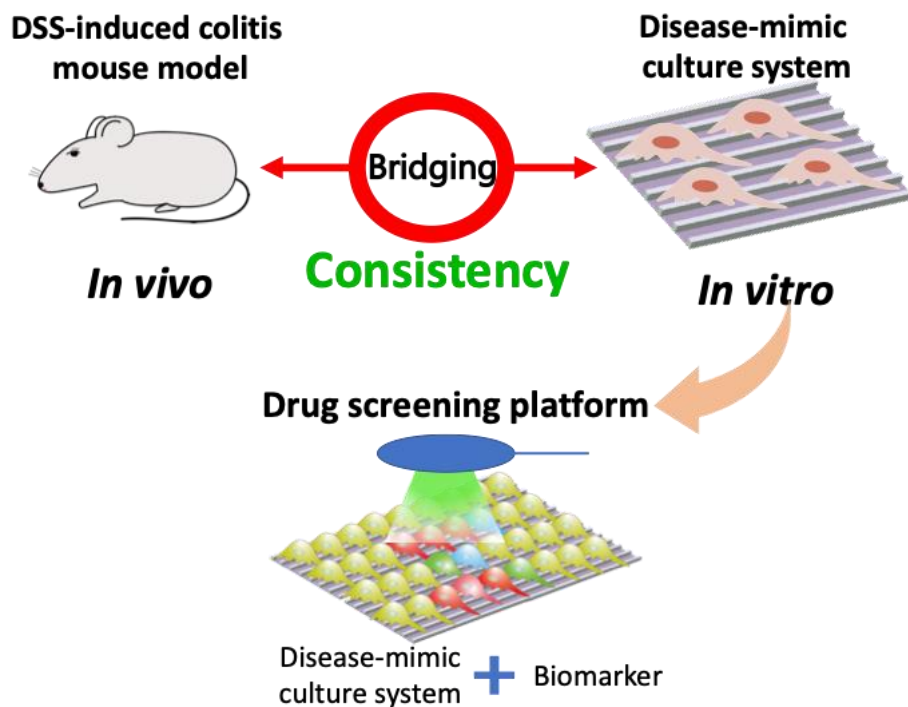


**Figure 5. 1.** Illustration of summary that the consistent results from *in vivo* and *in vitro* models developed a disease-mimic culture system that could be used for drug screening platform.

## 5.2. Future Perspectives

For improvements of related studies using this disease-mimic culture system, I arranged some future prospects based on this work. The glomerular filtration barrier consists of MCs, endothelial cells, and podocytes along with the glomerular basement membrane. They act in different roles to maintain the glomerular filtration function. Herein, the further research objective will be divided 1) to modify the parameters of the nanopattern to better mimic the specific ECM properties for each cell such as podocytes and endothelial cells; 2) to use the co-culture system to establish the disease model for elucidation of cell-cell interaction under glomerular disease; and 3) to adjust the parameters of the nanopattern according to organ-specific nanostructure and to establish the organ-specific *in vitro* fibrosis models. Figure 5.2 illustrates the future prospects based on the results obtained from this work.

In addition to the technical limitations and demands of nanopattern manufacturing, observations of nanopatterned samples sometimes suffered due to the sample color causing light blocking and resulting in technical difficulties. Finding substitutable biomaterials for better observing the unstained cell morphology under inverted light microscope could dissolve this limitation.

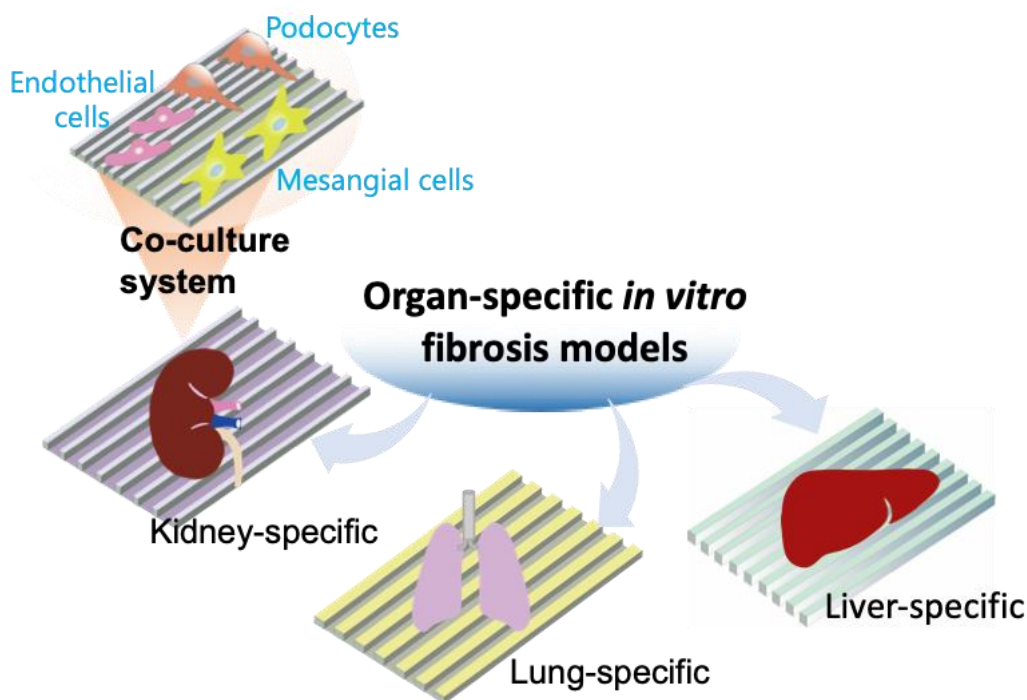


**Figure 5. 2.** Illustration of the future prospects to establish the organ-specific *in vitro* fibrosis model using nanopatterning.

## References

1. McGonigle, P.; Ruggeri, B. Animal models of human disease: challenges in enabling translation. *Biochem Pharmacol* **2014**, *87*, 162-171.
2. Breyer, M.D.; Look, A.T.; Cifra, A. From bench to patient: model systems in drug discovery. *Dis Model Mech* **2015**, *8*, 1171-1174.
3. Williams, S.M.; Haines, J.L.; Moore, J.H. The use of animal models in the study of complex disease: all else is never equal or why do so many human studies fail to replicate animal findings? *Bioessays* **2004**, *26*, 170-179.
4. Duval, K.; Grover, H.; Han, L.H.; Mou, Y.; Pegoraro, A.F.; Fredberg, J.; Chen, Z. Modeling Physiological Events in 2D vs. 3D Cell Culture. *Physiology (Bethesda)* **2017**, *32*, 266-277.

5. Chaicharoenaudomrung, N.; Kunhorm, P.; Noisa, P. Three-dimensional cell culture systems as an in vitro platform for cancer and stem cell modeling. *World J Stem Cells* **2019**, *11*, 1065-1083.
6. Betancourt, T.; Brannon-Peppas, L. Micro- and nanofabrication methods in nanotechnological medical and pharmaceutical devices. *Int J Nanomedicine* **2006**, *1*, 483-495.
7. Ermis, M.; Antmen, E.; Hasirci, V. Micro and Nanofabrication methods to control cell-substrate interactions and cell behavior: A review from the tissue engineering perspective. *Bioact Mater* **2018**, *3*, 355-369.

# List of Research Achievements

## Academic papers

1. ○ **Chia-Jung Chang**, Rin Minei, Takeshi Sato and Akiyoshi Taniguchi. “The Influence of a Nanopatterned Scaffold that Mimics Abnormal Renal Mesangial Matrix on Mesangial Cell Behavior”. *Int J Mol Sci.* **2019** 20(21).
2. ○ **Chia-Jung Chang**, Pi-Chao Wang, Tzou-Chi Huang and Akiyoshi Taniguchi. “Change in Renal Glomerular Collagens and Glomerular Filtration Barrier-Related Proteins in a Dextran Sulfate Sodium-Induced Colitis Mouse Model”. *Int J Mol Sci.* **2019** 20(6).
3. Hso-Chi Chaung, Chin-Dong Chang, Pi-Hang Chen, **Chia-Jung Chang**, Shyh-Hwa Liu and Chih-Cheng Chen. “Docosahexaenoic acid and phosphatidylserine improves the antioxidant activities in vitro and in vivo and cognitive functions of the developing brain”. *Food Chemistry* **2013**, 138: 342–347.

## Conference paper

**Chia-Jung Chang**, Chih-Cheng Chen, Chin-Dong Chang and Hso-Chi Chaung. “The Anti-oxident Effects of Docosahexaenoic Acid and Arachidonic Acid on Neuronal Cells and Astrogliaocytes”. International Conference on Bioscience, Biochemistry and Bioinformatics (ICBBB) 2011. IPCBEE 5:39-43 (2011).

## Presentations

Oral Presentations:

1. **Chia-Jung Chang** and Akiyoshi Taniguchi. “The Effects of a Nanopatterned Scaffold Mimicking Diseased Renal Mesangial Matrix on Mesangial Cell Behavior”. 14th

- Annual Meeting of the Nano Biomedical Society, **2019**. Tokyo, Japan.
2. **Chia-Jung Chang** and Akiyoshi Taniguchi. Development of a Novel Renal Disease Model by Nanopatterned Scaffold”. The 28<sup>th</sup> Intelligent Nanomaterial Symposium, **2018**. Tokyo, Japan.
  3. **Chia-Jung Chang** and Akiyoshi Taniguchi. “Development of a Novel Renal Disease Model by Nanopatterned Scaffold”. International Conference on Emerging Advanced Nanomaterials (ICEAN) **2018**. Newcastle NSW, Australia.
  4. **Chia-Jung Chang** and Akiyoshi Taniguchi. “Development of a Novel Renal Disease Model by Nanopatterned Scaffold”. 13<sup>th</sup> Annual Meeting of the Nano Biomedical Society, **2018**. Tokyo, Japan.
  5. Chia-Jung Chang, Tzou-Chi Huang and Pi-Chao Wang. “Influence of DSS-induced colitis on kidney injury and ECM change of mice”. Early Career Physiologists' Symposium (ECPS**2016**).
  6. **Chia-Jung Chang**, Chih-Cheng Chen, Chin-Dong Chang and Hso-Chi Chaung. “The Anti-oxident Effects of Docosahexaenoic Acid and Arachidonic Acid on Neuronal Cells and Astrogliaocytes”. International Conference on Bioscience, Biochemistry and Bioinformatics (ICBBB) **2011**. Sentosa, Singapore.

Poster Presentations:

1. **Chia-Jung Chang** and Akiyoshi Taniguchi. “Influence of Mesangial Cell Behavior on Disease-mimic Mesangial Matrix”. 41<sup>th</sup> Japanese Society for Biomaterials meeting, **2019**. Tsukuba, Japan.
  2. **Chia-Jung Chang** and Akiyoshi Taniguchi. “Novel Use of a Dextran Sulfate Sodium-induced Colitis Mouse Model in the Study of IBD-associated Renal Disease”. 30<sup>th</sup> Annual Conference of the European Society for Biomaterials ESB **2019**. Dresden, Germany.
  3. **Chia-Jung Chang** and Akiyoshi Taniguchi. “The Effects of Nanopatterned Scaffold Mimicking the Abnormal Renal Mesangial Matrix on Mesangial Cell Behavior”. 30<sup>th</sup> Annual Conference of the European Society for Biomaterials ESB **2019**. Dresden, Germany.
  4. **Chia-Jung Chang** and Akiyoshi Taniguchi. “Effects of Artificial Nanotopographical
-

- Surfaces on Renal Mesangial Cell Behavior”. MANA International Symposium **2019**. Tsukuba, Japan.
5. **Chia-Jung Chang** and Akiyoshi Taniguchi. “Establishment of Disease Model Using Nano-patterned Scaffold”. 40th Japanese Society for Biomaterials meeting, **2018**. Tsukuba, Japan.
  6. **Chia-Jung Chang**, Tzou-Chi Huang and Pi-Chao Wang. “Influence of DSS-induced colitis on kidney injury and ECM change of mice”. Proc Physiol Soc 37 (2016), p345-346. **2016**. Dublin, Ireland.
  7. **Chia-Jung Chang**, Tzou-Chi Huang and Pi-Chao Wang. “Influence of DSS-induced colitis on kidney injury and ECM change of mice”. The 48th Annual Meeting of The Japanese Society for Matrix Biology and Medicine, p137 (2016). **2016**. Nagasaki, Japan.
  8. **Chia-Jung Chang**, Tzou-Chi Huang and Pi-Chao Wang. “Effects of DSS-induced colitis on kidney injury and ECM accumulation of mice”. Tsukuba Students Research Exchange Workshop, p16 (2016). **2016**. Ibaraki, Japan.
  9. **Chia-Jung Chang**, Chih-Cheng Chen, Chin-Dong Chang and Hso-Chi Chaung. “Effects of Docosahexaenoic Acid and Phosphatidylserine on Neurexin II Gene Expression and Neuronal Apoptosis”. 2009 Joint Spring Conference of the Chinese Society of Veterinary Science and the Taiwan Association of Veterinary Science and Animal Husbandry (CSVS/TAVSAH), p55 (2009). Taiwan.

## Patent

Hso-Chi Chaung, Chih-Cheng Chen, **Chia-Jung Chang**. “Bioactive Liposomes and Method for Making the Same”. R.O.C. Patent I378937. Taiwan.